TWO–PROTON INTENSITY INTERFEROMETRY FOR IMPACT–PARAMETER SELECTED ^{36}AR + ^{45}SC COLLISIONS AT E/A=80, 120 AND 160 MEV

By

Damian Orest Handzy

A DISSERTATION

Submitted to
Michigan State University
in partial fulfillment of the requirements
for the degree of

DOCTOR OF PHILOSOPHY

Department of Physics and Astronomy

1995

ABSTRACT

TWO-PROTON INTENSITY INTERFEROMETRY FOR IMPACT–PARAMETER SELECTED ^{36}AR + ^{45}SC COLLISIONS AT E/A=80, 120 AND 160 MEV

By

Damian Orest Handzy

Impact–parameter selected two–proton intensity interferometry is used to study the space–time characteristics of emitting sources formed in medium–energy heavy–ion collisions.

Building on a previous study for the same system at a lower energy, a high–resolution 56–element Si–CsI(Tl) hodoscope was used to collect single– and two–proton yields, for collisions of ^{36}Ar + ^{45}Sc at E/A=120 MeV and 160 MeV. Coincident measurements of other charged particles emitted in the reaction were made with the MSU 4π Array, providing information about the impact–parameter of the collision.

The Boltzmann–Uehling–Uhlenbeck (BUU) equation is used to predict the emission of protons from the reaction zone created in heavy–ion collisions. The Koonin–Pratt formalism is then used to calculate theoretical correlation functions from the predicted single–particle phase space probability density. Dependencies of predicted longitudinal and transverse correlation functions on source velocity are examined for central and peripheral ^{36}Ar + ^{45}Sc collisions at E/A=80 MeV, and are compared to previously measured values. The usefulness of the correlation function to distinguish exotically shaped sources, predicted by microscopic transport models at this energy, is investigated.

Consistent with previous measurements, proton correlations are shown to have larger peaks for more energetic protons, regardless of impact–parameter. However, the measured correlations are shown to decrease as beam energy

increases from E/A=80 to 160 MeV, indicating that proton–emitting sources formed in more energetic collisions appear to have larger space–time extents. For central collisions at E/A=160 MeV, the correlation function shows no dependence on the momentum of the proton pair, suggesting that the source emits fast and slow protons on similar time scales.

The BUU theory is shown to over predict the magnitude of the measured correlations for the reactions at E/A=120 and 160 MeV, possibly because of the effects of proton emission from particle unstable resonance states not modeled by the theory.

Рені

ACKNOWLEDGMENTS

I became interested in the study of the nucleus as an undergraduate student working with Professors Fay Ajzenberg–Selove, David Balamuth and Keith Griffieon at the University of Pennsylvania. My undergraduate thesis project (on ^{6}He) developed into a collaboration between David Balamuth's group and the A1200 group at the NSCL, which will continue with an experiment next month. To the three of them I will be forever grateful for kindling in me a passion for experimental physics.

At the NSCL, I have had the fortune of working with many outstanding physicists. Most influential among them has been my advisor and friend, Claus–Konrad Gelbke. I have learned far more from him than the methods of world–class scientific research. I have been witness many times to his exceptional organizational, interpersonal, and professional skills, and to the diligence and integrity with which he approaches every situation. His influence on me, both personally and professionally, will be everlasting. Thank you, Konrad.

During my graduate studies, I have also had the privilege of working with and learning from other physicists who are "neck deep" in correlation functions. Wolfgang Bauer has worked closely with me on comparing predictions of his BUU model with my experimental results, and has taken an active and influential part in my education. Scott Pratt, whose door is always open, sat patiently through my numerous questions, even though I'm sure he had just answered them days before. Many thanks to you both.

I am also thankful to Gary Westfall, Skip Vander Molen, and the entire 4π Group for going through not one – but two – more hodopscope – 4π experiments. My guidance committee deserves special recognition. To Professors Pope and Mahanti I am thankful for their participation and input

during the first 3 years. To Professors Yuan and Duxbury, I am especially grateful for serving on my committee on such short notice.

I also wish to thank a number of physicists from the NSCL and other institutions. They are: David Bowman, Romualdo deSouza, Thomas Glasmacher, Roy Lacey, Roy Lemmon, Bill Llope, Graham Peaslee, Carsten Schwarz, M. Betty Tsang, and Gordon Wozniak. And of course, I (the *cook*), say to Nicola Colonna (the *chambermaid*), "gracia."

I have been very fortunate to become close friends with a few fellow graduate students who have made my years in Michigan especially enjoyable. From over–boiling wort with Phil, Brian and Mathias, to gripe sessions over Long Islands with Carlos and discussing everything from Wall Street to Windows programming with David over cappuccino, the friendships I have formed with them will last a lifetime. I have enjoyed our time together, and the privilege of their company.

I am indebted to my friends Phil Zecher, Carlos Montoya, David McGrew, Brian Young, Mathias Steiner, Sally Gaff, Jac Caggiano, Mike Fauerbach, Renan Fontus, Njema Frazier, Gene Gualtieri, Stefan Hannuschke, Wen–Chien Hsi, Min–Jui Huang, John Kruse, Michael Lisa, Catherine Mader, Joelle Murray, Raman Pfaff, Larry Phair, Chris (it's 4π!) Powel, Easwar Ramakrishnan, and Shigeru Yokoyama for sharing with me a small part of their lives. A professor once told me that in graduate school you meet the most interesting people at the worst time of their lives. He clearly did not know my friends, who have made the past four years some of my best. I thank each of you.

I owe thanks to many NSCL employees for their roles in making my time at the cyclotron lab enjoyable. They are: Kay Barber, Shari Conroy, Mike Ellis, Laura Hernandez, Tina Keehn, Rilla McHarris, Chris O'connor, Barb Pollack, Reg Ronningen, Arlieta Sawyer, Greg Scoczlas, Dennis Swan, Chris Townsend, and, of course, C–c–c–h–h–h–u–u–u–c–c–c–k–k–k V–v–v–a–c–e–k.

During our trips back East, Renata and I were always met with relatives' warm smiles, in amazement that we were able to make yet another family event. To all of you, for always providing us a place to rest our heads and quench our thirst, I am thankful.

From discussions about the height of the Saturn–V rocket (while crossing the George Washington bridge) to multiple trips to the Hayden Planetarium and the Museum of Natural History, my parents taught me at an early age that science is both interesting and fun. Through their own lives, they have taught me how to reach things not initially in my grasp, and how to enjoy the time in between. Я Вас люблю і Вам дякую.

As I conclude my graduate studies, my brother is still in the middle of his own program in mathematics. Although we have not lived together in over 4 years, we continue to become closer, as each of us follows his own path. I thank you, Nest, for reminding me to keep things in perspective as I struggled with the demands of academic life, and for constantly reminding me of my "war crimes." Now let me remind you of one thing: I love you, too.

Most of all, I thank Реня, my wife. This thesis is dedicated to her because of the tremendous support she has given me during my years of graduate school. For everything you put up with, from late nights at the lab to family event we *didn't* make, I thank you. Now it's time to move on to our next adventure together, and it's you turn to lead the way. Я Тобі дуже дякую і Тебе дуже люблю.

TABLE OF CONTENTS

LIST OF TABLES

LIST OF FIGURES

Chapter 1 – Introduction

1.1 Medium Energy Heavy–Ion Collisions

The study of heavy ion collisions at intermediate energies (E/A≈20–200 MeV) is an active field of fundamental research aimed at understanding the thermodynamic properties of strongly interacting quantum systems under extreme conditions of pressure and temperature. The nuclear system under study has between 20 and 200 constituents – too many to be understood in an accurate few body formalism, and not enough to be treated in a truly statistical manner. In addition, the system evolves over a very short time scale: on order 10^{-22} sec, or about 100 fm/c. As a consequence, many phenomena may require theoretical treatment by a quantum transport theory rather than allowing purely statistical descriptions. For these reasons the study of nucleus–nucleus collisions in this energy regime is interesting and very challenging, both experimentally and theoretically.

The dynamical and statistical effects of nuclear collisions are both heavily dependent upon the bombarding energy and the impact parameter. At low energies (typically a few MeV/nucleon), the reaction depends on mean–field effects and single body dissipation. Peripheral collisions can be described as "quasi–elastic", in which the target and projectile exit the reaction slightly perturbed by the collisions, possibly in excited states. Alternatively, peripheral collisions can also be classified as "deeply inelastic", in which case there is substantial exchange of energy, angular momentum and even nucleons between target and projectile. Central collisions result in a long–lived equilibrated system which decays by statistical particle evaporation.

At much higher, relativistic, energies ($E/A \geq 1$ GeV), nuclear reactions are described in terms of individual nucleon–nucleon collisions. The geometrical picture of the participant–spectator model is appropriate in which the hot (participant) region is defined by the geometric overlap of projectile and target.

The deposited energy causes the system to "explode," emitting constituent nucleons as well as more exotic massive particles. Statistically models are applicable to the participant zone, where thermal equilibrium is readily achieved.

Between these two extremes is the intermediate–energy regime for which both mean field effects and nucleon–nucleon collisions are important. Statistical and dynamical processes compete as the system evolves. After an early emission of fast nucleons, a semi–equilibrated system is predicted to remain which continues to evolve through statistical decay, possibly accompanied by expansion. Pre–equilibrium emission of particles is known to be important. At low energies, the system undergoes a sequential binary decay, while at higher energies, multifragment decays are known to occur on an increasingly shorter time scale. Experimental evidence exists for Au + Au collisions at E/A=200 MeV that the source expands as it emits fragments [Hsi 94, Jeon 94] and dynamical model calculations have predicted the formation of exotically shaped sources for central collisions in this energy domain [Baue 92a, Gros 92, Bord 85, Xu 93 and Hand 94]. A liquid–gas phase transition is expected to occur in nuclear matter of temperature 5–10 MeV and density 0.1 to 0.5 times normal nuclear density.

Experimental progress has been significant in recent years. Higher resolution, lower threshold detector arrays have allowed more detailed measurements of reaction products and unique detectors have permitted studies in which nearly all emitted particles are detected, allowing a detailed characterization of the collision process.

1.2 Intensity Interferometry

Interferometry has played an important role in physical and astronomical measurements. The famous Young double–slit experiment, which used an amplitude interferometer, was instrumental in establishing the wave theory of light, and was crucial in the development of a unified electromagnetic theory.

Out of this theory came the notion of the aether, the medium which "waved" when light traveled. It was not until 1881 that Michelson built an amplitude interferometer capable of disproving the existence of the aether that the foundation was laid for the special theory of relativity. The Michelson interferometer was used in this century to measure the angular diameters of the red giant Betelgeuse and of many other stars [Swen 87]. The amplitude interferometer had two difficulties in measuring angular sizes of stars accurately. Better resolving power required increasing the size of the device, which introduced mechanical instabilities. More importantly, atmospheric turbulence imposes random relative phase shifts that destroy the interference signal. Hanbury Brown and Twiss (HBT) proposed a conceptually different interferometer in response to these shortcomings in 1954 [Hanb 54], and the theory of the effect was refined in a series of papers [Hanb 57a, 57b].

The difference between intensity and amplitude interferometry can be understood from Figure 1.1 [Boal 90]. The finite sized source emits particles from points S_1 and S_2, which are later observed at points P_1 and P_2. In *amplitude* interferometry, the points P_1 and P_2 could be slits through which the particles pass. They would then interfere constructively or destructively at various points on a screen located behind the points, producing the traditional fringe pattern. Knowledge of the slit size and measuring fringe visibility could then provide information regarding the source size and the degree of coherence of the light emitted from points P_1 and P_2. In *intensity* interferometry, the two–particle coincidence yield n_{12} and the single–particle yields n_1 and n_2 are measured. In contrast to the Young experiment, the signal is maximal when the emission from P_1 and P_2 is incoherent. From these measurements, a correlation function $C(\mathbf{p}_1,\mathbf{p}_2)$ is constructed through the relation:

$$C(\vec{p}_1,\vec{p}_2) = 1 + R(\vec{p}_1,\vec{p}_2) = \frac{\langle n_{12}\rangle}{\langle n_1\rangle \cdot \langle n_2\rangle}. \qquad (1.1)$$

Information about the source size can be extracted from the correlation function in a two particle coincidence measurement.

The coincident yield, n_{12}, is influenced by quantum statistics (for identical particles) and by the interaction between the two detected particles. For measurements of non–interacting identical bosons, e.g. photons and neutral pions, the correlations arise due to the symmetrization of their relative wave function: the presence of one boson in a particular momentum state will enhance the probability that another will be found in the same state. The size of the correlation depends upon the separation of the bosons upon emission. Hence, the two–photon correlation function is sensitive to the source size.

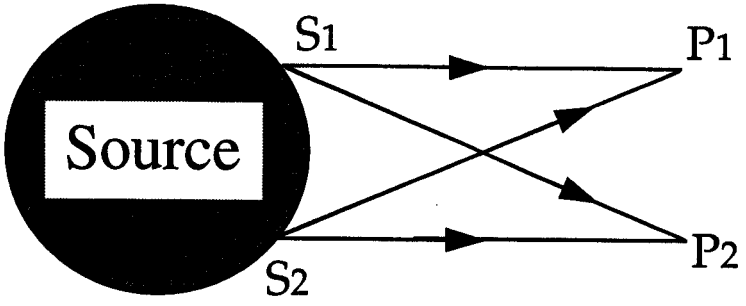

Figure 1.1 Schematic diagram underlying the principle of interferometry.

Although the technique of intensity interferometry was originally intended for two–photon correlations, it was quickly applied to other particles, including charged fermions and bosons. The first such application, by Goldhaber, Goldhaber, Lee and Pais studied pion correlations in proton–antiproton annihilation at about 1 GeV [Gold 59, Gold 60]. More recently, two–pion correlation studies have been used extensively to study the shapes, sizes and lifetimes of sources created in elementary particle and high energy nuclear collisions [Boal 90]. This technique will be an integral part of the search for

signatures of the quark–gluon plasma at the Relativistic Heavy Ion Collider (RHIC) in the early part of the next century.

The use of two–*proton* intensity interferometry was proposed by Koonin [Koon 77] to investigate the space–time nature of medium energy heavy–ion collisions. In contrast to the bosonic nature of photons and pions, protons should exhibit an anti–correlation due to their quantum–statistical behavior as fermions. The dominant contributions to the two–proton correlation, however, are final–state interactions due to the strong nuclear attraction and long–range Coulomb repulsion. Each of these three factors has definite consequences on the shape of the two–proton correlation function, which was shown to be highly sensitive to the space–time extent of the source at low relative momentum (less than 50 MeV/c). The two–proton correlation function has been used to study medium energy heavy ion collisions over a wide range of bombarding energies [Boal 90]. It may also provide information about the liquid–gas phase transition in nuclear matter [Prat 87].

1.3 The Two–Proton Correlation Function

Two protons which are emitted from an excited nuclear system will repel each other through the Coulomb force and attract one another through the nuclear force. In addition to these final state interactions, quantum Fermi statistics requires that the two–proton wavefunction be antisymmetric. These three effects modify the two–proton distribution, and the magnitude of that modification depends upon the relative separation of the protons upon emission. Dividing the coincidence yield by the single particle yields largely divides out the single particle phase space effects and isolates the correlation caused by the final state interactions.

The attractive S–wave nuclear interaction leads to a pronounced maximum in the correlation function at relative momentum q≈20 MeV/c. This maximum decreases for increasing source size and/or emission time scale. Coulomb

repulsion and Pauli antisymmetrization produce a minimum at q≈0, which becomes more pronounced for sources of smaller space–time extents.

Consider a source of radius r and lifetime τ which emits protons of average speed v. The initial spatial separation of the emitted protons, approximately $r + v\tau$, is greater for longer lifetimes. The correlation function is sensitive to this initial separation, which depends upon source radius *and* lifetime. Figure 1.2 shows the spatial distribution of protons emitted from a source. Larger radii (panel b) or longer lifetimes (panel c) produce larger emission zones. Larger and smaller emission zones can be discriminated by analyzing the peak height of the two–proton correlation function; smaller emission zones have larger peaks. The nuclear resonance (at q=20 MeV/c) is spherically symmetric due to its S–wave nature. Furthermore, Coulomb repulsion is dominated by the $\ell = 0$ partial wave for spatial separations less than the two–proton Bohr radius of 58 fm. Therefore, these final state interactions are sensitive only to the size (not shape) of the emission zone; panels b and c cannot be distinguished from one another.

However, information regarding the shape of the distribution of emitted protons may be extracted from quantum statistical effects. The Pauli antisymmetrization requirement of the two–proton relative wavefunction is directionally sensitive for values of relative momentum, $\vec{q}$, and relative position, $\vec{r}$, which satisfy $|\vec{r} \cdot \vec{q}| \approx \hbar$ [Koon 77, Pratt 87, Awes 88]. In particular, correlation functions are suppressed over a range $q_i \leq \hbar / r_i$, for each Cartesian coordinate i. Since the distribution of emitted particles (such as in panel c) is elongated in the direction of total proton momentum, $\vec{P} = \vec{p}_1 + \vec{p}_2$, (measured in the system's center–of–momentum frame) this vector can be used to exploit the directional sensitivity of the Pauli principle. Correlation functions constructed from proton pairs whose relative momentum, $\vec{q} = \frac{1}{2}(\vec{p}_1 - \vec{p}_2)$, is oriented along the short dimension of the distribution (transverse to $\vec{P}$) will be suppressed when compared with correlation functions constructed from pairs whose relative

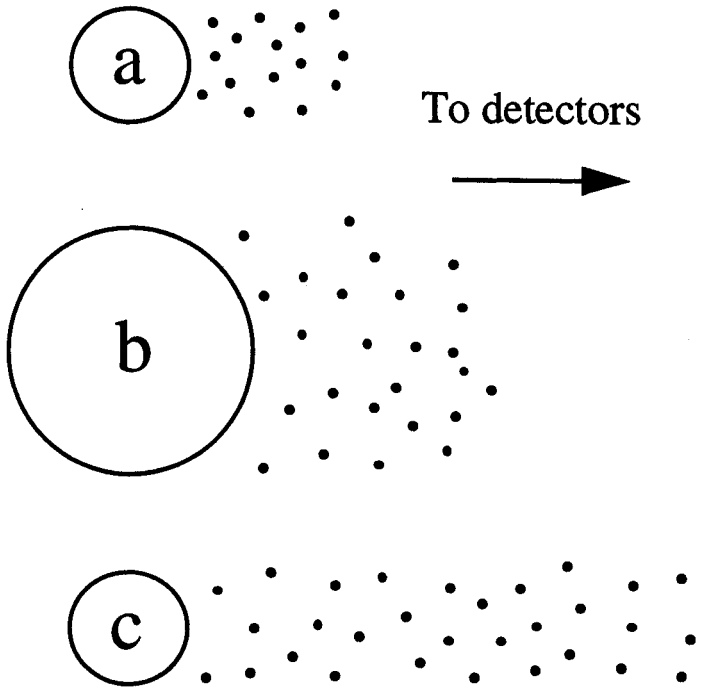

Figure 1.2. Spatial distribution of emitted protons from (a) a small source of short lifetime, (b) a large source of short lifetime and (c) a small source of long lifetime.

momentum is oriental along the long dimension of the distribution (parallel to $\vec{P}$). Such cuts are performed, in practice, by analyzing the angle between relative and total proton momenta, $\psi = \cos^{-1}\left(\vec{P}\cdot\vec{q}/Pq\right)$.

1.4 Motivation

The two–proton correlation function has been shown to have a dependence on the magnitude of the total proton pair momentum, $P = |\vec{p}_1 + \vec{p}_2|$, for many systems over a range of beam energies [Lync 83, Chen 87c, Poch 86, Poch 87, Awes 88, Gong 90b, 90c, 91b, Lisa 91, 93a, 93b, Hand 94]. Higher momentum protons have a larger correlation peak height, indicative of emission from a smaller source. This dependence has been reproduced by calculation of the Boltzmann–Uehling–Uhlenbeck (BUU) dynamic transport model [Gong 90c, 91b, Baue 92a]. More recently, measurements of energy integrated (but impact parameter gated) two–proton correlation functions have shown that central collisions result in a larger source than peripheral collisions, consistent with a geometric interpretation of the reaction zone [Lisa 91, 93a, 93c]. The BUU model predicts a qualitatively similar trend. It was able to reproduce the detailed momentum dependence of the correlation function for central collisions of ^{36}Ar+^{45}Sc at E/A = 80 MeV, but it under predicted the peak height in more peripheral collisions (especially for more energetic protons) [Lisa 93a, 93c].

Another important result from this analysis was the first experimental observation of a difference between longitudinal ($\psi \approx 0°$) and transverse ($\psi \approx 90°$) correlation functions consistent with a finite–lifetime effect [Lisa 93b, 93c], using the technique described in the previous section. Past experiments had failed to identify such a directional dependence, possibly because a clear characterization of emission sources had not been achieved. Comparisons of these directional correlation functions with schematic sources were consistent with a Gaussian source of radius 5 fm and lifetime 25 fm/c. To gain further

insight into the predicted evolution of the source, detailed calculations of the BUU theory were compared with the experimental data [Lisa 93b, 93c] as part of this thesis. We investigated the dependence of the impact parameter and momentum gated directional correlation function on the frame of reference in which the total momentum is defined [Hand 94].

Serious discrepancies between predictions of the BUU model and experimentally measured correlation functions for impact parameter inclusive collisions of $^{40}Ar+^{197}Au$ at E/A=200 MeV were reported by Reference [Kund 93]. Improved agreement was obtained by calculations with the Quantum Molecular Dynamics model (QMD), but these calculations failed to describe the data at E/A=60 MeV where BUU calculations were successful in interpreting impact–parameter inclusive data [Kund 93]. Furthermore, these data show a vanishing minimum in the correlation function at $q \approx 0$, suggesting that the experimental acceptance of the detecting device may have seriously affected the data.

It was the goal of this thesis to investigate the details of proton emission in heavy–ion reactions by measuring the two–proton correlation function's dependence on total momentum and impact parameter, and its directional dependence for collisions of $^{36}Ar+^{45}Sc$ as a function of bombarding energy. We were particularly interested in investigating the claims of Reference [Kund 93] for a symmetric system with improved statistical accuracy capable of impact parameter determination. We also investigated the utility of the correlation function to extract a signature from exotically shaped sources predicted to form in central heavy–ion collisions in this energy domain [Baue 92a]. We measured coincidence yields at bombarding energies of E/A=120 and 160 MeV, using the same high–resolution 56–element hodoscope array employed in the original measurement at E/A=80 MeV [Lisa 93c].

1.5 Organization

Chapter 2 begins with a discussion of the details of the experimental setup, triggering and digitizing electronics. We then discuss data reduction, including particle identification and energy and time calibrations, including time walk correction. Finally, we present our approach of determining the impact parameter of each collisions from data taken with the 4π Array and the construction of an impact parameter distribution appropriate for use with dynamical models.

In chapter 3, we present the theoretical framework in which the two–proton correlation function is calculated, and we present the results of illustrative examples of the space–time ambiguity of correlation functions and the use of directional cuts. Finally, we discuss the construction of the correlation function from measured data.

Chapter 4 presents the BUU transport model's predictions of the directional correlation function for collisions of $^{36}Ar + ^{45}Sc$ at E/A=80 MeV. Sensitivities to the motion of the emitting source are discussed for central and peripheral collisions. Comparisons of these simulations with the data measured by M.A. Lisa [Lisa 93a, 93b, 93c] are shown.

Chapter 5 deals with the BUU prediction of toroidally shaped sources [Baue 92a, Gros 92, Bord 85, Xu 93 and Hand 94]. We investigate the possibility of extracting a signature of such an exotically shaped distributions using the two–proton correlation function by presenting a step–by–step approach which incorporates increasingly realistic assumptions.

In chapter 6 we discuss correlation functions for $^{36}Ar + ^{45}Sc$ at E/A=120 and 160 MeV. Single proton energy spectra are shown, followed by a discussion of measured correlation functions and comparisons with BUU predictions. We show the results of varying BUU input parameters. The importance of particle–unstable fragment production in correlation measurements is discussed and directional correlation functions are presented.

A summary and conclusions are given in chapter 7. Most of the results presented in this dissertation have been submitted to refereed scientific journals for publication [Hand 94, Hand 95a, Hand 95b].

Chapter 2 – Experimental Details and Data Reduction

This thesis project involves two experiments which continue the study of $^{36}Ar+^{45}Sc$ collisions via two–proton intensity interferometry using the 56–Element Hodoscope [Gong 88, 90a, 91b, 91c] coupled with the MSU 4π Array [West 85, Winf 91, Lisa 93c]. Experimental details are summarized in Table 2.1

Table 2.1 Details of the three $^{36}Ar + ^{45}Sc$ experiments.

Experiment Number	**88026**	**91034**	**93034**
Experimenter	M.A. Lisa	D.O. Handzy	D.O. Handzy
Beam Energy/Nucleon	80 MeV	120 MeV	160 MeV
Target Thickness	10 mg/cm^2	40 mg/cm^2	40 mg/cm^2
Beam Intensity	3×10^8 particles/sec	3×10^7 particles/sec	5×10^7 particles/sec
Hours Approved	216	252	360
Number of p–p coincidences recorded	2.1×10^6	1.2×10^6	3.1×10^6
4π Configuration	Ball + Forward Array	Ball + Forward Array	Ball + High Rate Array
Species Resolved in Hodoscope	p,d,t,^{3}He,^{4}He	p,d,t,^{3}He,^{4}He	p,d,t
Dates of Run	June 1991	November 1992	August 1994

In this chapter, we discuss the detectors, their processing electronics and energy and time calibrations. Finally, we discuss impact parameter selection.

2.1 Detector Elements

A closely–packed array of 56 Si–CsI(Tl) telescopes [Gong 88,90a,91b,91c] was used to detect the light charged particles p, d, t, ^{3}He, and ^{4}He. All 56 of the telescopes, as well as the vacuum chamber used to mount the hodoscope onto the 4π Array had been previously constructed for the theses of W.G. Gong [Gong 91c] and M.A. Lisa [Lisa 93c]. Figure 2.1 shows a schematic drawing of the coupling of the two devices.

2.1.1 56–Element Hodoscope

Each hodoscope element consisted of a thin Si ΔE–detector backed by a thick CsI(Tl) E–detector. We used Si surface barrier detectors of 300 and 400 μm thickness and active areas 450mm^2. Each Si detector was attached to the hodoscope's mechanical support structure [Lisa 93c] using a brass mount, the front face of which was covered by a thin (~10μm) Ta foil to suppress signals from electrons and photons. Typical bias voltages ranged from 100 to 200 volts, and each raw ΔE signal was sent to a preamplifier (in vacuum) before being processed by the electronics logic.

Behind the Si detectors were CsI(Tl) crystals [Gong 91c, Lisa 93c] of length 10 cm and diameter 4 cm. Their signals were read out with PIN diodes of active area 2cm x 2cm attached to the back end of the crystals; preamplifiers for these detectors were contained in the same casings as the crystals.

The telescopes, each of which subtended a solid angle of $\Delta\Omega$=0.37 msr, were packed with a nearest–neighbor spacing of $\Delta\theta$=2.6°. Figure 2.2 shows polar coordinates of the hodoscope array. Gain drifts, which were reduced by actively cooling the hodoscope to about 20° C, were monitored by pulser input test signals for both the Si and CsI(Tl) detectors. The gains were found to be stable to within 1% for both experiments.

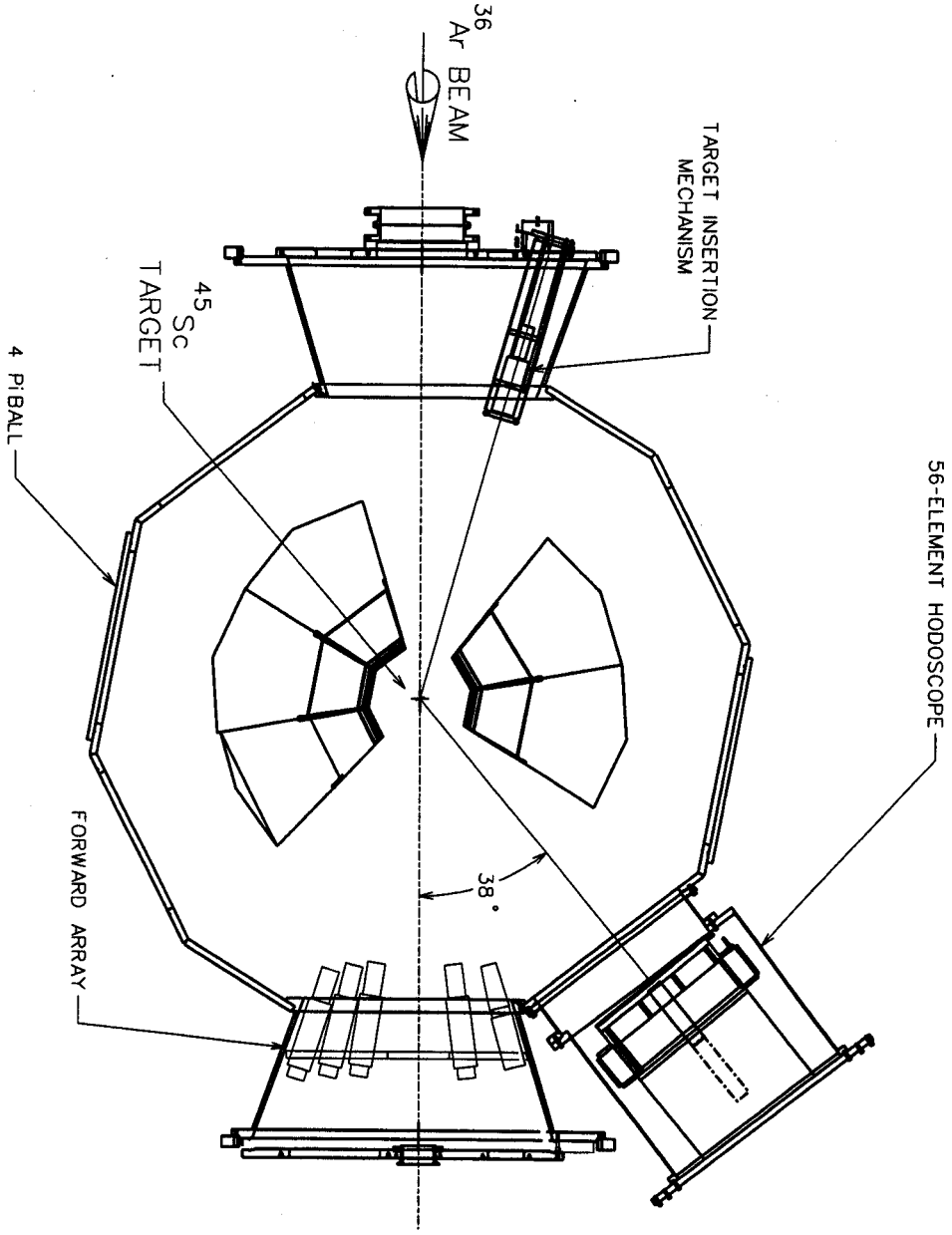

Figure 2.1. Schematic diagram of the 56–element hodoscope coupled to the MSU 4π Array.

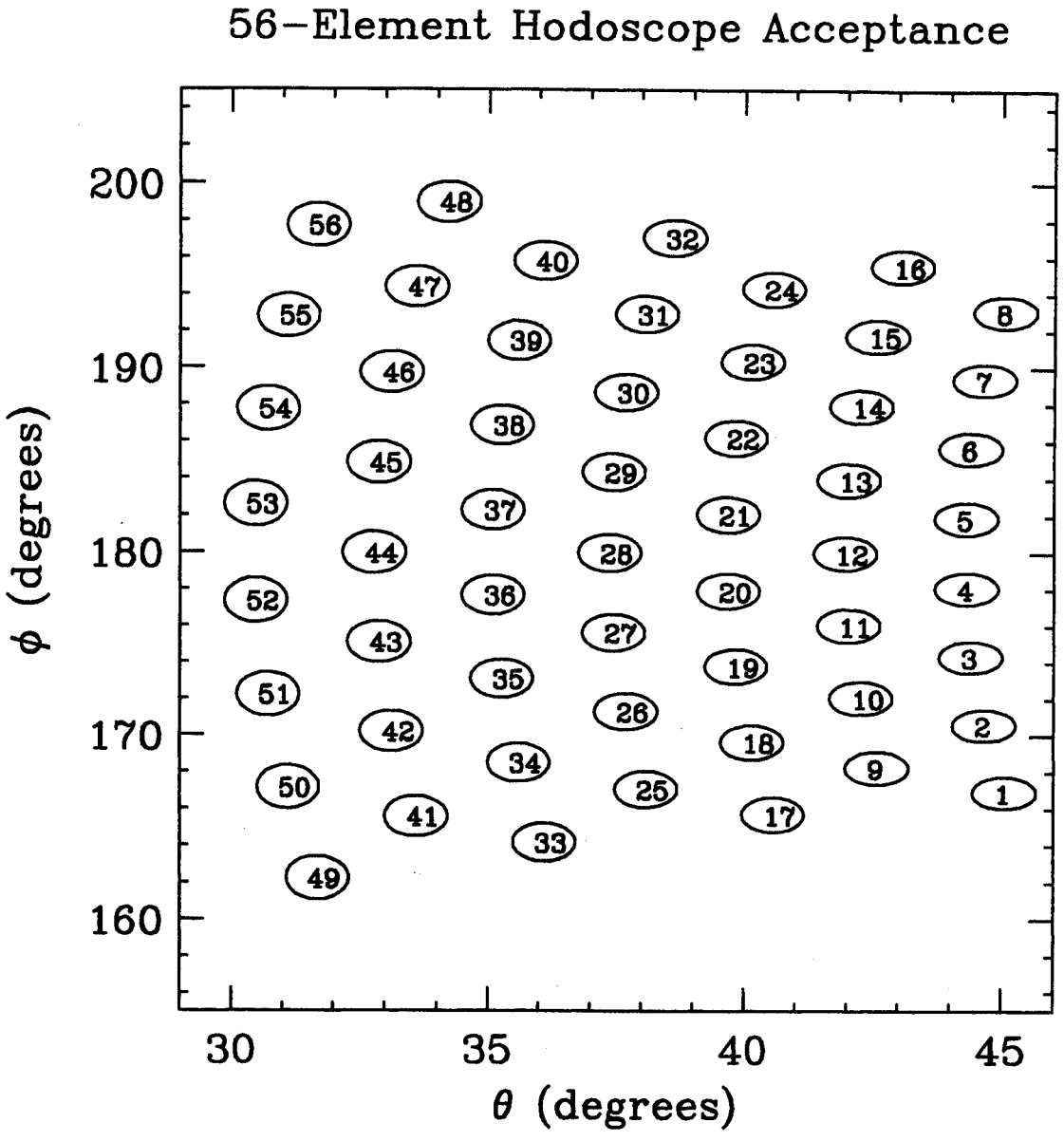

Figure 2.2. Angular coverage of the 56–element hodoscope.

2.1.2 The MSU 4π Array

The MSU 4π Array [West 85, Winf 91] is a closely–packed array of plastic phoswhich detectors covering approximately 87% of 4π. The 4π Array is arranged as a 32–faced truncated icosahedron built of 20 regular hexagonal faces and 12 regular pentagonal faces, as shown schematically in Figure 2.3 Each of the hexagonal (pentagonal) detectors is subdivided into 6 (5) light–charged–particle detector telescopes. The 4π Array is capable of resolving nuclear species of Z≈1–18.

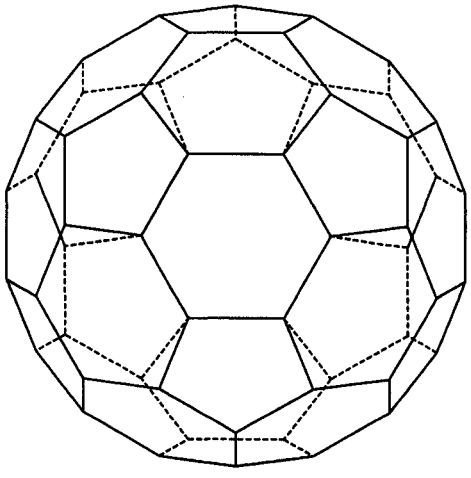

Figure 2.3. A 32–faced truncated icosahedron, the MSU 4π Array geometry.

The 4π Array is composed of 170 "Ball" detectors, and 45 Forward Array detectors. During the two years between the experiments, the 4π Array augmented it's Forward Array (FA) to be geometrically more efficient, by about a factor of two. This improved device is called the High Rate Array (HRA). A schematic diagram of the FA and the HRA is shown in Figure 2.4.

The 4π Array is made of 215 phoswhich telescopes, each of which is composed of a thin "fast" plastic scintillator optically coupled to a larger "slow" plastic scintillator. Pulse–shape discrimination of each telescope's output signal is used to separate the fast (rise time≈1ns, fall time≈3.3 ns) and slow (rise time≈25 ns; fall time≈180 ns) components.

The minimum energy required to enter the "slow" portion of the detector (punch–in energy) depends on particle type, and these values are listed in Tables 2.2 and 2.3 for the Ball and the FA respectively. The HRA and the FA have virtually identical punch–in energies.

Table 2.2 Punch–In Energies for Ball Detectors

Particle Type	Punch–In Energy (MeV)	Particle Type	Punch–In Energy (MeV)
p	17	Li	140
d	24	Be	214
t	28	B	287
He	70	C	380

Table 2.3 Punch–In Energies for Forward– and High–Rate– Array Detectors

Particle Type	Punch–In Energy (MeV)	Particle Type	Punch–In Energy (MeV)	Particle Type	Punch–In Energy (MeV)
p	12	C	259	Al	816
d	16	N	328	Si	927
t	19	O	403	P	1009
He	47	F	472	S	1124
Li	95	Ne	570	Cl	1216
Be	146	Na	636	Ar	1403
B	195	Mg	737		

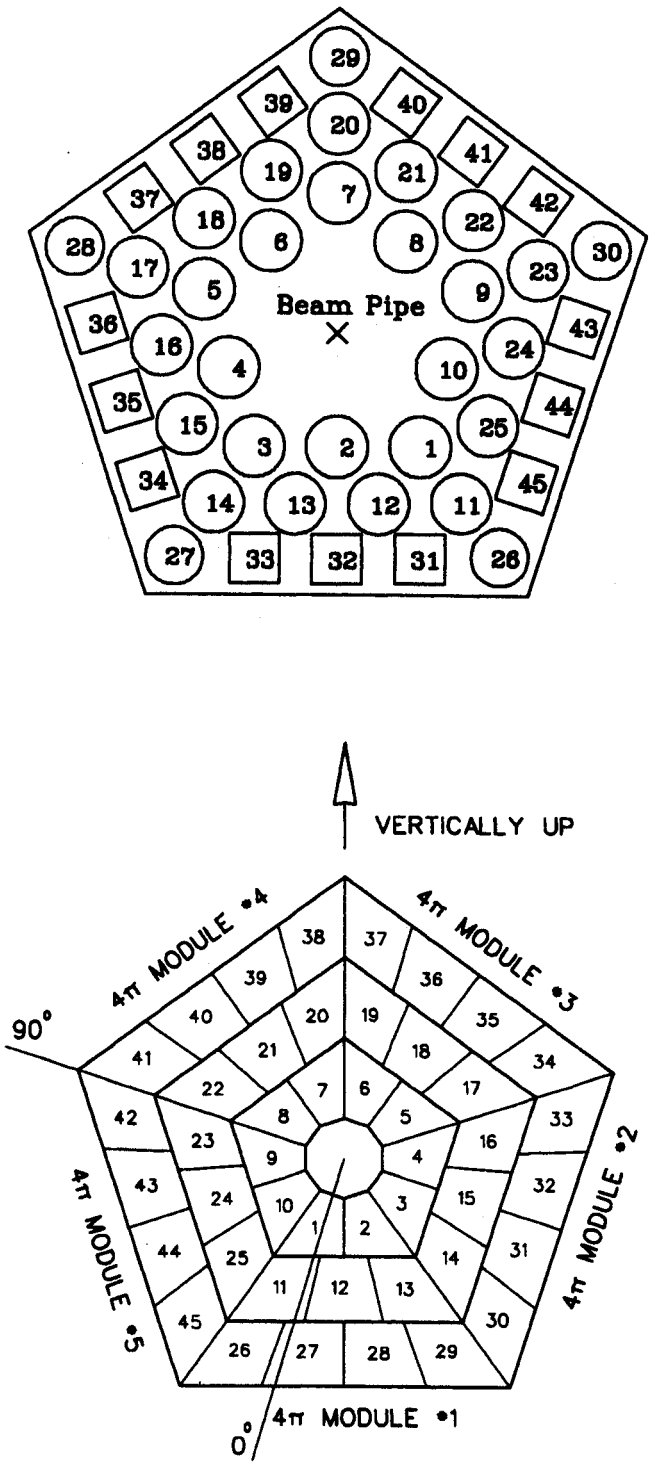

Figure 2.4. Schematic diagram of the front faces of the Forward Array (top) and the High Rate Array (bottom).

2.2 Electronics

The purpose of these experiments was to measure two–proton correlations as a function of impact parameter. The protons were measured in the hodoscope while the impact parameter of each collision was determined from data taken with the 4π Array. The electronics set–up of both of these experiments were based on that used by Michael Lisa for his thesis experiment [Lisa 93c].

Because the 4π detectors had a much faster rise time than the hodoscope detectors, the 4π Array triggered its own ADC's. The digitized information was read into the computer if the slower hodoscope satisfied its trigger condition. Otherwise, the data was cleared in anticipation of the next event. The two detector arrays had independent triggers, both of which had to fire to form a valid event. Events in which the 4π Array fired, but the hodoscope did not, were "fast cleared" before the computer recorded the event. Because of the much greater geometrical acceptance of the 4π Array and because of the large polar angle positioning of the hodoscope, events in which the hodoscope fired but the 4π Array did not were extremely rare. Because these events had no information about the impact parameter, they were ignored in the subsequent off–line analysis.

We used three different "master" triggering conditions. The "Coincidence" trigger demanded that at least two hodoscope detectors fire. Data so taken was used to construct the numerator of the correlation function. We used a second "Singles" trigger in which a minimum of one hodoscope detector fired to have data with which to construct the denominator of the correlation function. Finally, we took short runs with the 4π Array as the trigger to construct an impact parameter scale (see section 2.4).

Shown in Figure 2.5 is a schematic diagram of the electronics used for the two detectors and how they work together.

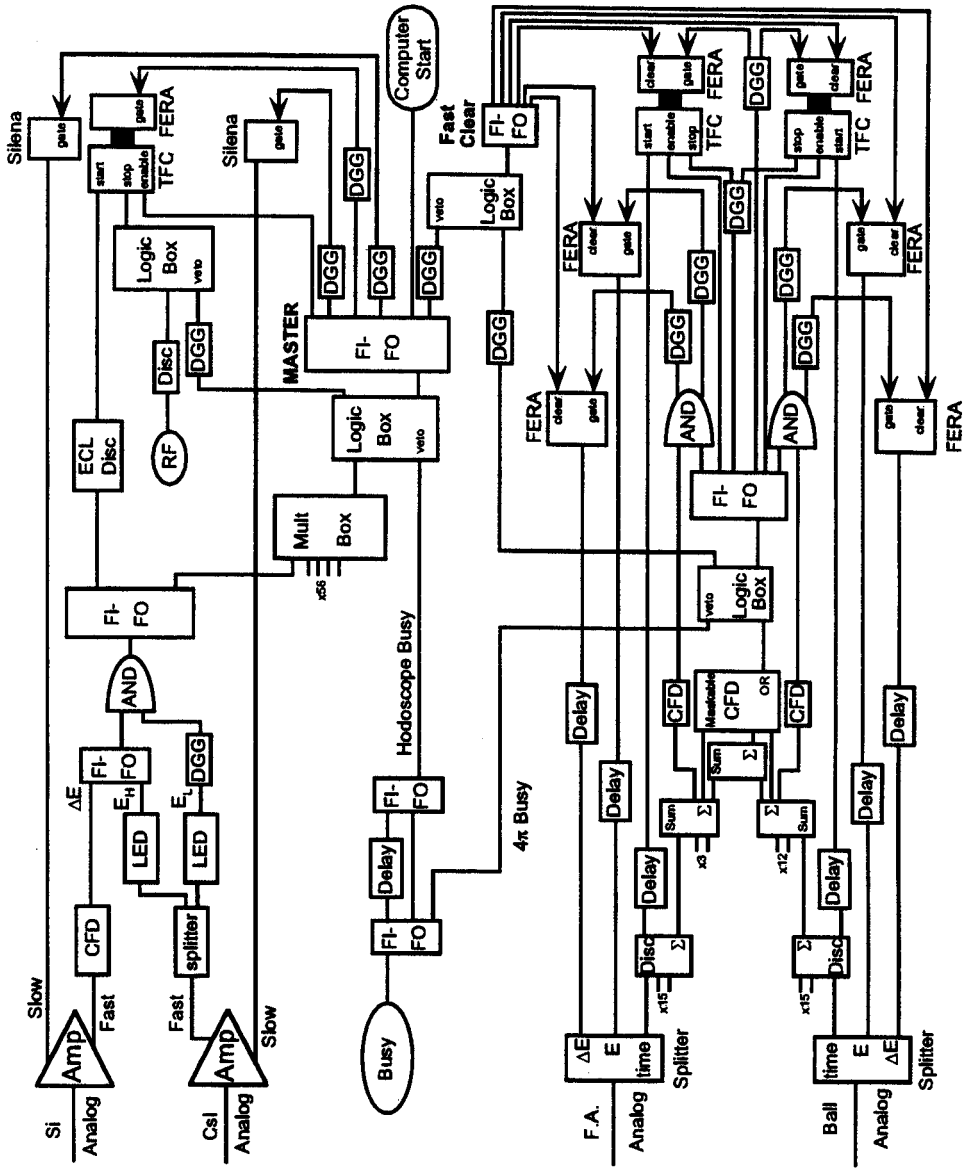

Figure 2.5. Electronics used by the 56–element hodoscope and the MSU 4π Array in digitizing data.

2.2.1 The 56–Element Hodoscope

The electronics logic for each individual telescope is schematically outlined in the upper section of Figure 2.5. The shaping amplifiers provided two outputs: a 'fast' output (with integration time constant $\tau \approx 100$ ns) which was used to construct the trigger logic, and a 'slow' output (with $\tau \approx 3$ μs) which was sent directly to a peak–sensing Silena ADC. In order to detect high–energy protons (which deposit too little energy to reliably trigger the Si detector discriminators), two thresholds were used for the CsI(Tl) detectors. Signals passing the Si threshold (typically ~200 keV) will be denoted ΔE; those passing the low CsI(Tl) threshold (typically ~500 keV) will be denoted E_L; and those passing the high CsI(Tl) threshold (typically ~1–2 MeV) will be denoted E_H. Because we were interested in fast and slow protons, a valid event could have been formed in one of two ways. Simultaneous ΔE and E_L signals were considered valid, which would include low to medium energy protons (which trigger both detector discriminators). High energy protons would produce solitary E_H signals (not triggering the ΔE discriminator), and were also valid. A hodoscope event was considered valid, then, if the following triggering condition was met: $(E_L \cdot \Delta E) + (E_L \cdot E_H)$.

E_L was the only signal present for all valid events; it therefore, was made to determine the timing of each hodoscope event. Since the *second* signal to arrive at an "AND" gate determines the timing of the gate's output, delaying the E_L signal, with a Delay–and–Gate–Generator (DGG), insured that it always determined the timing of the hodoscope event. Since the timing of a discriminator's output depends upon the magnitude of the analog input pulse, our timing technique had the advantage that this "walk" or "slewing" effect was determined by the E_L discriminator. By using a Leading–Edge Discriminator (LED), we introduced a *well–defined* particle dependent slewing effect which was later corrected for off–line.

The output of the final hodoscope "AND" in Figure 2.5 was used for two purposes: as an input into the overall "hodoscope master," and for timing relative to the RF cycle of the cyclotron. We used a LeCroy TFC–FERA system to digitize the time information which requires (in order): an enable, a start and a common stop. The enable was generated by the hodoscope master, and the individual detector starts were generated by the individual valid detector signals. However, the hodoscope master could arrive as much as 200ns after the first detector fires (due to walk). In order to insure that the starts arrived after the enable, a rather unconventional delay was developed by M.A. Lisa [Lisa 93c]. The detector masters were re–discriminated with an ECL discriminator (width≈ 500 ns), and sent along modified cables which physically flipped the signals, the effect of which is to conjugate the logic. The trailing edge of the (now inverted) signal is interpreted by the TFC (Time to FERA Converter) as a leading edge, thus effectively delaying the start by the 500 ns "width." The common stop to the TFC was provided by a discriminated RF signal in coincidence with a hodoscope master.

During the analysis of the first experiment, we noticed that for certain detectors, the particle identification lines in the E–ΔE matrices were discontinuous; very low values of either variable were suddenly "dropped" to lower channel numbers than expected. A subsequent bench test with the Silena ADC showed that this problem is reproduced when the gate width is larger than about 2 μs, because the ADC digitizes the *first* (not the largest) peak it encounters within the gate. Using a wider gate allows ripples in the upward sloping signal to be misinterpreted as the peak. In our second experiment, we set all Silena gates to less than 1.5 μs and did not observe this phenomenon.

2.2.2 The MSU 4π Array

Signals from the Ball and Forward Array photomultiplier tubes enter "splitter boxes" designed especially for the 4π Array. These passive splitters

divide the analog signals into three identical signals known as "fast," "slow," and "timing." Both the "fast" and "slow" signals are appropriately delayed and sent to FERA's (Fast Encoding Readout ADC's) where they undergo charge integration and digitization.

The "timing" signal's processing is more complicated. First, it is discriminated in an Phillips Scientific 7106 discriminator. The individual discriminator outputs are themselves delayed and sent to TFC start inputs. These discriminators also have a "sum" output which generates a voltage level of –50mV for each firing channel; these are used to determine the multiplicity of each event. The 45 Forward Array (or High Rate Array) detector "timing" signals pass through three Phillips discriminators, the "sum" outputs of which are then linearly added in a "summer" box, providing a measure of the Forward Array multiplicity.

The 170 Ball detector "timing" signals are similarly processed to measure the "Ball" multiplicity. Finally, the Ball sum signal and forward array sum signal are added to measure the overall multiplicity. These three "sum" signals (Ball, FA and "total") are each sent to a maskable, CAMAC programmable CFD (Constant Fraction Discriminator). By setting which of these three sum signals to consider, through the discriminator's masking capabilities, one forms the 4π trigger by programming the discriminator's threshold. In this way, one can trigger on "Ball," "Forward Array," or "Total," and one can set the minimum multiplicity through the discriminator threshold.

2.2.3 Master Electronics

As described above, the usual trigger conditions required 2 hodoscope detectors firing along with a minimum number of 4π detectors. The 4π Array self–gated its own ADC's and would fast–clear that digitized information if no hodoscope master appeared.

The vetoing of the triggers due to the computer–busy was affected by the large difference in arrival times between the hodoscope master and the 4π

master. We used the original 4π computer busy to veto the 4π master signals, and we used a stretched "hodoscope busy" to veto hodoscope master signals. For the higher energy experiment, we adopted a different method to veto the master signals. In this last experiment, we used a delayed (not stretched) hodoscope busy signal. Furthermore, we explicitly required a 4π master (appropriately delayed) in coincidence with every hodoscope master before issuing gates to the ADC's. This change prevented the possibility of events being written to tape in which hodoscope data was present without corresponding information from the 4π Array. Figure 2.6 shows the timing of the master electronics.

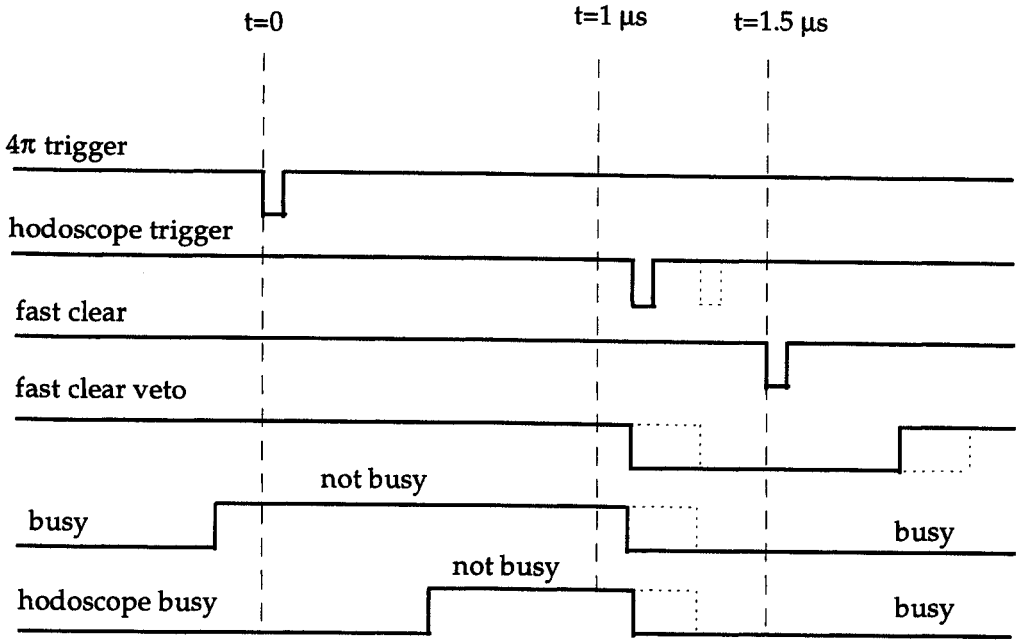

Figure 2.6. Master electronics timing diagram. The dashed lines indicate the effect of the (approximately) 200 ns "jitter" in the relative time between 4π triggers and hodoscope triggers. The fast clear is created about 1.5 μs after the 4π trigger, and the fast clear veto is issued immediately following a hodoscope trigger.

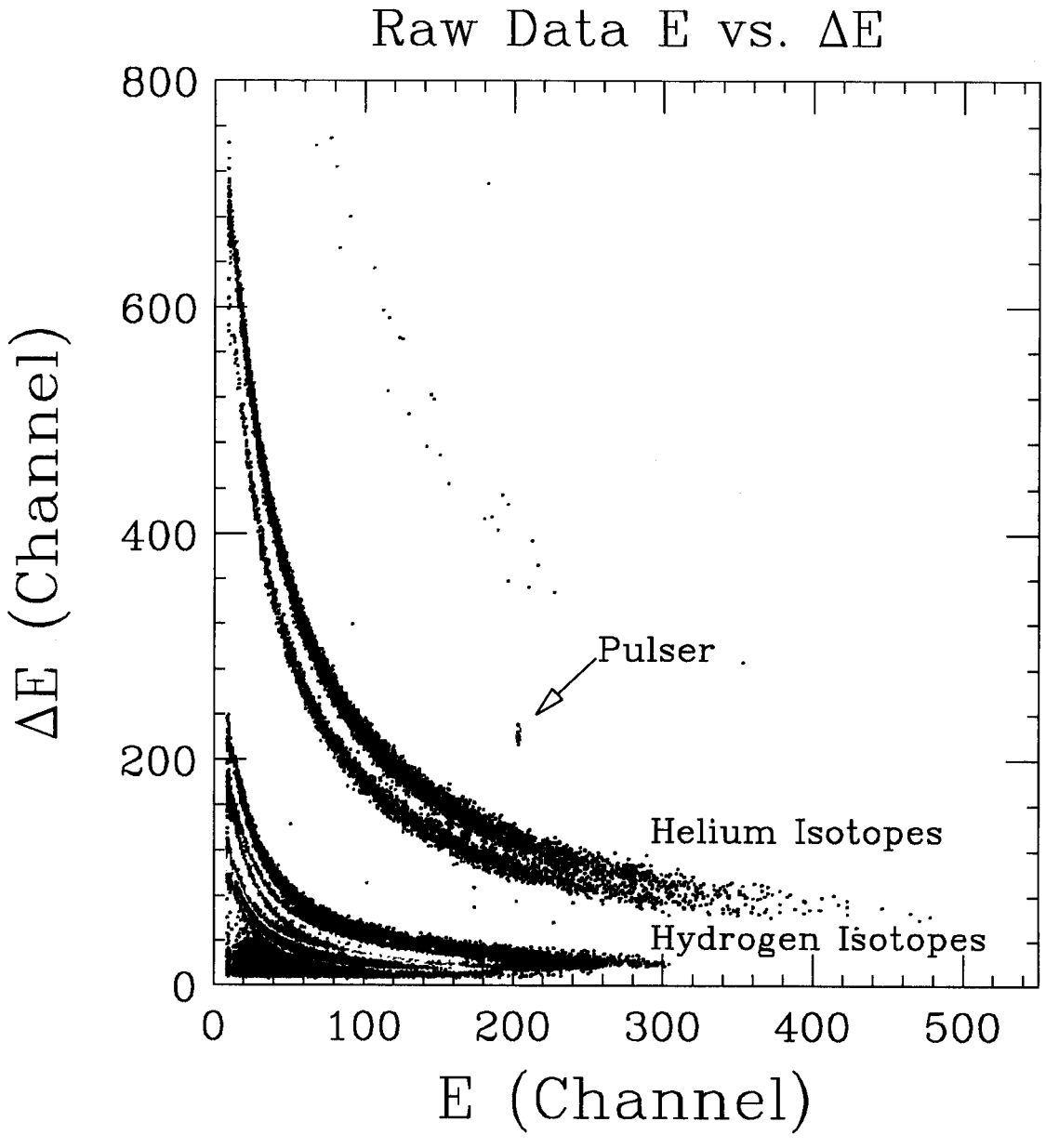

Figure 2.7. 2–dimensional E vs. ΔE for a typical hodoscope detector. Isotopes separate into hyperbolic bands on this logarithmic scale.

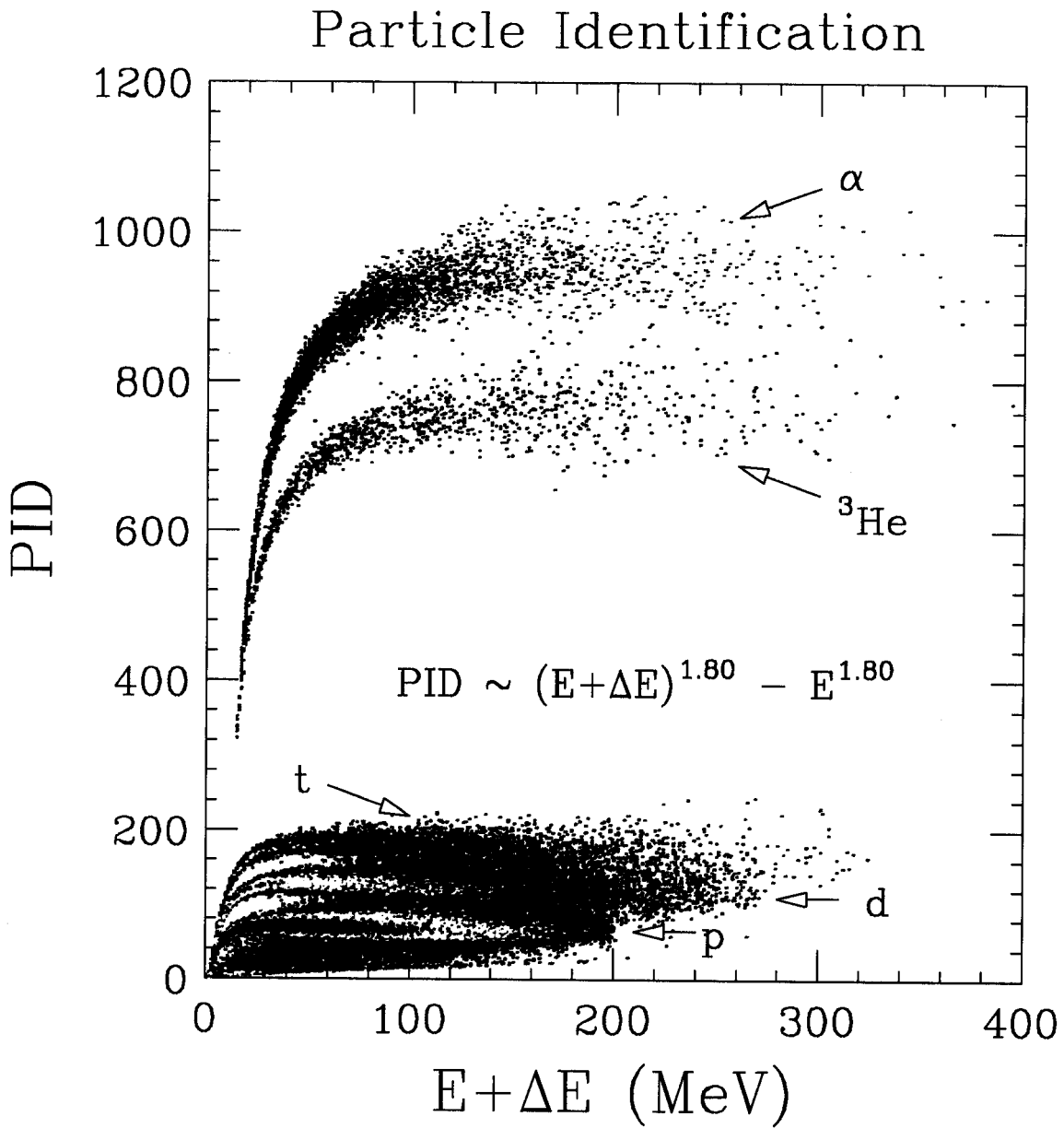

Figure 2.8. 2–dimensional total energy vs. PID plot showing linear separation of isotopes. Again, logarithmic density scale is used.

2.3 Calibrations

In this section, we discuss our methods for identifying particle species, and calibrating the energy and time signals.

2.3.1 The 56–Element Hodoscope

Since the energy calibration of scintillating detectors depends upon the nuclear species, one must first identify the detected particles before calibrating. Figure 2.7 shows a plot of CsI(Tl) detector E–signal vs. Si detector ΔE–signal for one of the hodoscope detectors in which the different nuclear species can be seen as hyperbolas. Although clear bands are visible in this representation, separation of protons from deuterons at high energy becomes difficult due to limited channel resolution. We transform this E–ΔE map into a linearized E–PID matrix which makes more efficient use of the two dimensional space. Particle identification in areas of low resolution is then accomplished by linearly extrapolating from regions of higher resolution. Figure 2.8 shows this function, PID ~ $(E+\Delta E)^{1.80} - E^{1.80}$, vs. total particle energy. Linear bands defining regions in the E–PID space were then used to clearly identify the nuclear species: p,d,t, ^{3}He and α. One–dimensional projections of these curves onto the PID axis for various cuts in total energy are shown in Figure 2.9, where one sees that clean separation of the nuclear species is achieved over a wide range of proton energy.

The Si detectors were calibrated using a highly linear capacitor and pulser system, following the method described in [Gong 91c] and [Lisa 93c]. Si calibrations were found to be linear, in agreement with these previous studies.

Calibration of the CsI(Tl) crystals was achieved by scattering alpha particles off of a 10 mg/cm^2 $(CH_2)_n$ target at E/A=25,30 and 40 MeV into the hodoscope detectors. Each beam was run for approximately 8 hours, resulting in the reactions listed in Table 2.4 which provided calibrations accurate to about 1% for all 5 nuclear species.

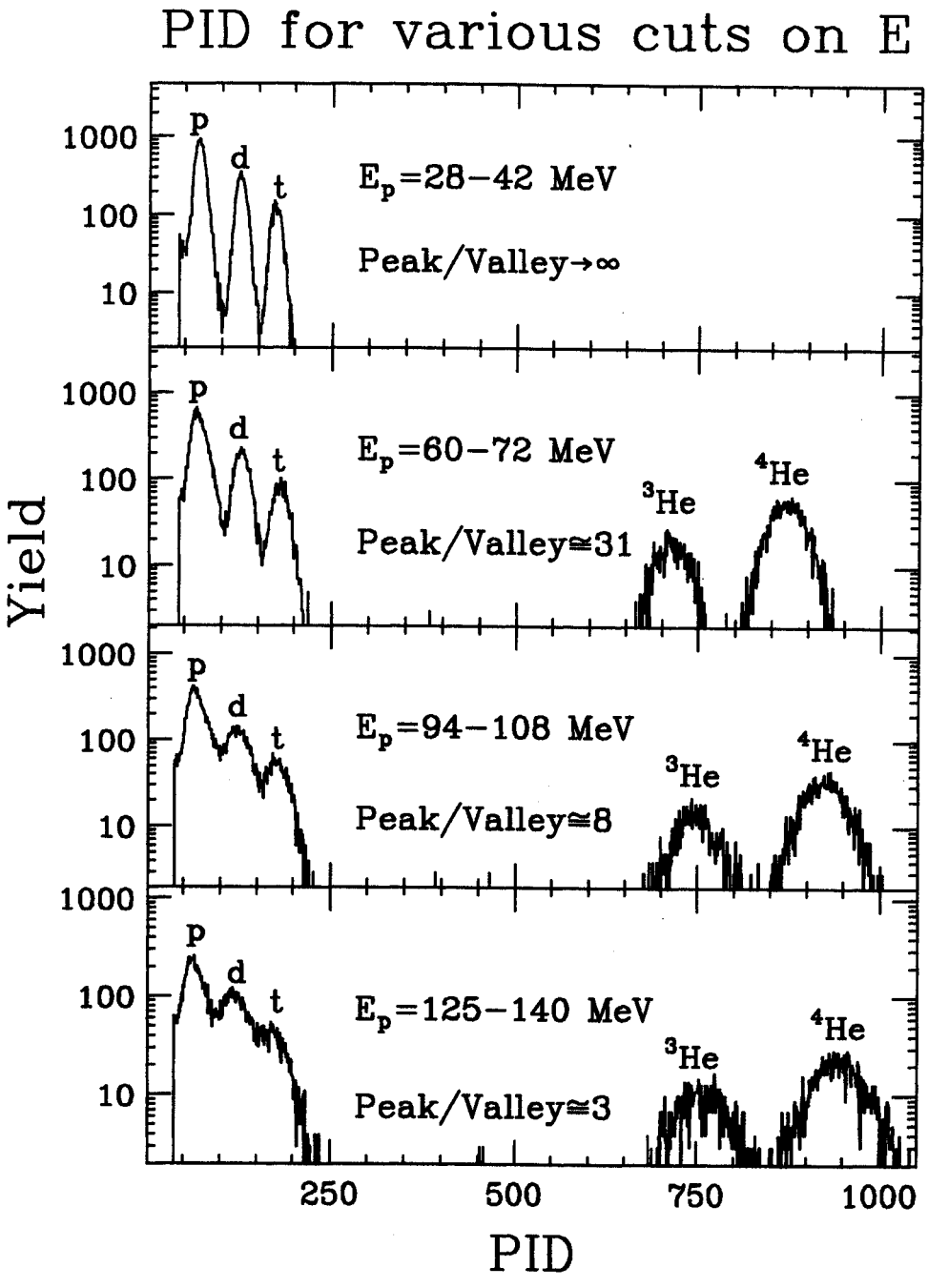

Figure 2.9. 1–dimensional projections of PID using thin cuts in energy, showing particle identification resolution as a function of energy.

Table 2.4 Calibration Reactions

Particle Type	Calibration Reaction	State Scattered off in Residual Nucleus Residual Nucleus: J^{π} (energy in MeV)
p	p (α,p) α	N/A: knockout reaction
d	^{12}C (α,d) ^{14}N	^{14}N: 5^+ (8.96)
t	^{12}C (α,t) ^{13}N	^{13}N: $\frac{1}{2}^-$ (g.s.), $\frac{5}{2}^+$ / $\frac{3}{2}^-$ (3.55, 3.51), $\frac{3}{2}^-$ (6.89)
^{3}He	^{12}C (α, ^{3}He) ^{13}C	^{13}C: $\frac{1}{2}^-$ (g.s.)
^{4}He	^{12}C (α,α') ^{12}C*	^{12}C: 0^+ (g.s.), 2^+ (4.44)

Figure 2.10 shows the single particle energy spectra resulting from the calibration run at E/A=30 MeV. The calibration curves were assumed to be linear, based on previous work with these detectors [Gong 91c, Lisa 93c]. Losses in the Ta foil and in the ΔE detector were accounted for, and in each case the centroid of the scattering peak was used to determine the energy calibration using two–body kinematics. Calibration curves for a representative detector are shown in Figure 2.11. In the most backward detectors, in which deuteron peaks could not be extracted, we averaged the proton and triton calibrations to provide an approximate deuteron calibration. This method was compared with the true calibration in more forward detectors, and Figure 2.11 shows that the "approximate" calibration (dashed line in deuteron panel) is nearly indistinguishable from the true calibration (solid line). Figure 2.11 also shows the linearity of the Si detector calibration for this telescope.

Energy losses through the Ta foils and ΔE detectors were calculated using the Littmark–Zieger tables [Litt 80], following Reference [Lisa 93c]. To test this method, we also determined the energy loss through the Si detectors using their known calibrations. For the lightest ions, the methods agreed to about 0.1%. However, for ^{3}He, there was substantial disagreement (about 2%). Therefore, we recalibrated the entire device using the measured energy loss through the Si

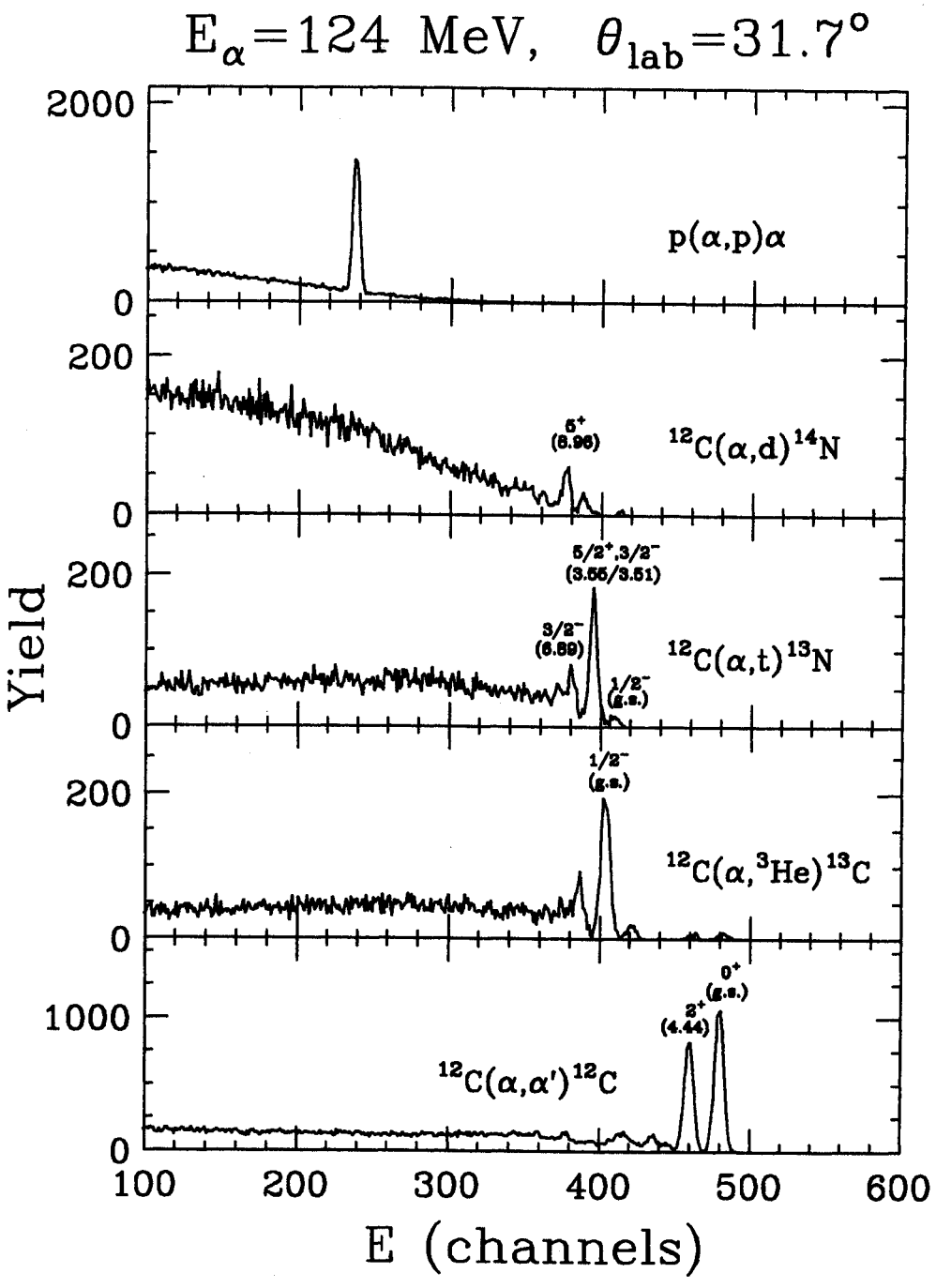

Figure 2.10. Energy spectra gated on detected particle type (p,d,t,^{3}He,α; top to bottom) for our E/A=30 MeV calibration run.

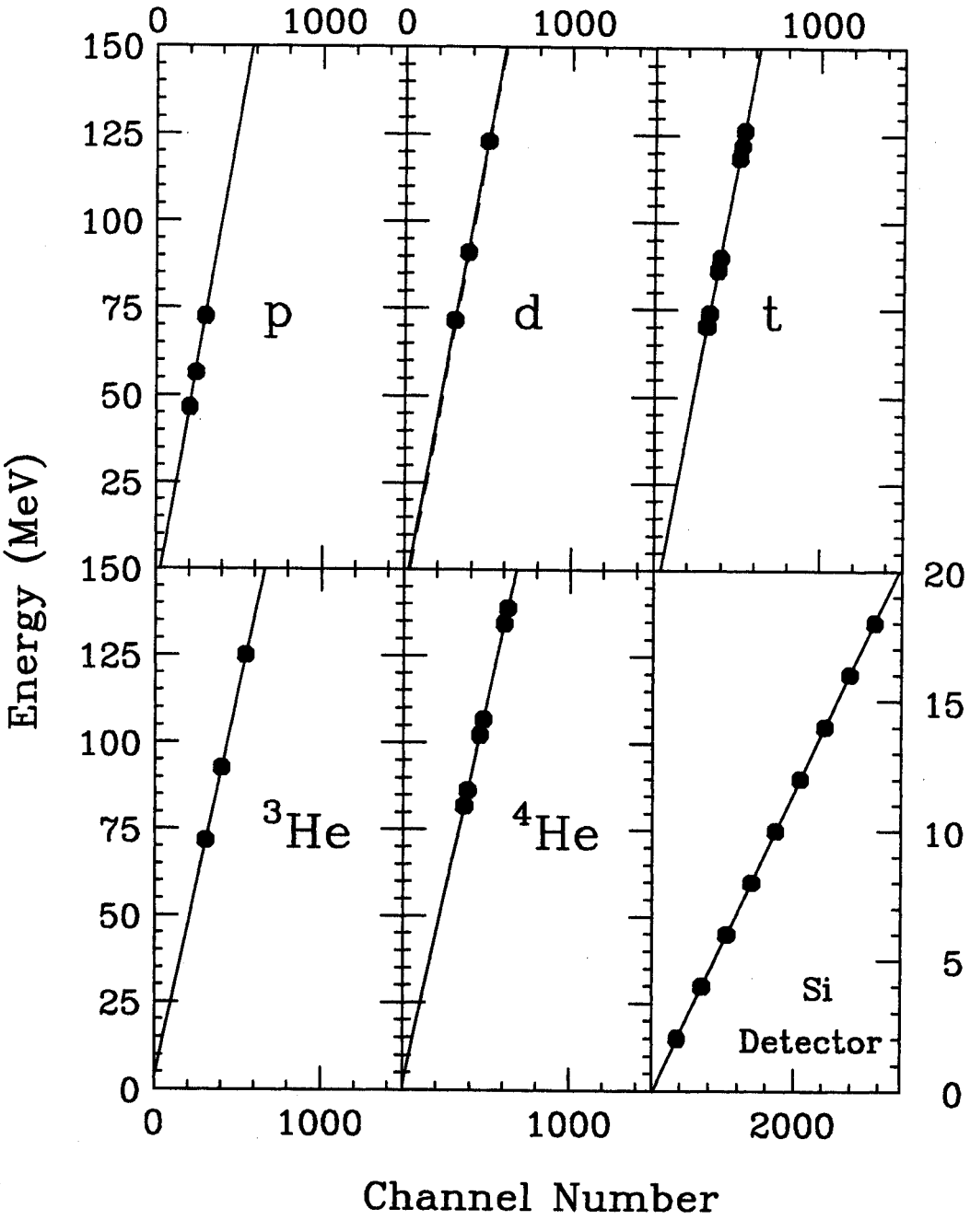

Figure 2.11. Linear calibration curves for a typical hodoscope detector. The dashed line in the deuteron panel is the average of the proton and triton calibrations, which was used for those detectors in which insufficient deuteron statistics prevented a direct calibration.

detectors and used the tabulated values to account only for the thin Ta foil. It should be noted that this discrepancy did not affect the proton calibration of Reference [Lisa 93c] to more than 0.05%, and that the two–proton correlation function was unaffected within its uncertainty.

Any two–particle observable measured in experiments must take into account "real" and "random" coincidences. In our work, misidentification of random coincidences will lead to a suppression of the correlation function, and therefore must be screened.

In both experiments, we recorded the time at which each hodoscope detector fired, relative to the Radio–Frequency (RF) time of the cyclotron, $T_i - T_{RF}$. Calculating $(T_i - T_{RF}) - (T_j - T_{RF}) = T_i - T_j$ then provides a measure of the relative time between the firing of detectors i and j. This variable is plotted, after being summed over all detector pairs recording two protons, in the upper panel of Figure 2.12, where one sees a rather broad distribution due to the effects of discriminator walk [Gong 91c, Lisa 93c]. By assuming a Gaussian shaped amplifier output, $V(t) = E e^{(t-t_o)^2/\tau}$, where E is the particle energy, t is the observed detector firing time, t_o is the "true" firing time, and τ is a particle–type dependent rise time constant, one can easily correct for the energy–dependent walk effect. Solving for t_o, one obtains: $t_o = t - \tau\sqrt{\ln(E/E_{th})}$ where E_{th} is the threshold level of the discriminator. After making this transformation, the relative timing spectrum appears in the bottom panel of Figure 2.12, showing distinct peaks corresponding to different cyclotron beam burst. We defined as "real" events those which fell to within $2\frac{1}{2}$ cyclotron RF bursts of the peak. Proton pairs with relative times in the "random" section of the spectrum were used to correct for the small random background. Since four RF peaks were included in the "random" and five in the "real" definition, we used the relation:

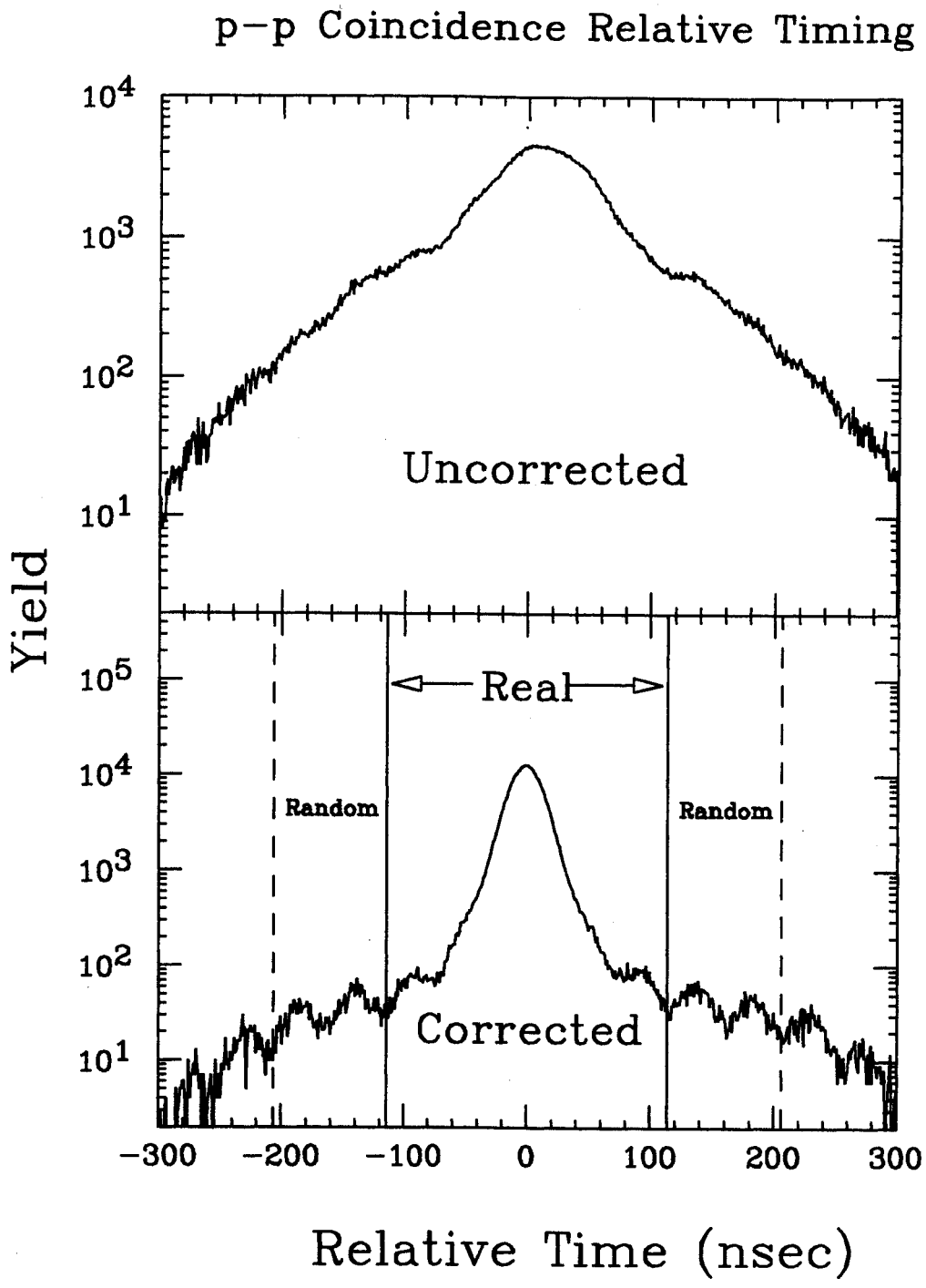

Figure 2.12. Relative timing of detectors both recording protons. The upper panel shows the results before "walk" correction. After the correction (lower panel), the spectrum displays clear peaks corresponding to different cyclotron beam bursts.

"True" = "Real" – (5/4) x "Random." The random contribution amounted to less than 2% of the coincidences for both experiments.

2.3.2 The 4π Array

Particle identification and calibration in the 4π Array was accomplished by analyzing "fast" vs. "slow" spectra. The 4π Group has put together a standard procedure which gain–matches all of their detectors in a systematic and routine way [Wils 91]. Each fast–slow map is "stretched" to fit into the standard detector template. By matching the observed particle lines with predefined "standard" positions, one identifies each species and calibrates simultaneously [Li, T 93 and Cebr 90]. This calibration technique is accurate to approximately 10%.

2.4 Impact Parameter Selection

The impact parameter with which two nuclei collide cannot be determined directly, but it can be roughly deduced from "global" observables which are related to the "violence" of the collisions. Following the work of References [Phai 92, 93b, Hand 94 and Lisa 93c], we studied three commonly used global observables.

1) The charged particle multiplicity, N_C, is the number of 4π detectors that record a charged particle.
2) The total transverse kinetic energy is defined by:

$$E_t = \sum_{i=1}^{N_C} E_i \sin^2(\theta_i) \qquad (2.1)$$

where E_i and θ_i are the kinetic energy and laboratory angle of the i^{th} measured particle by the 4π Array in an event. This definition is appropriate at nonrelativistic energies since

$E\sin^2(\theta) = p_\perp^2/2m$ provides a measure for energy dissipation into velocity components perpendicular to the beam axis.

3) The midrapidity charge, Z_Y, is defined by:

$$Z_Y = \sum_{i=1}^{N_C} Z_i \cdot \Theta\left(y_i - \tfrac{3}{4} y_{tar}\right) \cdot \Theta\left(\tfrac{3}{4} y_{pro} - y_i\right), \qquad (2.2)$$

where $\Theta(x)$ is the standard Heaviside function and y_{tar}, y_{pro} and y_i are the rapidities of the target, projectile, and i^{th} charged particle detected by the 4π Array, in the center–of–momentum system.

In order to reduce the effects of "self–biasing," particles detected in the 56–element hodoscope were not included in the definitions of any of the global observables used to construct the impact parameter.

Phair showed that E_t provides the best measured of centrality for collisions of $^{40}Ar+^{197}Au$ at E/A=50, 80 and 110 MeV [Phai 92, 93b], and Lisa showed the same for collisions of $^{36}Ar+^{45}Sc$ at E/A=80 MeV [Lisa 93c]. The total transverse kinetic energy spectrum, dP/dE_t, for collisions of $^{36}Ar+^{45}Sc$ at E/A=120 MeV is shown in Figure 2.13 for three triggers: Ball (4π multiplicity ≥1) shown in solid squares; Singles (hodoscope multiplicity ≥1) in open diamonds, and Coincidence (hodoscope multiplicity ≥2) in solid circles. Since larger values of E_t correspond to more central collisions, Figure 2.13 shows that requiring particles to enter the hodoscope preferentially selects more central collisions.

Following References [Phai 92, Phai 93b, Hand 94 and Lisa 93c], we construct a reduced impact parameter scale by means of the geometric relation

$$\hat{b}(X) = \sqrt{\int_X^\infty \frac{dP}{dX'} dX'}, \qquad (2.3)$$

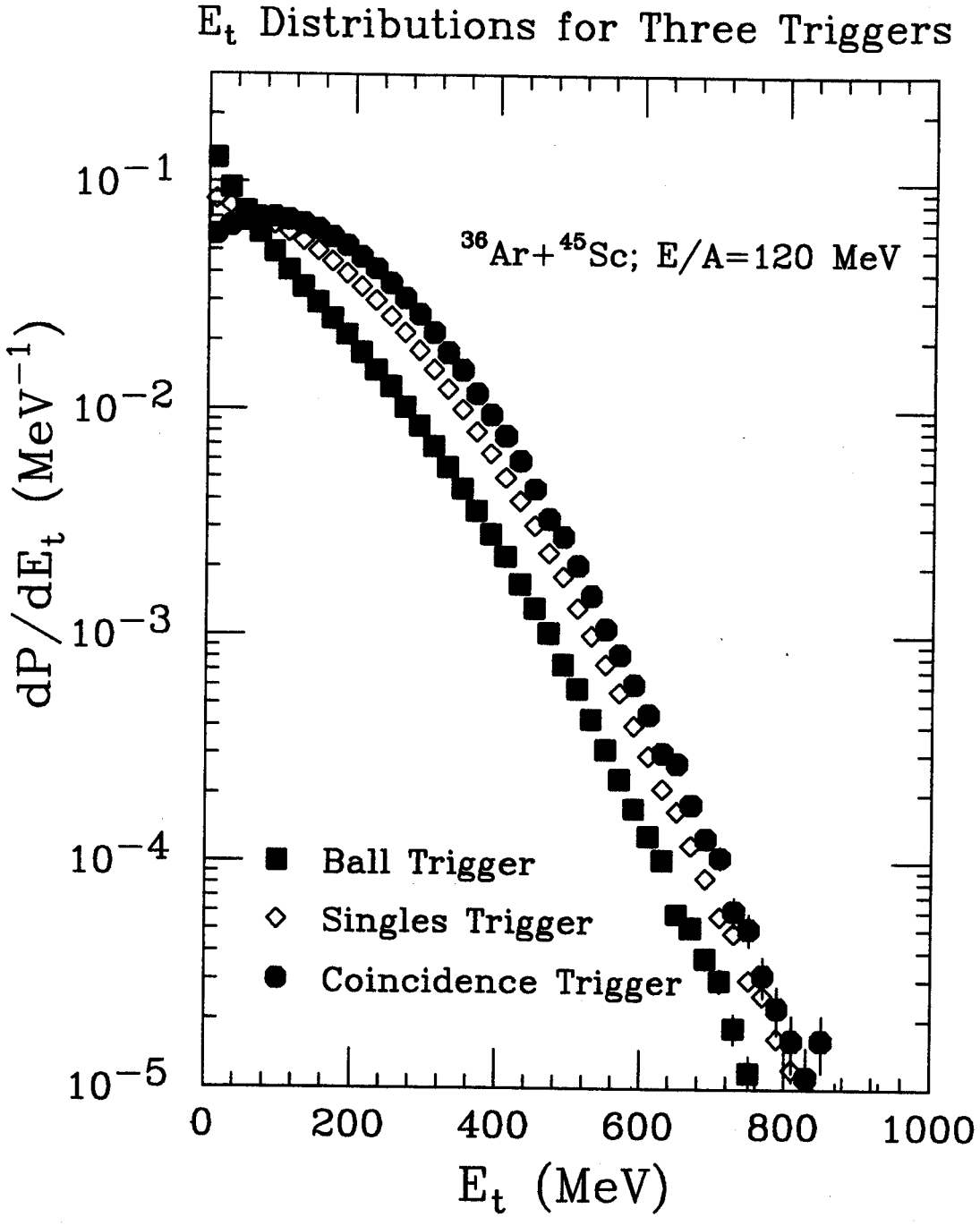

Figure 2.13. Total transverse kinetic energy distributions measured in the 4π Array under the three trigger conditions "Ball," "Singles," and "Coincidence."

where dP/dX is the normalized probability distribution for the global observable X. If the variable X exhibits a strictly monotonic dependence upon impact parameter, b, then $\hat{b}(X) = b(X)/b_{max}$ where b_{max} is the maximum impact parameter for which the measured value of X assumes a nonzero value. Furthermore, we assume that the detecting system has perfect efficiency regardless of impact parameter, from which it follows that with an inclusive (minimum bias) trigger, the probability of observing an event with impact parameter b follows the geometric distribution: dP/db~b.

Figure 2.14 illustrates the relationship between E_t and $\hat{b}(E_t)$ defined by equation 2.3. The top panels show the transverse energy spectra dP/dE_t for the $^{36}Ar+^{45}Sc$ reaction at E/A=120 MeV (left) and at E/A=160 MeV (right). The lower panels show the corresponding reduced impact parameter scales, $\hat{b}(E_t)$, which range from 0 for the most central collisions to 1 for the most peripheral collisions. The analysis of our data focuses on central collisions, defined by $\hat{b}(E_t) = 0.0 - 0.03$.

Through the relationship $\hat{b}(E_t)$, any distribution dP/dE_t can be transformed into a reduced impact parameter distribution using

$$\frac{dP}{d\hat{b}} = \frac{dP}{dE_t} \Big/ \frac{d\hat{b}}{dE_t} . \qquad (2.4)$$

Figure 2.15 presents the reduced impact parameter distribution corresponding to the different experimental triggers for our E/A=120 MeV analysis (the E/A=160 MeV results are very similar). The solid line represents the minimum bias trigger which, by construction, increases linearly with $\hat{b}$. The dot–dashed and dashed lines show the distributions for the single and two–proton inclusive events in the 56–element hodoscope, respectively. Requiring one or more

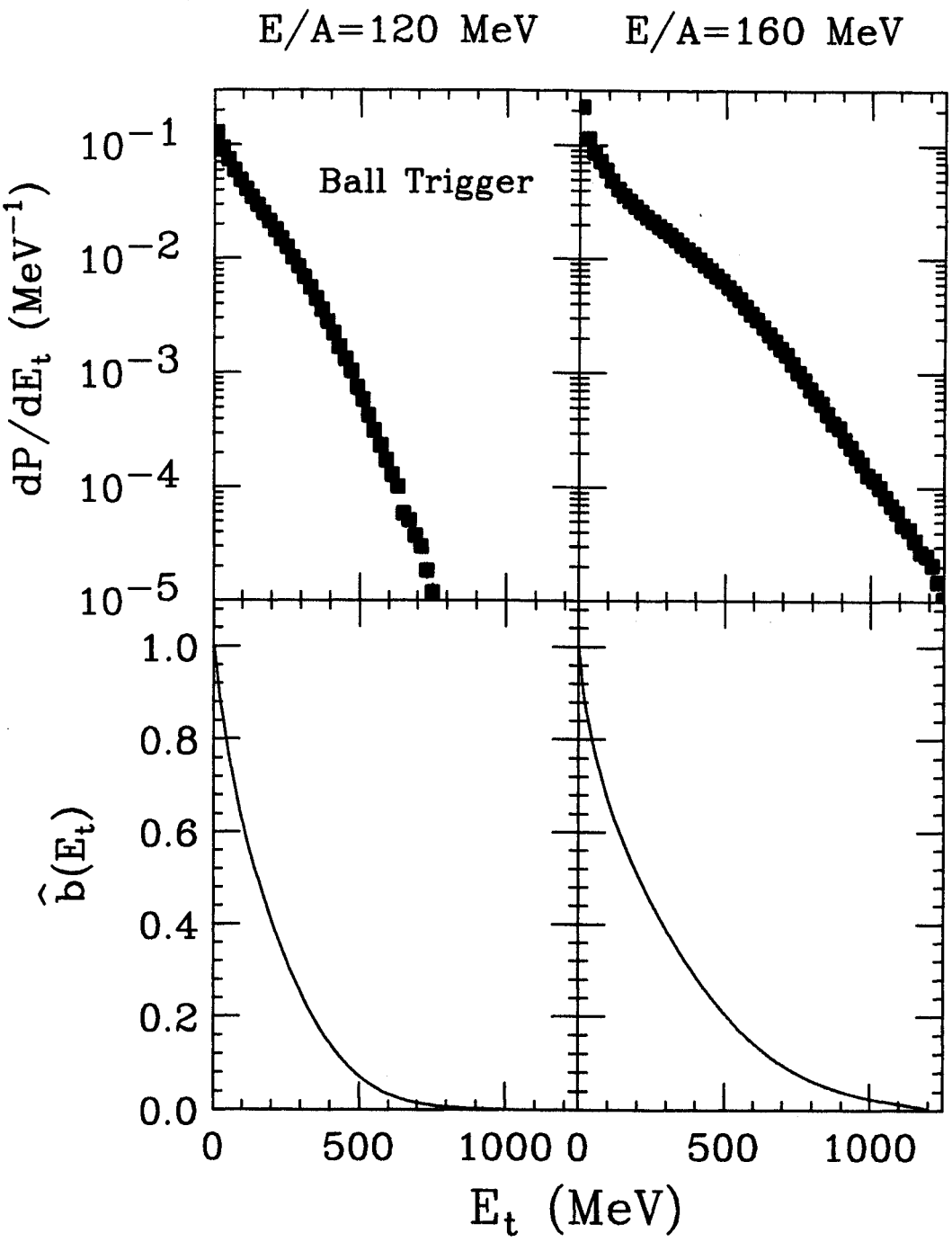

Figure 2.14. Upper panels: total transverse kinetic energy spectrum for the "Ball" trigger in our E/A=120 MeV reaction (left) and the E/A=160 MeV reaction (right). Below each spectrum is the corresponding reduced impact parameter scales $\hat{b}(E_t)$ based on these distributions.

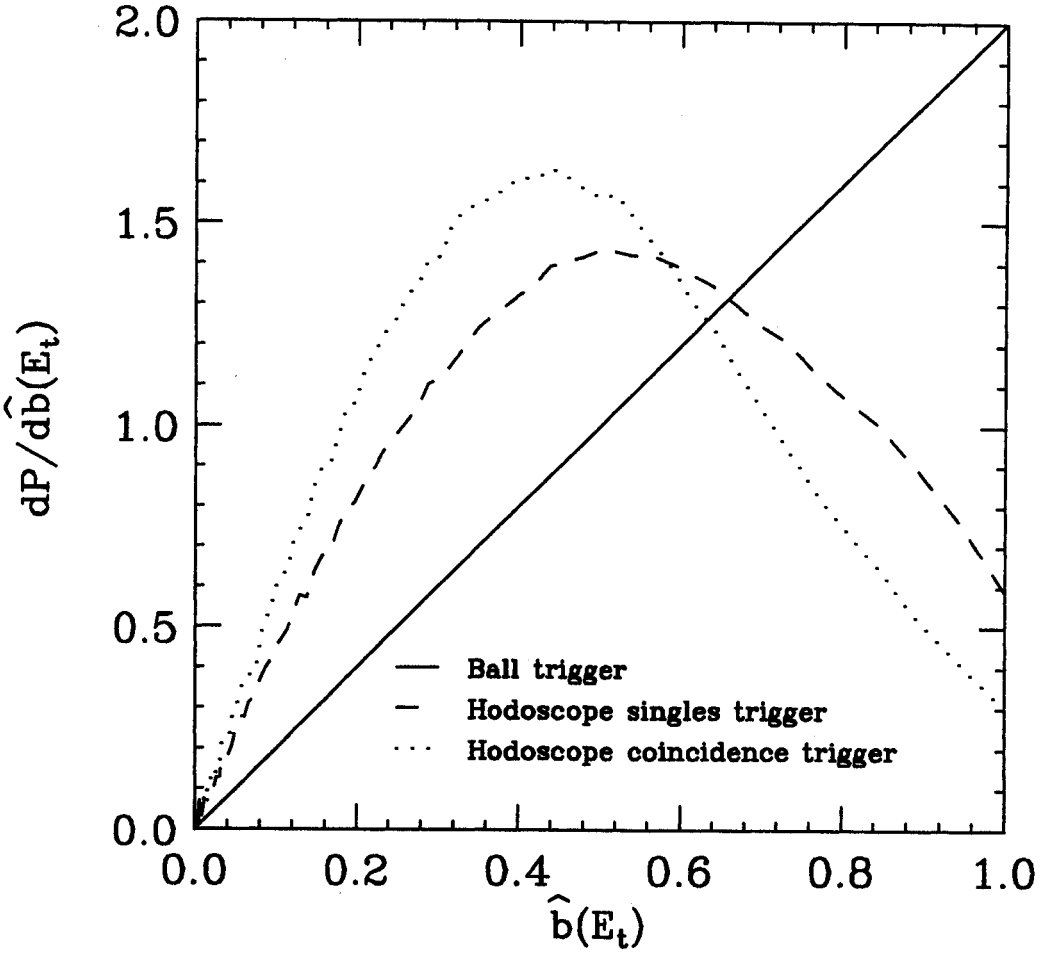

Figure 2.15. Average reduced impact parameter distributions $dP/d\hat{b}(E_t)$ for the three event triggers studied.

protons in the hodoscope clearly biases the data to slightly more central collisions.

In Figure 2.16 we compare the transverse kinetic energy spectrum to predictions of the BUU transport model using a geometric weighting of impact parameters. Since the BUU transport model only predicts the emission of nucleons, Figure 2.16 shows the predicted values of E_t when neutrons are included (dashed line) and not included (solid line) in the definition of E_t. The obvious disagreement between observed and calculated E_t spectra arises primarily from the fact that the BUU model describes the time evolution of the single–particle phase space distribution. As a consequence, the model cannot reproduce observables sensitive to the emission of complex fragments contributing to the sum in Equation 2.1. Similar difficulties are encountered for other observables, such as N_C and Z_Y. Since the calculations fail to reproduce the observed E_t spectrum, comparisons or E_t–selected data to model predictions are not straightforward. Clearly, the use of identical E_t cuts on data and theoretical predictions is inappropriate.

We attempt to construct a realistic impact parameter distribution sampled by the data. For this purpose, we employ alternative reduced impact parameter scales derived from the charged–particle multiplicity and midrapidity charge (using X= N_C and Z_Y, respectively, in Equation 2.3). By construction, a sharp cut in the observable X corresponds to a sharp cut in $\hat{b}(X)$. In order to quantify the values of impact parameter that are sampled by the data, one must consider the effects of fluctuations in the relationship between the true impact parameter of a collision and the global observable X. Following References [Phai 92, 93b, Hand 94 and Lisa 93c], we obtain an estimate of the scale of the fluctuations in the relationship between the true reduced impact parameter $\hat{b}_{true}$ and the transverse kinetic energy E_t by observing the effects of narrow cuts in $\hat{b}(N_C)$ and

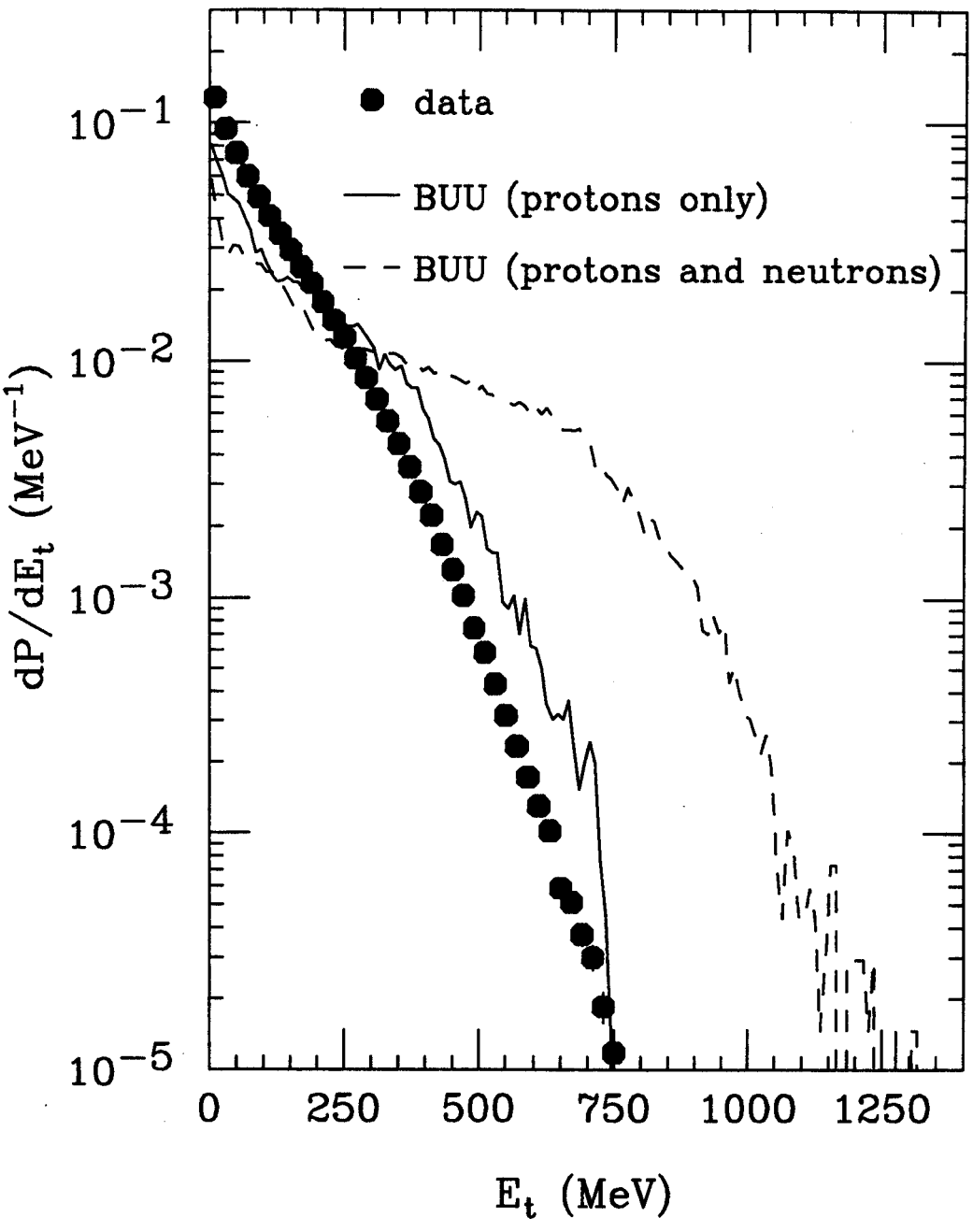

Figure 2.16. The total transverse kinetic energy spectra, dP/dE_t, measured in the 4π Array (solid) is compared with the predictions of BUU where neutrons are included (dashed line) and excluded (solid line).

$\hat{b}(Z_Y)$ on the distribution $dP/d\hat{b}(E_t)$. The upper panel of Figure 2.17 shows $dP/d\hat{b}(E_t)$ for narrow cuts in $\hat{b}(N_C)$ (dotted line) and in $\hat{b}(Z_Y)$ (dashed line), and for a double–cut on both variables (solid line) for our E/A=120 MeV collisions. Similar distributions are shown in the lower panel for somewhat less central cuts. The widths, $\sigma(\hat{b})$, of the double–cut distribution can be taken as upper limits of the widths of the distributions of the true reduced impact parameter for a given values of E_t.

To obtain a "true" reduced impact parameter distribution $dP/d\hat{b}_{true}$, it is necessary to fold the effects of the finite widths into the impact parameter distributions. As an ansatz, we take the following expression for the probability distribution of true reduced impact parameters for events filtered by a sharp cut on $\hat{b} \equiv \hat{b}(E_t)$:

$$\frac{dP(\hat{b};\hat{b}_{true})}{d\hat{b}_{true}} \propto \hat{b}_{true} \cdot \exp\left(-\frac{(\hat{b}-\hat{b}_{true})^2}{\sigma^2(\hat{b})}\right) \cdot \Theta(1-\hat{b}_{true}) \cdot \Theta(\hat{b}_{true}) \qquad (2.5)$$

For a given cut, $E_t^{min} \le E_t \le E_t^{max}$, the true reduced impact parameter distribution is given by:

$$\frac{dP}{d\hat{b}_{true}} = \int_{\hat{b}_{min}}^{\hat{b}_{max}} d\hat{b} \left[\frac{dP(\hat{b};\hat{b}_{true}))}{d\hat{b}_{true}} \cdot \frac{dP(\hat{b})}{d\hat{b}}\right] \qquad (2.6)$$

with $\hat{b}_{min} = \hat{b}(E_t^{max})$ and $\hat{b}_{max} = \hat{b}(E_t^{min})$. By inserting the geometric distribution $dP/d\hat{b} = 2\hat{b}/\hat{b}_{max}^2$, into Equation (2.6), we construct explicit impact parameter distributions used to weight the impact parameters of the BUU calculations. In our calculations, we assumed b_{max}=10 fm; an additional

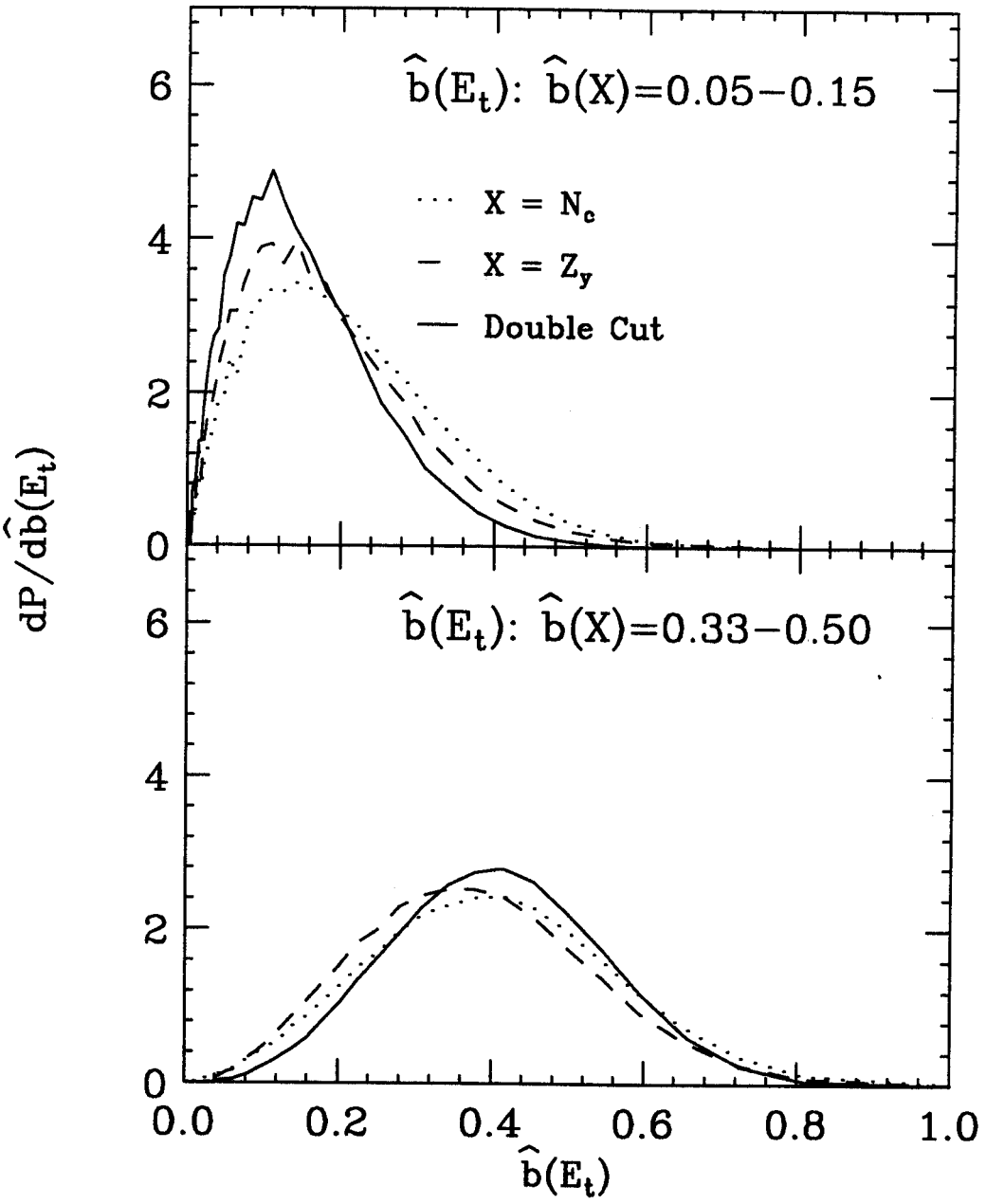

Figure 2.17. Reduced impact parameter distributions $dP/d\hat{b}(E_t)$ for the narrow cuts on $\hat{b}(N_C)$ and $\hat{b}(Z_Y)$ indicated in the figure. The upper and lower panels show for central and midcentral cuts.

requirement of proton emission in the direction of the hodoscope was imposed when selecting phase–space points for the calculation of correlation functions. For illustration, the upper panel of Figure 2.18 shows the sharp cut in $\hat{b}(E_t)$ used in the subsequent analysis of our *data*. The lower panel shows the corresponding distributions, extracted via Equation 2.6 for our *theoretical* E/A=120 MeV analysis (solid) and our *theoretical* E/A=160 MeV analysis (dashed).

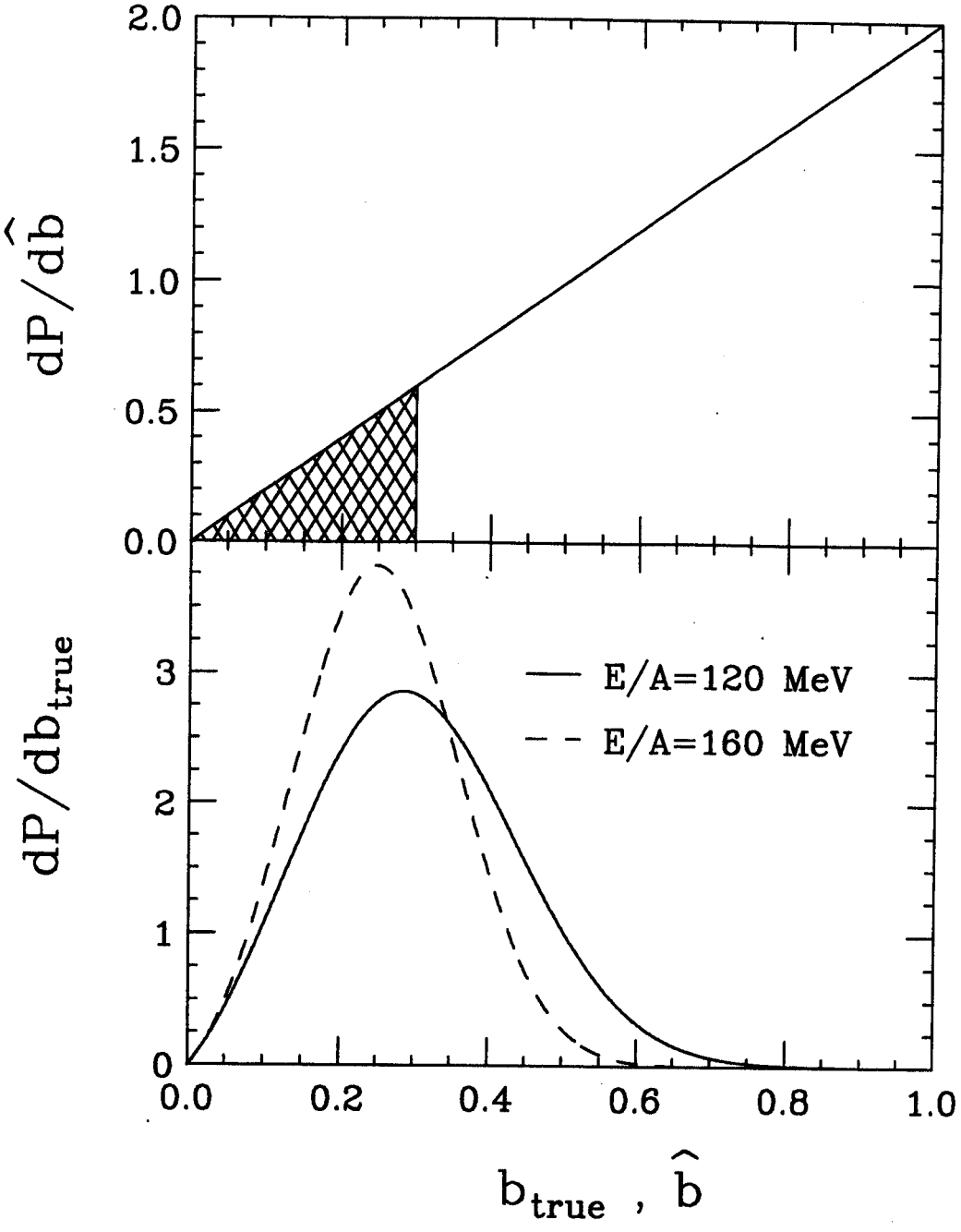

Figure 2.18. Upper panel: sharp cut in $\hat{b}(E_t)$ used to define our central events. Lower panel: distributions $dP/d\hat{b}_{true}$ of "true" reduced impact parameter corresponding to the cut on $\hat{b}(E_t)$ (in upper panel) for our E/A=120 MeV results (dashed line) and our E/A=160 MeV results (solid line).

Chapter 3 – The Two–Proton Correlation Function

In this chapter we give a brief review of the formalism in which the two–proton correlation function is calculated from the predicted single particle phase space density. The sensitivity of the correlation function to the source size and lifetime is discussed with the use of analytical source parametrizations. Finally, we discuss the construction of the experimental correlation function from measured data and the effects of target thickness.

3.1 The Koonin–Pratt Formalism

The theoretical framework known as the Koonin–Pratt formalism uses the *single* particle emission probability and knowledge of the two–particle relative wave function to calculate the correlation function. Since the derivation of the general particle–particle correlation function is produced in detail elsewhere [Koon 77, Prat 84, Prat 87, Boal 90, Gong 91a], we discuss only those results which are pertinent to two–proton correlations.

The formalism requires knowledge of the probability of emitting a proton at position $\vec{r}$ with momentum $\vec{p}$ at time t. This information is contained in the "source function" $g(\vec{r},\vec{p},t)$, which can be predicted by theoretical models such as the Boltzmann–Uehling–Uhlenbeck (BUU) dynamic transport model [Gong 90c, 91b, Baue 92a]. For demonstrative studies, schematic Monte–Carlo simulations can produce analytical source functions; for example, Gaussian spatial distributions with exponential lifetimes. In most of our analysis, the BUU model is used to predict the theoretical source function $g(\vec{r},\vec{p},t)$. In Chapter 5, however, we use schematic simulations to study whether of the correlation functions can be used to identify exotically shaped sources such as tori and discs.

Once the source function is known, three assumptions are made in order to calculate the correlation function. It is assumed that the protons are emitted

independently of one another, implying that all correlation between the two protons are due to the final state interactions discussed in chapter 1: the nuclear and Coulomb forces and the effects of the Pauli principle. However, conservation laws restrict the independence of the particles [Lync 82]. Entrance channel effects [Zhu 91] and correlations in the source itself [Bern 85, Alm 93, Kund 93] can also break this assumption.

It is also assumed that the two protons interact only with each other and not with the emitting source nor with other emitted particles. For light particles well above the Coulomb barrier this is a reasonable assumption because the Coulomb field will not affect the relative coordinates of the emitted particles. For heavier fragments, however, effects of the nuclear residue become important [Kim 91, Kim 92, Fox 93, Bowm 93, Glas 93]. Even for light particles, especially near the Coulomb barrier [Eraz 91, Gong 92], three–body calculations have shown a sensitivity to the charge of the emitting source [Ledn 95, Mart 95].

The third and final assumption is that the source function $g(\vec{r},\vec{p},t)$ is approximately constant over regions of momentum of order q, the two–proton relative momentum. This is reasonable since the momenta of the protons are typically hundreds of MeV/c, while the correlation function's region of interest lies in the range q=0~50 MeV/c.

With these assumptions, References [Koon 77, Prat 84, 87, Boal 90, and Gong 91a] have shown that the correlation function can be written:

$$1+R(\vec{P},\vec{q}) = C(\vec{P},\vec{q}) = \frac{Y_2(\vec{p}_1,\vec{p}_2)}{Y_1(\vec{p}_1)\cdot Y_1(\vec{p}_2)} =$$

$$\frac{\int d^4r_1 d^4r_2\; g(\vec{r}_1,\vec{P}/2,t_1)\cdot g(\vec{r}_2,\vec{P}/2,t_2)\cdot\left|\varphi\left(\vec{r}_1-\vec{r}_2-\frac{t_1-t_2}{2m}\cdot\vec{P},\,\vec{q}\right)\right|^2}{\int d^4r_1\; g(\vec{r}_1,\vec{P}/2,t_1)\;\bullet\;\int d^4r_2\; g(\vec{r}_2,\vec{P}/2,t_2)}, \qquad (3.1)$$

where $\vec{q}=\frac{1}{2}(\vec{p}_1-\vec{p}_2)$ is the relative momentum in the rest frame of the proton pair, $\vec{P}$ is the total momentum of the proton pair, and the relative wave function,

$\varphi(\vec{r},\vec{q})$, depends only on the relative phase space coordinates at the time of emission of the second proton.

The relative wave function was calculated by modifying the full Coulomb wave function [Mess 76] by the contribution from the nuclear interaction between the protons. This contribution was calculated by solving the Schrödinger equation for the $\ell = 0$ and $\ell = 1$ partial waves with the Coulomb and Reid soft–core potential [Reid 68]. The two–proton wave function was then calculated as:

$$\left|\varphi(\vec{r},\vec{q})\right|^2 = \tfrac{1}{4}\left|\varphi_s(\vec{r},\vec{q})\right|^2 + \tfrac{3}{4}\left|\varphi_t(\vec{r},\vec{q})\right|^2, \qquad (3.2)$$

where $\varphi_s(\vec{r},\vec{q})$ and $\varphi_t(\vec{r},\vec{q})$ are the singlet at triplet two–proton spatial wave functions respectively, whose weights in Equation 3.2 are determined by assuming that the proton spins are statistically distributed.

For noninteracting identical particles, the squared relative wave function has the form: $\left|\varphi(\vec{r},\vec{q})\right|^2 \sim \left|e^{i\vec{r}\cdot\vec{q}} \pm e^{-i\vec{r}\cdot\vec{q}}\right|^2 \sim 1 \pm \cos(2\vec{r}\cdot\vec{q})$, where the upper (lower) sign applies to bosons (fermions), due to the quantum mechanical (anti) symmertrization requirement. The correlation function is then the Fourier transform of the square of the source distribution [Kopy 72, Zajc 92]. For spin–1/2 fermions, then, the correlation function reduces to 1/2 at q=0 , and returns to 1 with a characteristic width of $q_x \approx 1/r_x$, for a source whose spatial extent in the x–direction is about r_x [Kopy 72]. A full measurement of the 3–dimensional characteristics of the correlation function would, in principle, yield the size and shape of the emitting source.

The Coulomb interaction between the protons produces a dip in the correlation function that goes to zero as q goes to zero. As long as the spatial extent of the source is well below the proton Bohr radius of 58 fm, this dip is largely independent of the relative orientation of $\vec{r}$ and $\vec{q}$. An unfortunate aspect of the Coulomb interaction is that it lessens the number of available pairs

at small relative momentum, making it more difficult to determine the effects of identical particle interference.

The strong interaction provides a very sensitive gauge of the size of the source. An attractive ^{2}He "near–resonance" (with a phase shift of about 60°) causes a bump in the correlation function at q ≈ 20 MeV/c. The size of the bump scales roughly as the proportion of proton pairs whose relative position is within the size of the nearly bound state. The height to the bump, therefore, scales approximately as R^{-3}. However, since this "resonance" is S–wave, it provides no directional information.

3.2 Resolving the Space–Time Ambiguity of the Correlation Function

Illustrative calculations of the two–proton correlation function have been performed in detail in references [Gong 91c] and [Lisa 93c] for various source parametrizations. Without reproducing those illustrations, we discuss some of their relevant points.

Calculations of the correlation function with schematic sources of zero lifetime are able to easily differentiate source sizes which differ by as little as 1/2 fm, provided the source radius is less than about 7 fm. For larger sources, the sensitivity is diminished, but not removed. Calculations with schematic sources of fixed size emitting protons of fixed momentum revealed sensitivity to the lifetime of the source on order about 10 fm/c, provided the lifetime was less than about 100 fm/c. Similarly, the sensitivity was diminished, but not removed, for longer lived sources. Calculations with fixed lifetime and fixed source size showed that correlation function with cuts on the total momentum of the proton pair were distinguishable provided that the momentum cuts differ by about 200 MeV/c. It was shown that faster moving protons exhibited a smaller peak at q=20 MeV/c than slower protons. This can be understood in terms of the 'apparent' source size. For a faster pair, the spatial separation at the time of the second proton's emission will be greater than for a slower pair, due to

kinematics. This faster pair, therefore, appearing to come from a larger source, has a reduced peak in the correlation function.

Although the schematic calculations described above show sensitivity to the radius (when lifetime is held fixed) and to the lifetime (when radius is held fixed), they cannot differentiate a small source of large lifetime from a larger source of shorter lifetime. To extract such information, it is necessary to exploit the directional sensitivity of the quantum mechanical contributions to the correlation function. This is accomplished, as described in chapter 1, by gating on the angle between relative and total proton momentum, $\psi = \cos^{-1}\left(\left|\vec{P}\cdot\vec{q}\right|/Pq\right)$. Care must be taken when defining this angle because although the relative momentum is independent of reference frame (in the non–relativistic limit), the total momentum depends upon the frame of reference. Since the phase–space distribution of emitted protons is extended in the direction of $\vec{P}$ (defined *in the rest frame of the emitting source*), the angle ψ should be constructed in the source rest–frame [Gouj 91, Lisa 93b, Rebr 93]. In chapter 4, we discuss the effects of defining the angle ψ in frames of reference moving with velocities ranging from 0 (laboratory frame velocity) to v_{proj} (projectile frame velocity) for both central and peripheral collisions.

3.3 Calculating Correlation Functions from Model Predictions

The model (BUU, QMD, schematic calculation, etc.), is used to generate the source function, $g(\vec{r},\vec{p},t)$, from which the correlation function is then calculated employing the Koonin–Pratt formalism described earlier. In practice, the model produces a set of phase space points for different impact parameters and reaction–plane orientations. In order to simulate a geometrical distribution of impact parameters, N_b, the number of ensembles (or simulated events) with a given impact parameter b, was set proportional to b. With n, the event number,

running from 1 to N_b and i, the particle number, running from 1 to $M_{n,b}$ (the multiplicity of the event), the correlation function was calculated as [Lisa 93c]:

$$1+R(q)=$$

$$C\frac{\sum_b \frac{1}{N_b}\sum_{n_1}^{N_b}\sum_{n_2}^{N_b}\sum_{i}^{M_{n_1 b}}\sum_{j}^{M_{n_2 b}}\left(1-\delta_{ij}\delta_{n_1 n_2}\right)\delta_\Delta\left(q-\frac{\left|p'^{n1}_{ib}-p'^{n2}_{jb}\right|}{2}\right)\left|\varphi(x''^{n1}_{ib}-x''^{n2}_{jb};\frac{\left|p'^{n1}_{ib}-p'^{n2}_{jb}\right|}{2})\right|^2}{\sum_{b_1}\sum_{b_2}\sum_{n_1}^{N_{b1}}\sum_{n_2}^{N_{b2}}\sum_{i}^{M_{n_1 b_1}}\sum_{j}^{M_{n_1 b_2}}\left(1-\delta_{ij}\delta_{n_1 n_2}\delta_{b_1}\delta_{b_2}\right)\delta_\Delta\left(q-\frac{\left|p'^{n1}_{ib}-p'^{n2}_{jb}\right|}{2}\right)}. \tag{3.3}$$

Here, the primed momenta are calculated in the center–of–momentum frame of the proton pair and the double–primed coordinates are calculated in the center–of–momentum frame at the time of emission of the second proton; φ is the wave function of relative motion between the two protons; $\delta_\Delta(q)$ is the "binning function" which is unity for $|q| \le \frac{1}{2}\Delta$ and zero otherwise; and C is a constant which sets R(q)=0 for q between 60 MeV/c and 80 MeV/c. Construction of the correlation function gated on centrality involves setting N_b proportional to the appropriate distribution $dP/d\hat{b}_{true}$ shown in the bottom panel of Figure 2.18.

3.4 Constructing Experimental Correlation Functions

Experimentally, the two–proton correlation function, 1+R(q), is defined through the relationship:

$$\sum Y_2(\vec{p}_1,\vec{p}_2) = N(1+R(q))\sum Y_{back}(\vec{p}_1,\vec{p}_2), \tag{3.4}$$

where $Y_2(\vec{p}_1,\vec{p}_2)$ is the measured coincidence yield for two protons with momenta $\vec{p}_2$ and $\vec{p}_2$, $Y_{back}(\vec{p}_1,\vec{p}_2)$ is the background yield, and N is a normalization constant. The sums on both sides of Equation 3.4 are extended

over all combinations of detectors and proton energies corresponding to each q–bin.

The background yield, $Y_{back}(\vec{p}_1,\vec{p}_2)$, is typically constructed in one of two ways. The first method, known as the "singles" technique, defines the background yield as the product of the single particle yields, measured with the same trigger condition as the coincidence yield: $Y_{back}(\vec{p}_1,\vec{p}_2)=Y_1(\vec{p}_1)\cdot Y_1(\vec{p}_2)$ [Zarb 81, Chit 85, 86a, Poch 86, Kyan 86, Chen 87a, 87b, Poch 87, Awes 88, Gong 90b, 90c, 91b, Kim 91, Zhu 91, Gouj 91, Lisa 93a, 93c, 93d].

The second method, referred to as the "mixed–events" technique, generates the background yield by "mixing" particles from different coincidence events [Kopy 74, Zajc 84, Gust 84, Dupi 88, Fox 88, DeYou 89, 90, Cebr 89, Rebr 90, 92, Lisa 91, 93c]:

$$Y_{back}(\vec{p}_1,\vec{p}_2)=\sum_{i\neq j}\left\{\delta^3(\vec{p}_1-\vec{p}_{1,i})\cdot\delta^3(\vec{p}_2-\vec{p}_{2,j})+\delta^3(\vec{p}_2-\vec{p}_{1,i})\cdot\delta^3(\vec{p}_1-\vec{p}_{2,j})\right\}. \tag{3.5}$$

Here, the indices i and j label the ith and jth recorded two–particle coincidence events and $\vec{p}_{1,i}$ and $\vec{p}_{2,j}$ denote the momenta of particles 1 and 2 recorded in events i and j, respectively [Lisa 91,93c]. In our analysis, the index i ran over all recorded coincidence events while the index j took on values from i to i+10.

The mixed–events and singles techniques have been shown to produce similar correlation functions, with a slight suppression of the correlation function when constructed with the mixed–events technique [Lisa 91, 93c]. We present a comparison of correlation functions constructed with the mixed–events and with the singles techniques in Figure 3.1, which shows that the differences are small (about 3%), consistent with previous comparisons.

A mixed events analysis offers the advantage of simplicity since no singles measurements are required to construct the correlation function. However, the coincidence technique is known to suppress the final state

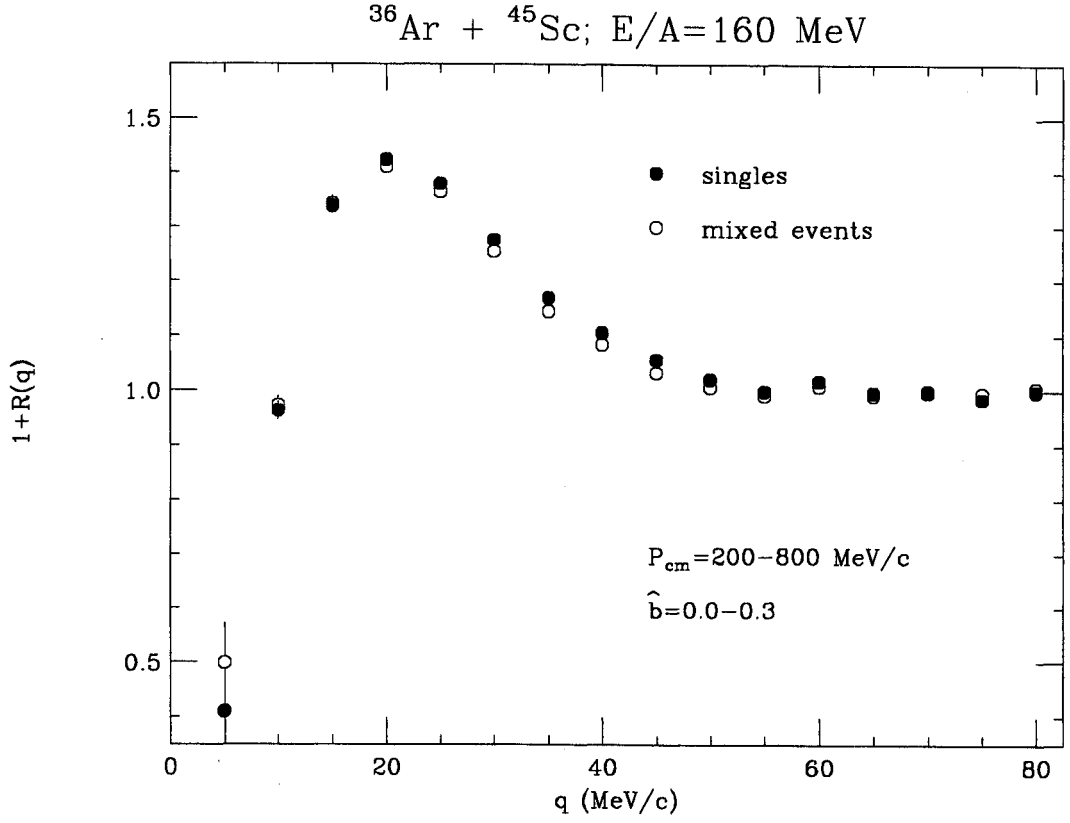

Figure 3.1. Correlation functions constructed with the mixed–events technique (open circles), and with the singles technique (solid circles). The suppression of the mixed–events constructed correlation function is consistent with previous studies [Lisa 91, 93c]

correlations under study [Zajc 84]. We have adopted the singles technique in our analysis of the correlation function for four reasons:

- Consistency with previous analyses [Gong 89,90a,90b,90c,91a,91b,91c,92, Lisa 91,93a,93b,93c, Kund 93].
- Ease of interpreting theoretical predictions (the mixed events technique is more difficult to model theoretically).
- The singles and coincidence yields sample very similar ranges of impact parameter (see Figure 2.15); hence the use of the singles yield to construct the denominator should not distort the correlation function [Lisa 91,93c].
- Unlike the coincidence method, the singles technique does not suppress the correlations we attempt to measure (see Figure 3.1).

The correlation function's sensitivity to small distortions in the coincidence yield against the large background requires it to be rather insensitive to single–particle phase space effects and to detector resolution. Reference [Lisa 93c] shows that the resolution effects for our 56–element hodoscope are of minor consequence to the correlation function, for cuts on both total proton momentum, $\vec{P}$, and on the angle, ψ, between relative and total momenta.

In the two experiments of this thesis, (^{36}Ar+^{45}Sc at E/A=120 and 160 MeV; see Table 2.1), thick targets of area density 40 mg/cm^2 were used to compensate the lower beam intensities in order to collect reliable statistics. Uncertainties in the outgoing proton energies (due to uncertainties in the "location" of the reaction within the thick target) may lead to distortions of the correlation function.

Furthermore, theoretical comparisons are complicated by the use of the software filter intended to mimic the acceptance of the 56–element hodoscope. Because the use of a "fine" filter (one which accepts particles into the exact polar coordinates (θ,ϕ) of each detector) would require prohibitively long calculations, we have used a coarse filter which introduces a small distortion but allows

calculations to proceed approximately 10 times faster. The coarse filter first accepts single protons that lie within the polar (θ) coordinate range of the hodoscope (θ=30°–45°). After randomly picking pairs of protons (appropriately weighted for relative angular acceptance), it screens these pairs to guarantee that the individual protons are not closer than 2.6 degrees of one another (the minimum spacing between detector elements).

The effects of both the target energy loss and the use of the coarse filter are small. Figure 3.2 shows theoretical correlation functions constructed with the coarse filter (and no target loss correction) in the solid line and with the fine filter (taking into account target energy loss) in the dashed line. The source function for this comparison took on the form $g(r,p,t) \sim e^{(-r/r_o)^2} e^{(-p^2/2mT)}\delta(t)$, with r_o=3.0 fm and T=20 MeV. The differences between the effects of the two filters are smaller than the differences between using mixed–events and singles techniques, and are within the uncertainty of our measurements, justifying the use of the faster course filter in our calculations of theoretical correlation functions.

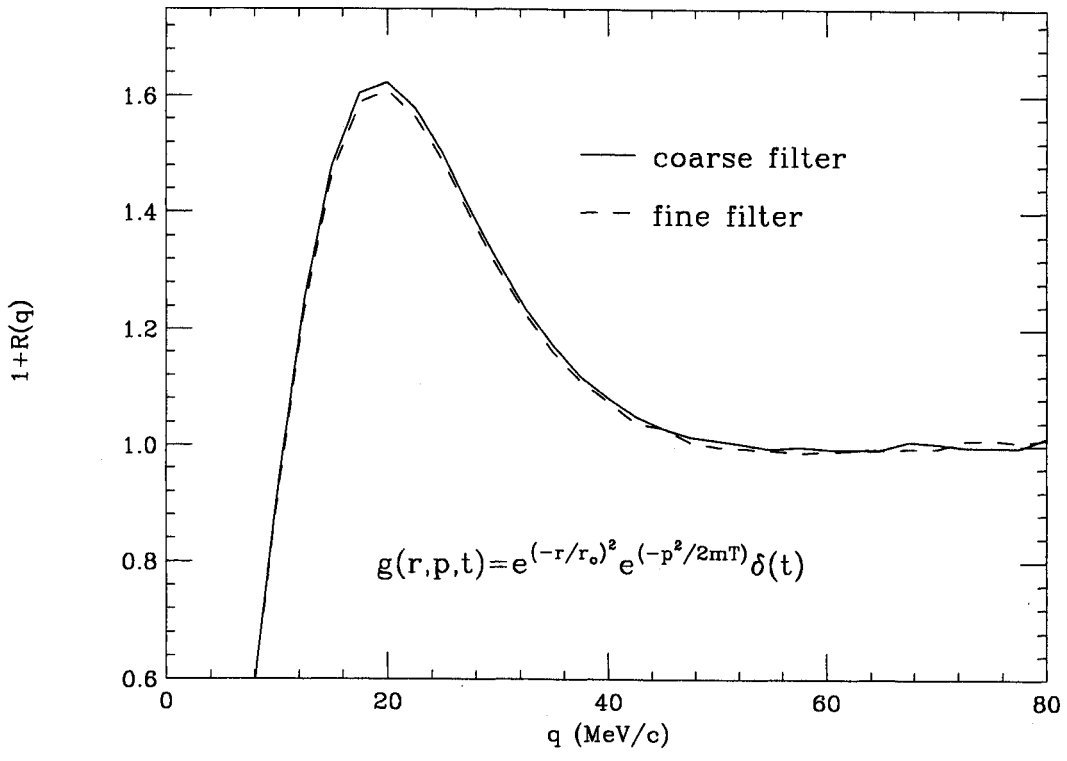

Figure 3.2. A theoretical correlation function constructed from the schematic source function $g(r,p,t) \sim e^{(-r/r_o)^2} e^{(-p^2/2mT)} \delta(t)$ using the coarse filter, which does not take into account energy loss through the target, is shown in the solid line. The correlation function calculated by using the exact filter and correcting for energy loss through the target is shown in the dashed line. The differences are smaller than the uncertainty in our measurements.

Chapter 4 – Correlation Functions for $^{36}Ar + ^{45}Sc$ at E/A=80 MeV

This chapter presents a comparison of BUU predictions with two–proton correlation function measured for impact–paramter gated collisions of $^{36}Ar + ^{45}Sc$ at E/A=80 MeV. We compare both angle integrated and directional correlation functions for central and peripheral collisions and for high and low momentum proton pairs. Since directional correlation functions depend upon the frame of reference, comparisons are made in the laboratory, center–of–mass and projectile rest frames. Finally, we present a detailed analysis of the BUU predictions of directional correlation functions for different impact parameters, proton momenta and frames of reference. The experimental results presented in this chapter were taken from Reference [Lisa 93a, 93b, and 93c].

4.1 Comparison of Angle–Integrated Correlation Functions.

The main findings of Reference [Lisa 93a] are shown in Figure 4.1. The solid points in the figure show the measured [Lisa 93a] total momentum dependence of the average peak height, $\langle 1+R\rangle_{q=15-25\,MeV/c}$, of the two–proton correlation function in the region around q≈20 MeV/c. As described in chapters 1 and 3, for relatively small sources and short emission time scales, this quantity is the primary indicator of the extent of the phase–space distribution of emitted protons. The data are gated on central and peripheral collisions in the upper and lower panels, defined by $\hat{b}(E_t) \leq 0.36$ and $\hat{b}(E_t) = 0.44 - 0.82$, respectively (see chapter 2 and References [Lisa 93c, Hand 94]). Error bars indicate statistical uncertainties as well as an estimate of the normalization uncertainty in the high–q region. For orientation, the right hand axis gives the Gaussian radius of a zero–lifetime spherical source that produces a correlation function with the same value of $\langle 1+R\rangle_{q=15-25\,MeV/c}$. Impact parameter filtered BUU predictions are shown as open circles. The impact parameter probability distribution,

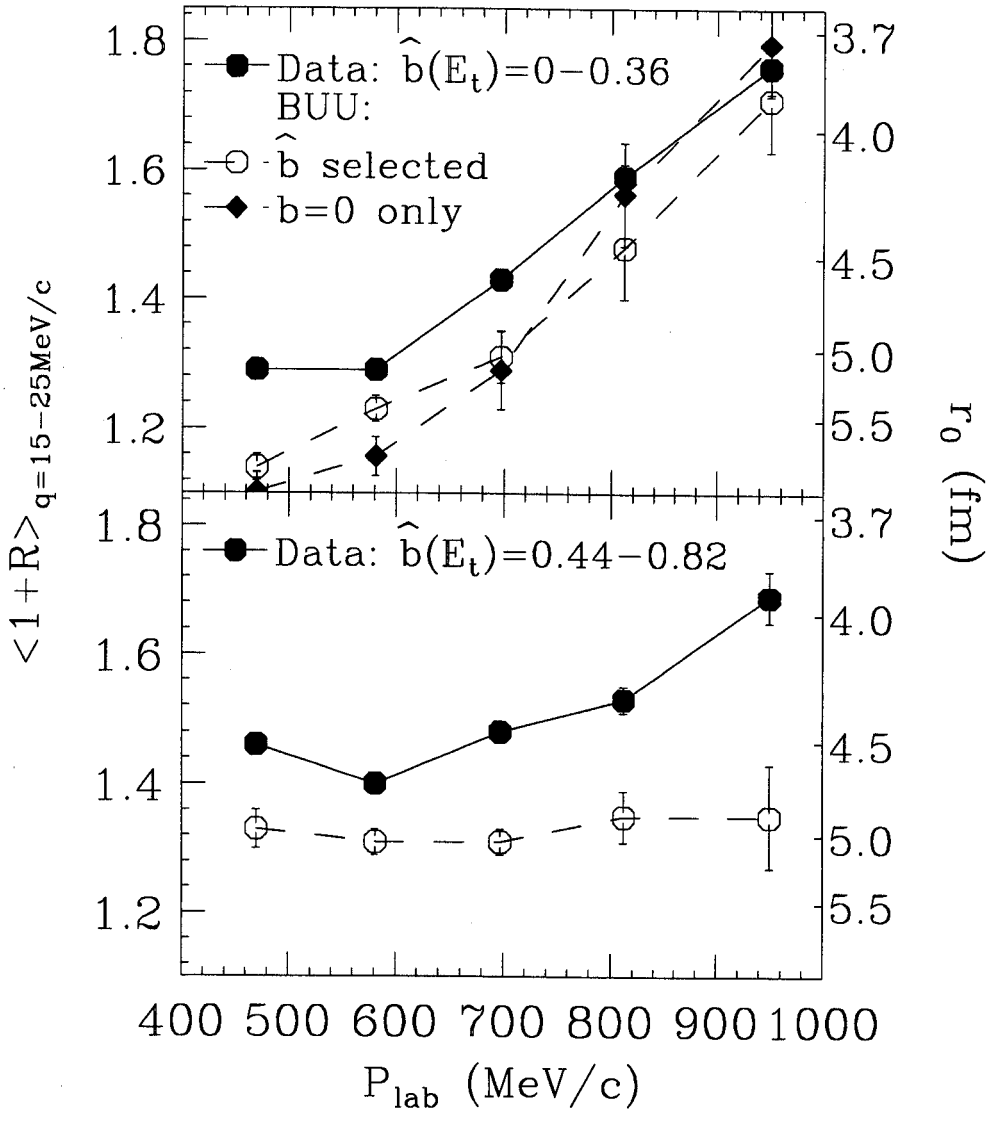

Figure 4.1 Average height of the correlation function in the region as a function of the total laboratory proton–pair momentum, P_{lab}. The right–hand axis gives the radius of a zero–lifetime spherical source with a Gaussian density profile that produces a correlation function of equal magnitude. The upper and lower panels show results for central and peripheral events. Data are shown by solid circles and impact parameter filtered BUU predictions are shown in open circles. The BUU predictions of strictly central collisions ($\hat{b}=0$) are shown in solid diamonds. The lines are drawn to guide the eye.

$dP/d\hat{b}_{true}$, used to weight these calculations was calculated in the same manner as descried in section 2.4 (using equation 2.6) and is shown in Figure 4.2. For central collisions (top panel in Figure 4.1), the agreement between experimental and theoretical correlation functions is satisfactory, but for more peripheral collisions (bottom panel), the BUU transport model substantially under predicts the total momentum dependence of the correlation function.

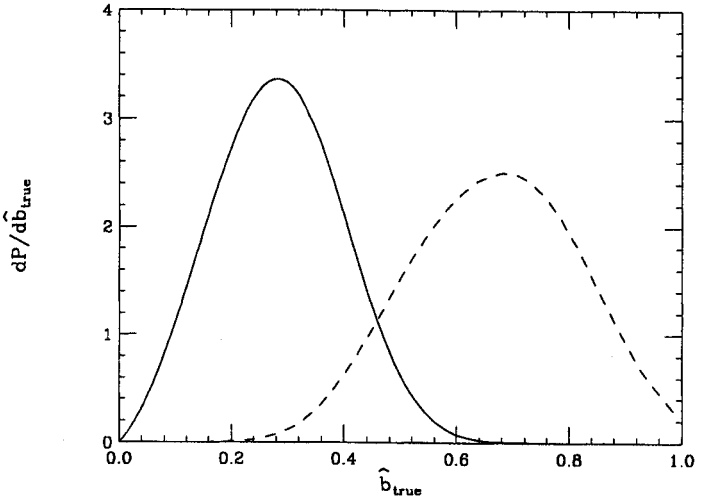

Figure 4.2. Distributions of the true reduced impact parameter, $dP/d\hat{b}_{true}$, used for the theoretical calculations of our E/A=80 MeV collisions. The solid line represents the probability distribution for central collisions, the dashed line for peripheral collisions.

The dynamics of strictly central ($\hat{b}=0$) collisions cannot be investigated experimentally because contributions from nonzero impact parameters cannot be avoided. Nevertheless, it is interesting to investigate theoretical predictions for

this idealized case and to assess the significance of imperfect impact parameter selection. For this purpose, we also present BUU predictions for collisions with $\hat{b} = 0$ (shown by solid diamonds in the upper panel of Figure 4.1). As may be expected (from the differences between central and peripheral predictions), the removal of noncentral collisions from the calculations leads to an enhanced momentum dependence of the two–proton correlation function. While the agreement with data is somewhat worse than for the more realistically filtered calculations, the qualitative observation of a strong momentum dependence of two–proton correlation functions for central collisions is already well reproduced in these simplified $\hat{b} = 0$ calculations.

The success of the BUU model in predicting the strong momentum dependence of the two–proton correlation functions observed in central collisions (top panel of Figure 4.1) suggests that the BUU transport model provides a reasonable description of the phase space density distribution of nucleons emitted in collisions at small impact parameters. Predictions for more peripheral collisions may be less reliable [Klak 93], because of a deficiency in treating the nuclear surface.

In the following, we investigate data and theoretical predictions for central collisions in more depth by exploring two–proton correlation functions with cuts on the angle ψ between $\vec{P}$ and $\vec{q}$.

4.2 Longitudinal and Transverse Correlation Functions

"Angle integrated" correlation functions (those with no explicit cut on $\psi = \cos^{-1}\left(\vec{P} \cdot \vec{q}/Pq\right)$) probe the volume of the phase–space distribution of emitted particles with little sensitivity to its shape [Pratt 87, Gong 91a]. Without independent knowledge of the size of the emitting system and the emission mechanism (surface versus volume emission), "angle–integrated" correlation functions cannot discriminate between smaller sources of longer lifetime and large sources of shorter lifetime.

This space–time ambiguity may be reduced by analyzing two–proton correlation functions with cuts on ψ [Koon 77, Pratt 87, Gong 91a, Awes 88, Gouj 91, Lisa 93b, Rebr 92]. Emission from a long–lived source leads to a phase space distribution elongated in the direction of $\vec{P}$, the total momentum of the proton pair in the rest frame of the emitting source. The magnitude of this elongation is of order $P\tau/2m$ where τ is the average time interval between the emissions of the detected particles. Two–proton correlation functions exhibit a directional sensitivity primarily due to an increased Pauli suppression in the nonelongated (transverse) direction. For very extended phase–space distributions, the Coulomb interaction causes additional ψ dependencies [Gong 91a, Kim 92]. For long–lived sources, transverse correlation functions ($\vec{q}\perp\vec{P}$) are therefore suppressed at small q in comparison with longitudinal correlation functions ($\vec{q}\parallel\vec{P}$). Since the total momentum, $\vec{P}$, depends upon the rest frame of the source, but the relative momentum, $\vec{q}$, does not, the angle ψ, and hence the definition of the longitudinal and transverse cuts, depends on the rest frame of the emitting system. Care must therefore be taken to characterize the rest frame of the emitting source [Gouj 91, Rebr 92, Lisa 93b].

Longitudinal and transverse correlation functions of low–energy proton pairs (P_{lab}=400–600 MeV/c) emitted in central ^{36}Ar + ^{45}Sc collisions were published in Reference [Lisa 93b]. Significant differences were observed when the longitudinal ($\psi_{long} = 0°–50°$) and transverse ($\psi_{trans} = 80°–90°$) cuts were defined in the ^{36}Ar + ^{45}Sc center of momentum frame. These differences were largely washed out when the directional cuts were defined in the laboratory rest frame. These observations could be reproduced by adopting a simple moving–source parametrization simulating emission from a source of finite lifetime $\tau = 20 - 40\,fm/c$ and spherically symmetric Gaussian density profile $\rho(r) \propto \exp\left(-r^2/r_o^2\right)$ with $r_o = 4.5 - 4.8\,fm$, moving with the center–of–momentum frame of reference. Energy and angular distributions of the emitted protons

were selected by randomly sampling the experimental yields. As part of this thesis project, we investigate whether the observed directional dependence of the two–proton correlation function can be understood in terms of the phase–space distribution predicted by the BUU transport model, including the impact parameter and source velocity dependencies.

The solid and open points of Figure 4.3 show the longitudinal and transverse correlation functions measured for central ^{36}Ar + ^{45}Sc collisions at E/A=80 MeV, with the angle ψ defined in the center–of–momentum frame of the colliding system [Lisa 93b]. The central cuts correspond to $\hat{b}(E_t) \leq 0.36$. The top and bottom panels of the figure show the results for low–momentum (P_{lab}=400–600 MeV/c) and high–momentum (P_{lab}=700–1400 MeV/c) protons, respectively. For consistency with References [Lisa 93a, 93b, Hand 94], we define our cuts on the magnitude of the total momentum defined in the laboratory frame, but we will use *different* rest frames for the definition of the angle ψ. Significant differences between longitudinal and transverse correlation functions are observed for the emission of slow protons, P_{lab}=400–600 MeV/c, but not for the emission of the faster protons, P_{lab}=700–1400 MeV/c, likely reflecting decreasing emission time scales for emitted protons of higher energy.

For orientation, the solid and dashed curves in Figure 4.3 show longitudinal and transverse two–proton correlation functions predicted by BUU calculations for the idealized case of $\hat{b} = 0$. The calculations reproduce the magnitude and the difference between longitudinal and transverse correlation functions rather well, slightly over predicting the peak height at q≈20 MeV/c for the high–momentum protons, P_{lab}=700–1400 MeV/c. This over prediction was already visible in Figure 4.1. It is comparable in magnitude [Gong 91a] to the theoretical uncertainty due to our choice of emission criteria t_{cut}=150 fm/c and $\rho \leq \rho_o/8$. Calculations using t_{cut}=200 fm/c predict slightly reduced correlation

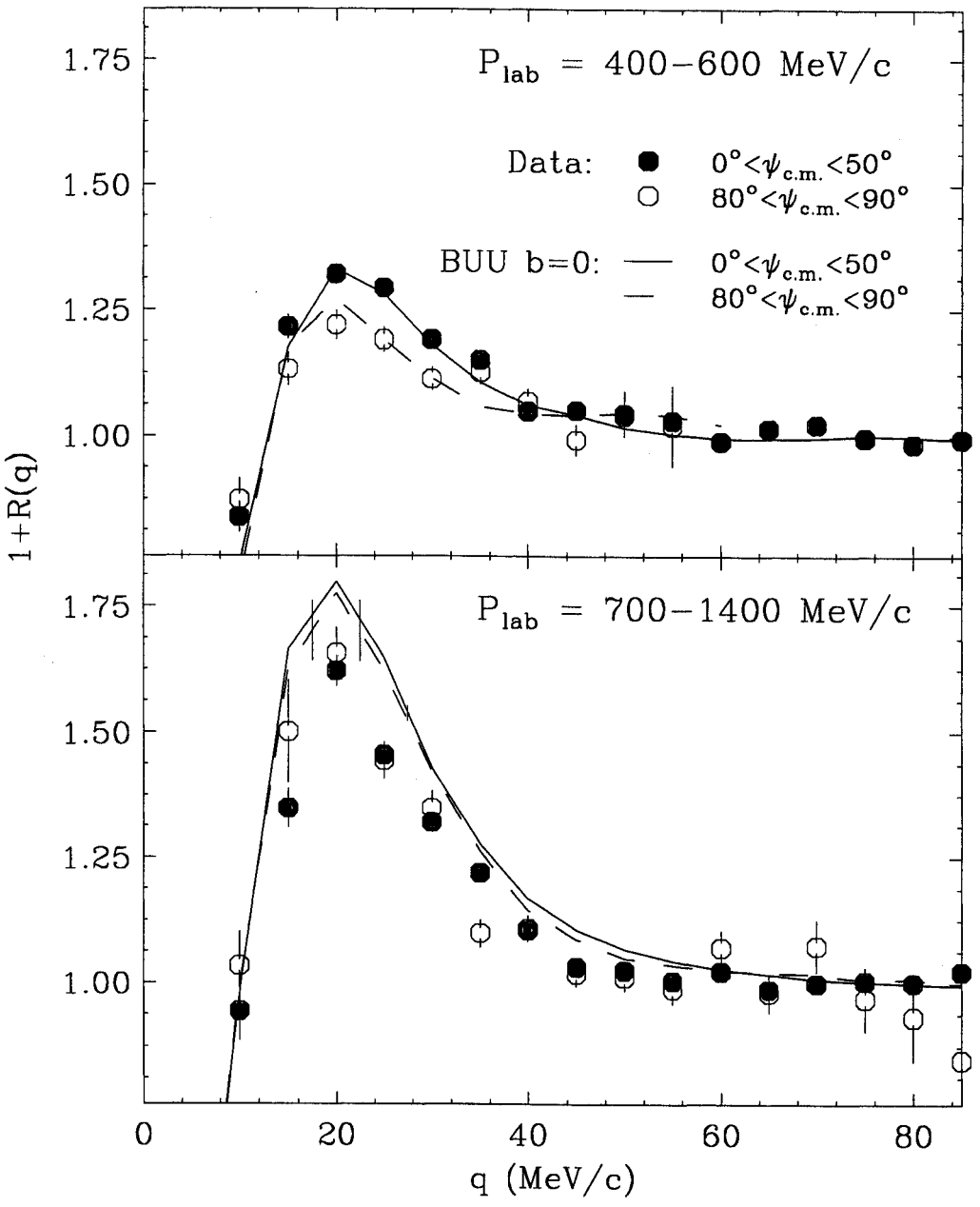

Figure 4.3. Solid and open points show longitudinal and transverse correlation functions measured for central collisions at the indicated momenta. The curves show the BUU predictions for the idealized case of purely central collisions ($\hat{b} = 0$). The cuts on the angle ψ are defined in the center–of–momentum frame of the colliding system.

functions: they agree rather well with data for the high–momentum gate, P_{lab}=700–1400 MeV/c, but they under predict the maximum at q≈20 MeV/c for the low–momentum gate and they predict too large a split between the directional correlation functions.

Figure 4.4 shows results for calculations which incorporate the effects due to the finite resolution of the centrality filter using the impact–parameter probability distribution, $dP/d\hat{b}_{true}$, shown in Figure 4.2. These more realistic calculations reproduce the overall trends of the data rather well, with a slight over prediction of the difference between longitudinal and transverse correlation functions for the high–momentum gate, P_{lab}=700–1400 MeV/c (bottom panel).

In order to provide more insight into the transport model predictions, we show in Figure 4.5 the acceptance of the hodoscope array in the p_x vs. p_z plane for single–proton momentum cuts of $p_{lab} = P_{lab}/2$. The dashed lines indicate the angular acceptance of the hodoscope: $\vartheta_{lab} = 30°–45°$. The dotted and hatched areas depict cuts corresponding to P_{lab}=400–600 MeV/c and P_{lab}=700–1400 MeV/c. For reference, the two solid circles depict the Fermi momentum spheres of the projectile (centered at $p_z/A = 395 MeV/c$) and target (centered at $p_z/A = 0$), and the dashed circle depicts the region of final momenta accessible by single nucleon–nucleon scattering processes, representative of a midrapidity source (centered at $p_z/A = 197 MeV/c$). The low–momentum cut P_{lab}=400–600 MeV/c selects protons emitted at large transverse angles with low energies with respect to the center–of–momentum rest frame for projectile and target. This kinematic region should be strongly populated by emission from the cooling participant zone formed by geometrical overlap of projectile and target, and the simple concept of emission from a source at rest in the center–of–momentum frame of the projectile–target system may be well justified for central collisions. In contrast, the high momentum cut, P_{lab}=700–1400 MeV/c, selects fast protons with velocities closer to the projectile than to the target velocity. In this

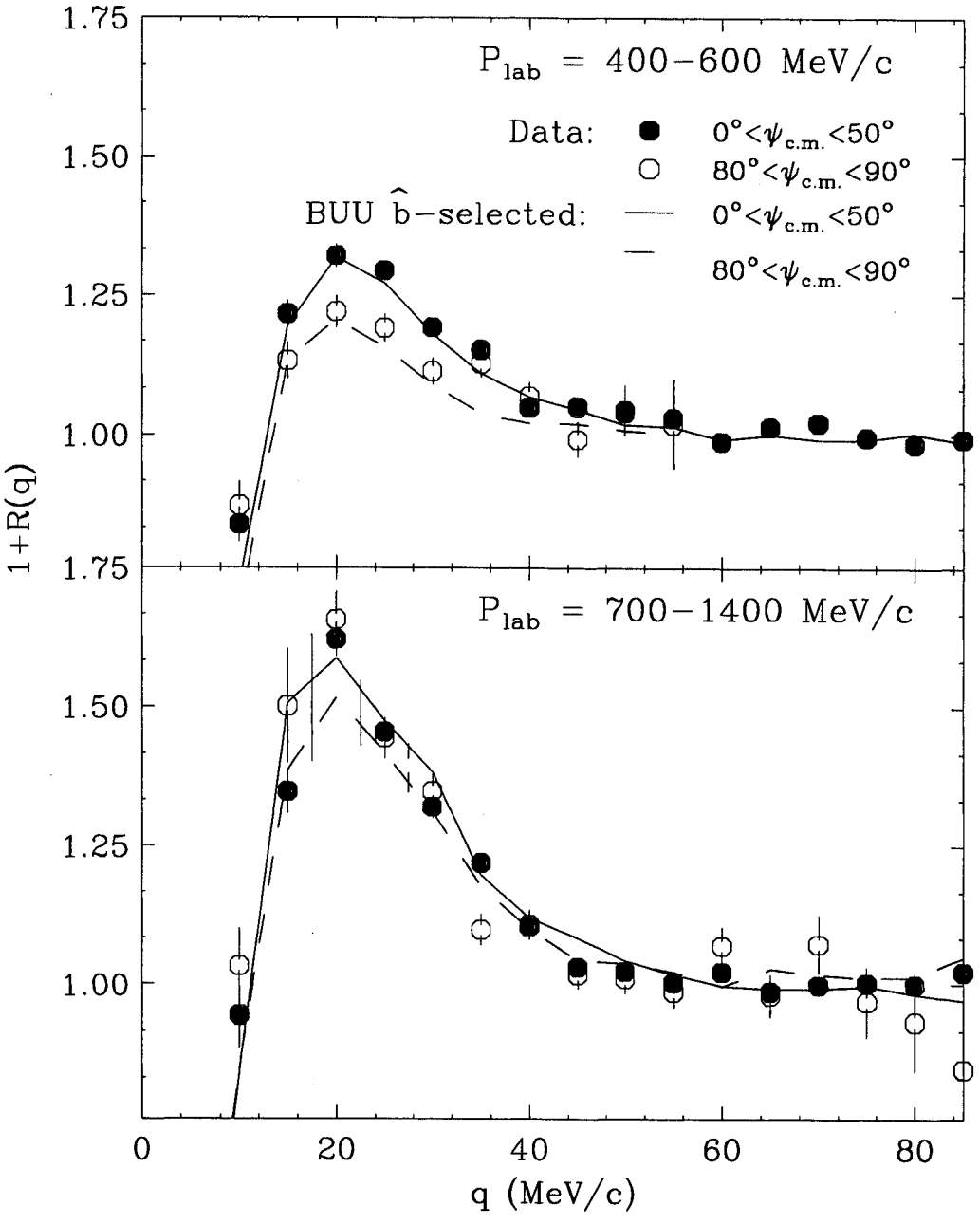

Figure 4.4. Solid and open points show longitudinal and transverse correlation functions measured for central collisions at the indicated momenta. The curves show the BUU employing the realistic impact parameter probability distribution shown in the solid line of Figure 4.2. The cuts on the angle ψ are defined in the center–of–momentum frame of the colliding system.

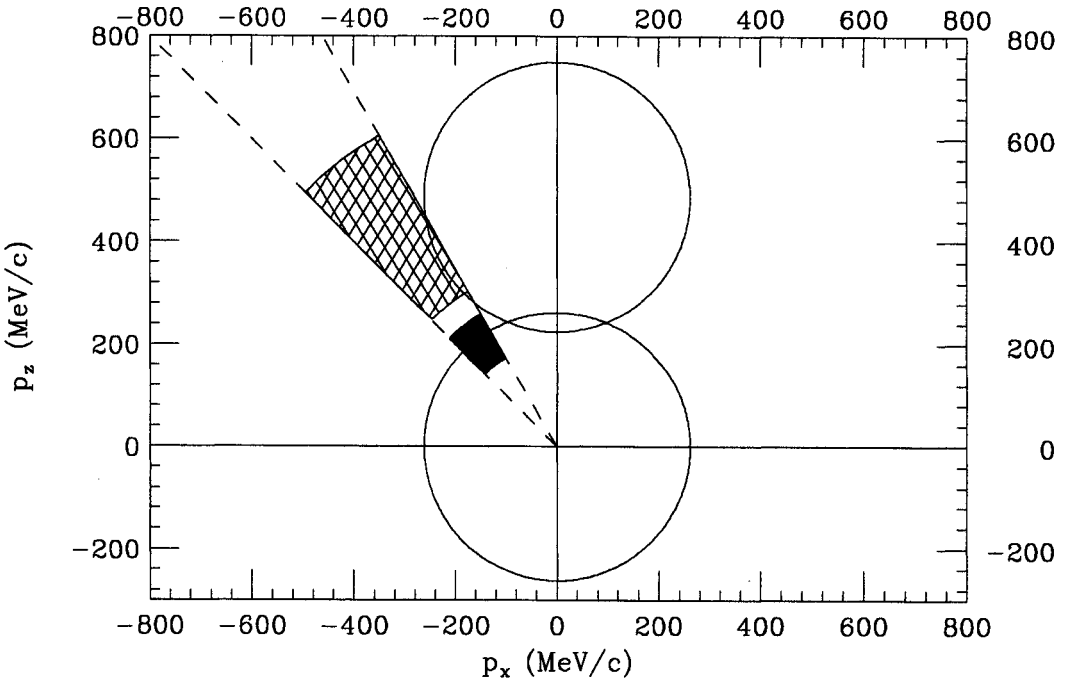

Figure 4.5. Schematic of our detector acceptance and momentum cuts. Dashed lines represent the detector boundaries at ϑ_{lab} = 30°–45°. Solid and hatched areas represent the low– and high– momentum cuts, P_{lab}=400–600 and 700–1400 MeV/c, respectively. The solid circles depict Fermi spheres of target and projectile.

kinematic domain, contaminating emission from excited projectile spectator matter is likely to occur, especially when contributions from noncentral collisions exist. Here, the concept of emission from a single source at rest in the center–of–momentum frame of projectile and target may become inappropriate.

Differences between longitudinal and transverse correlation functions caused by lifetime expansion effects are best shown by defining the angle ψ in the rest frame of the emitting system [Lisa 93b]. In less well–defined situations, other directional dependencies may exist which may not be revealed by our choice of cuts on ψ. It is therefore instructive to explore angular cuts on ψ, defined in different rest frames and compare them to predictions of the BUU model.

The upper and lower panels of Figures 4.6 and 4.7 show longitudinal (solid points) and transverse (open points) correlation functions with cuts on ψ defined in the laboratory and projectile frames, respectively. The right and left panels show data for the low and high momentum cuts. In Figure 4.6, the data are compared with BUU predictions for the idealized case of $\hat{b} = 0$. In Figure 4.7, they are compared to the more realistic impact–parameter gated calculations.

For the low–momentum cut, P_{lab}=400–600 MeV/c, the differences between longitudinal and transverse correlation functions become insignificant when the cuts on ψ are defined in the laboratory frame (top, left panels of Figures 4.6 and 4.7) and in the projectile rest frame (bottom, left panels). These trends are rather well reproduced by the BUU calculations, using either the $\hat{b} = 0$ (Figure 4.6) or realistic impact parameter weights (Figure 4.7). For the present reaction, the emission of low–energy protons at large angles ($\vartheta_{c.m.} \approx 90°$) appears to be rather well described by the BUU calculations, with little sensitivity to contributions from collisions at small, but nonzero, impact parameters.

For the high momentum cut, P_{lab}=700–1400 MeV/c, no significant difference between measured longitudinal and transverse correlation functions is observed when the cuts on ψ are defined in the laboratory frame (right, top

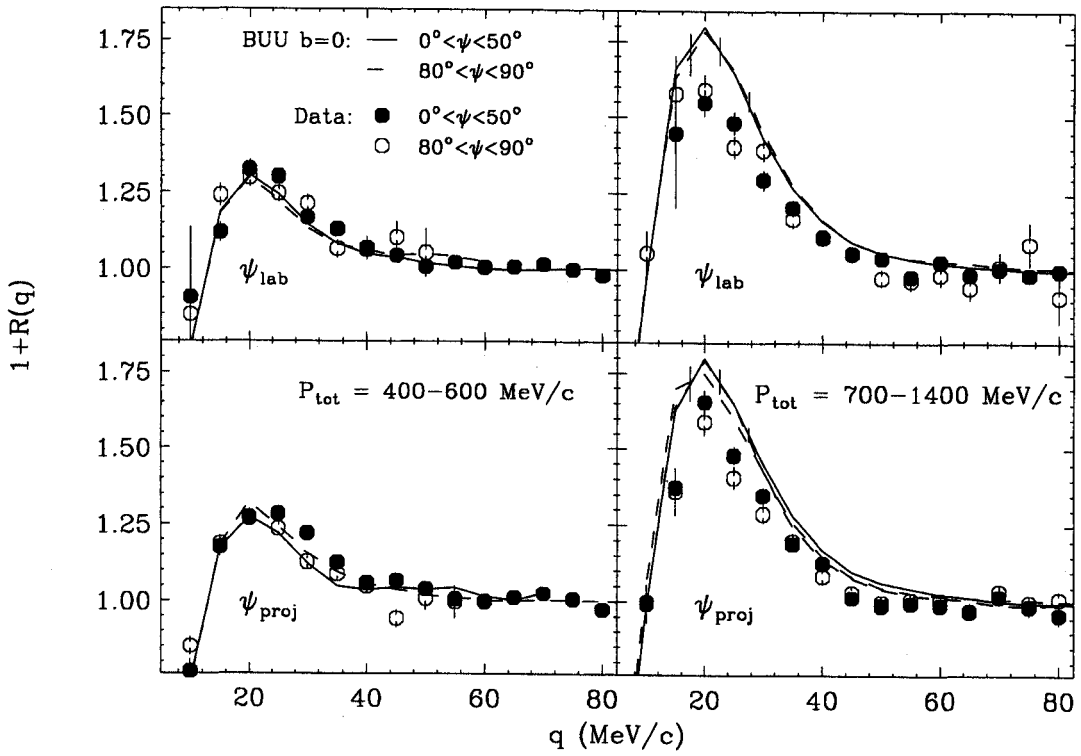

Figure 4.6. Longitudinal (solid points and curves) and transverse (open points and dashed curves) correlation functions constructed in the laboratory (top) and projectile (bottom) rest frames. Left and right panels show results for low– and high–momentum cuts, respectively. Points show data selected by the centrality cut $\hat{b}(E_t) \leq 0.36$, and the curves show BUU predictions for $\hat{b} = 0$.

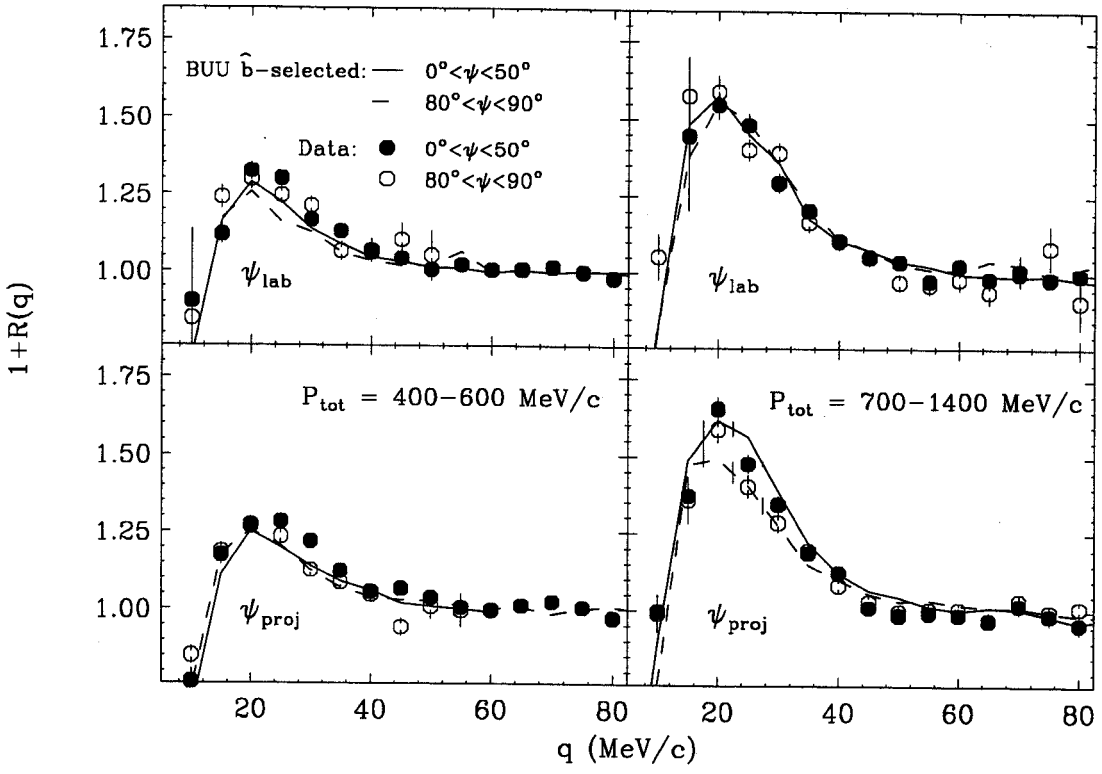

Figure 4.7. Longitudinal (solid points and curves) and transverse (open points and dashed curves) correlation functions constructed in the laboratory (top) and projectile (bottom) rest frames. Left and right panels show results for low– and high–momentum cuts, respectively. Points show data selected by the centrality cut $\hat{b}(E_t) \leq 0.36$, and the curves show BUU predictions employing the realistic impact–parameter probability distribution shown in the solid line in Figure 4.2.

panels in Figures 4.6 and 4.7), but there is an indication for a small suppression of the transverse correlation function in the projectile rest frame (right, bottom panels). This difference, is, however, of marginal statistical significance. These trends are reasonably well reproduced by the BUU calculations using $\hat{b} = 0$ (Figure 4.6) which do, however, over predict the magnitude of the peak at $q \approx 20$ MeV/c, as was already evident in Figures 4.1, 4.3 and 4.4. The BUU calculations employing the realistic impact–parameter distribution (Figure 4.7) predict a negligible difference between longitudinal and transverse correlation functions in the laboratory rest frame, in agreement with the experimental findings. In the projectile rest frame, however, these calculations predict a larger difference than observed experimentally, possibly indicating that the calculations predict somewhat too large emission from projectile spectator matter than is observed experimentally.

4.3 Source Velocity Dependence of BUU–Predicted Correlation Functions

In order to gain additional insight into the rest–frame dependence of longitudinal and transverse correlation functions predicted by BUU transport calculations, we plot in Figure 4.8 the relative split, $\langle \Delta R \rangle / \langle R \rangle$, between longitudinal and transverse correlation functions calculated for specific impact parameters, b=0, 3, and 6 fm, and for different rest frame velocities, $v_\psi = c\beta_\psi$ with respect to the laboratory frame. $\Delta R = R_{long} - R_{trans}$ is the difference between the longitudinal and transverse correlation functions evaluated in a given rest frame, R is the angle integrated correlation function which is independent of rest frame, and the $\langle\ \rangle$ denotes the average value over the interval $15\ \text{Mev}/c \le q \le 40\ \text{MeV}/c$. The top and bottom panels of Figure 4.8 show the values of $\langle \Delta R \rangle / \langle R \rangle$ predicted for the cuts P_{lab}=400–600 MeV/c and P_{lab}=700–1400 MeV/c, respectively.

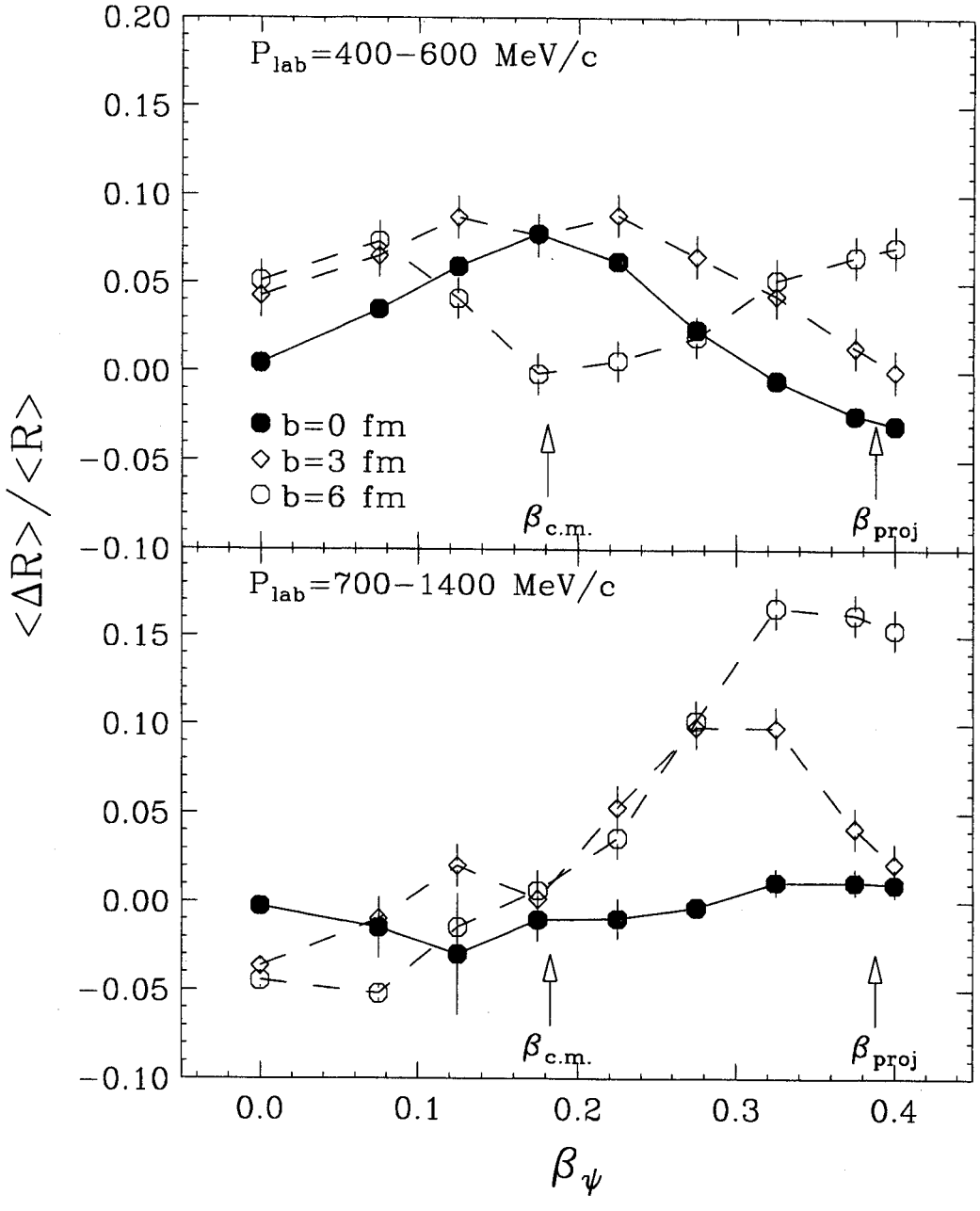

Figure 4.8. Relative difference, $\langle \Delta R \rangle / \langle R \rangle$, between longitudinal and transverse correlation functions as a function of the velocity, β_ψ, of the rest frame in which the directional ψ cuts are defined. Shown are BUU predictions for b=0 (solid circles), b=3 fm (open diamonds) and b=6 fm (open circles). Results for low– and high–momentum cuts are displayed in the upper and lower panels, respectively.

For the low momentum cut, P_{lab}=400–600 MeV/c, the predictions for central collisions (b=0, solid circles) follows the trends of the data: the largest value of $\langle \Delta R \rangle / \langle R \rangle$ is predicted in the center–of–momentum of projectile and target, and very small differences are predicted for longitudinal and transverse cuts on ψ defined in the target (laboratory) or projectile rest frames.

A qualitative interpretation of this observation was first given in Reference [Lisa 93b]. As the velocity of the ψ–frame (β_ψ) increases, the axis defined by $\vec{P}$ "rotates" through the spatial distribution of emitted nucleons, as is portrayed schematically in Figure 4.9. The relative difference between the longitudinal and transverse correlation functions, $\langle \Delta R \rangle / \langle R \rangle$, will be maximal when the axis is oriented along the distribution of emitted protons, which occurs when β_ψ assumes the value of the velocity of the rest frame of the emitting source.

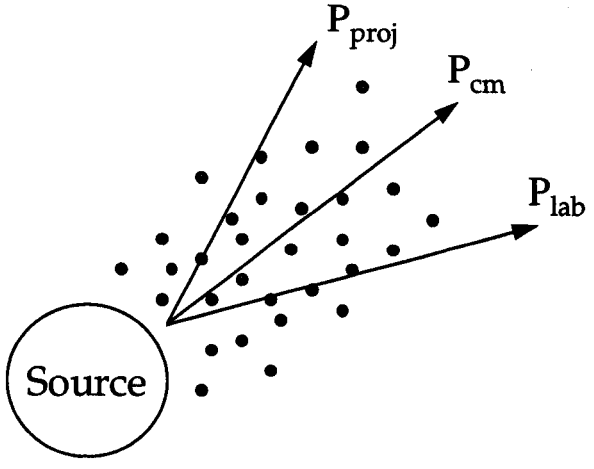

Figure 4.9. Schematic representation of a moving source (shown here in the center–of–momentum frame) and the directions probed when the angle ψ is defined in various reference frames. The direction defined by $\vec{P}$ (the longitudinal direction) is shown to "rotate" as the velocity of the defining frame increases.

A very different behavior is predicted for a large (b=6 fm) impact parameter (open circles in Figure 4.8) for the low–momentum cut. For these glancing collisions, no observable differences are predicted in the center–of–momentum frame. In contrast, significant differences are predicted when the ψ cuts are defined in the target and projectile rest frames, consistent with the intuitive expectations that emission of midrapidity protons in peripheral collisions is due to a superposition of emission from target and projectile like sources.

For the high–momentum cut, P_{lab}=700–1400 MeV/c, differences between longitudinal and transverse correlation functions are predicted to be negligible for central (b=0) collisions, independent of rest frame. These predictions follow the trends of the data. Fast particle emission in central collisions appears to occur on a fast time scale, and elongations of the phase–space distribution from finite lifetime effects becomes negligible. For larger impact parameters, however, $\langle \Delta R \rangle / \langle R \rangle$ is predicted to become large for rest–frame velocities close to the projectile velocity, indicating that fast, forward–emitted particles in peripheral collisions are predicted to have substantially (if not predominant) contributions from the decay of projectile residues. Note, however, that the BUU predictions for energetic emission in peripheral collisions do not reproduce the data – see Figure 4.1 and Reference [Lisa 93b]. Furthermore, for our peripheral cut, no statistically significant differences between longitudinal and transverse correlation functions were found in the target, projectile, nor in the center–of–momentum rest frames [Lisa 93b, 93c]. These findings corroborate that the details of proton emission in peripheral collisions are not well described by our calculations.

Chapter 5 – Toroidal Density Distributions

This chapter addresses the practicality of using the two–proton correlation function as a means of identifying toroidal density distributions that are predicted to form in heavy–ion collisions. After defining directional cuts, we explore the sensitivity of the correlation function to exotic shapes (disks and tori) employing increasingly realistic assumptions, including the effects of proton emission over extend time scales and impact parameter averaging.

5.1 Correlation Functions from Schematic Sources

Calculations with the BUU model predict that disk–shaped [More 92] or toroidal [Baue 92a, Gros 92, Bord 85, Xu 93, Hand 94] configurations may be produced in central heavy–ion collisions. Different observables have been suggested to find a signature of a toroidal breakup [More 92, Baue 92a, Xu 93, Phai 93a, Glas 93], but no experimental evidence for the formation of tori as yet exists. The suggested observables were based on either intuitive arguments [More 92, Baue 92a, Xu 93] or on schematic calculations [Phai 93a, Glas 93] in which a multifragment disintegration of the torus was assumed. However, none of these suggestions was substantiated by dynamical calculations capable of exploring the space–time evolution of the reaction zone. A consistent dynamical treatment is possible for nucleon emission and for the calculation of two–proton correlation functions, using the Koonin–Pratt formalism and the actually phase–space distributions predicted by the BUU theory.

Our analysis concentrates on simulations of central $^{36}Ar + ^{45}Sc$ collisions at E/A=80 MeV, performed with very high statistics. As shown in the previous chapter, measured impact–parameter–filtered correlation functions for this reaction were reproduced successfully by BUU calculations. These same calculations predict the formation of a toroidal density distributions [Hand 95a]. The data were, however, also reproduced by assuming emission from a spherical

source of finite lifetime [Lisa 93b]. Hence, the agreement with BUU calculations could not be taken as evidence for the predicted toroidal shapes; see also [Hand 94].

Shown in Figure 5.1 is the calculated evolution of the *residual* system for strictly central (b=0) ^{36}Ar + ^{45}Sc collisions at E/A=80 MeV. Panels from left to right show density projections at times t=10, 50, 100 and 150 fm/c; top and bottom panels show projections onto the (x,y) and (x,z) planes, respectively, with the z–axis chosen parallel to the beam axis. The system is shown to evolve into a toroidal configuration which is symmetric about the beam axis. In order to isolate effects due to the spatial configuration of the emitting source, we make stringent cuts on the directions of total and relative momenta, as shown in Figure 5.2.

We first cut on the orientation of the total momentum, $\vec{P}$, which is selected to lie within $\pm 10°$ of the (x,y) plane. The relative momentum, $\vec{q}$, is then selected (within $\pm 10°$) along three directions: $\vec{q}_{par}$ is parallel to $\vec{P}$ and thus sensitive to the source dimension and its lifetime; $\vec{q}_{beam}$ and $\vec{q}_{perp}$ are perpendicular to $\vec{P}$ and thus insensitive to lifetime effects. $\vec{q}_{perp}$ lies in the (x,y) plane and is thus sensitive to the radius of the torus, while $\vec{q}_{beam}$ is parallel to the beam axis and is thus sensitive to the thickness of the torus.

The solid and dashed curves in Figure 5.3 show two–proton correlation functions calculated under the simplifying assumption of instantaneous emission from the volume of the toroidal density distribution at t=100 fm/c, as reproduced (from Figure 5.1) in the left hand panels of Figure 5.4. The momenta for this simulation were chosen isotropic in the center–of–mass frame, with a flat distribution for each Cartesian component ranging from –200 to 200 MeV/c. Statistical uncertainties of the calculations are indicated by the error bars. The correlation functions for $\vec{q}_{par}$ and $\vec{q}_{perp}$ (not shown in the figure) are practically

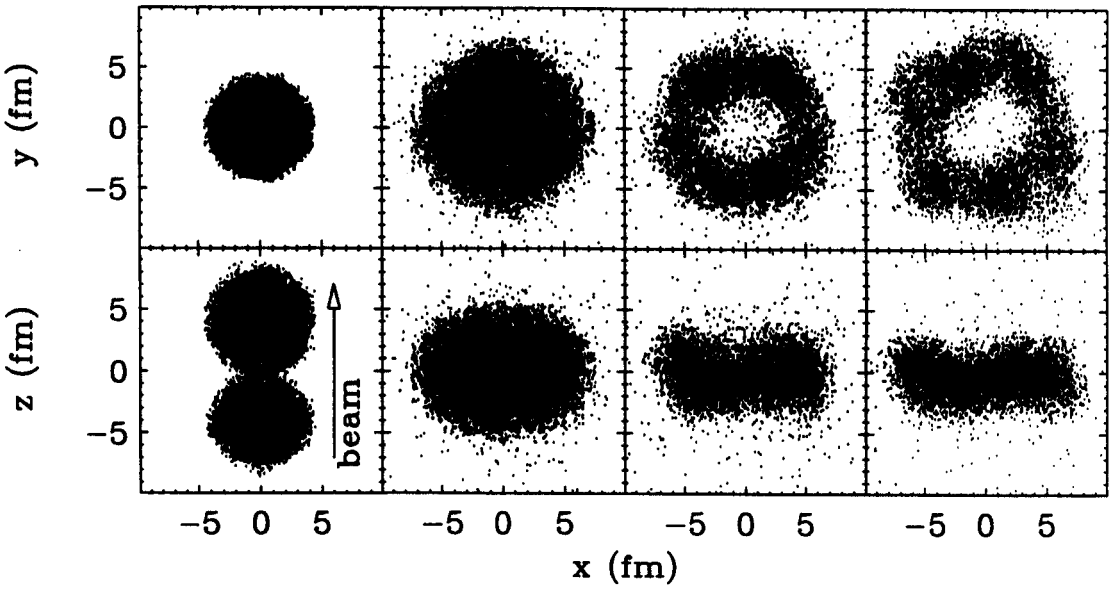

Figure 5.1. Residual system predicted by BUU transport calculations for b=0 collisions of ^{36}Ar + ^{45}Sc at E/A=80 MeV at time t=10, 50, 100, and 150 fm/c. The top panels show distributions viewed along the beam axis; the bottom panels show distributions projected onto a plane which contains the beam axis.

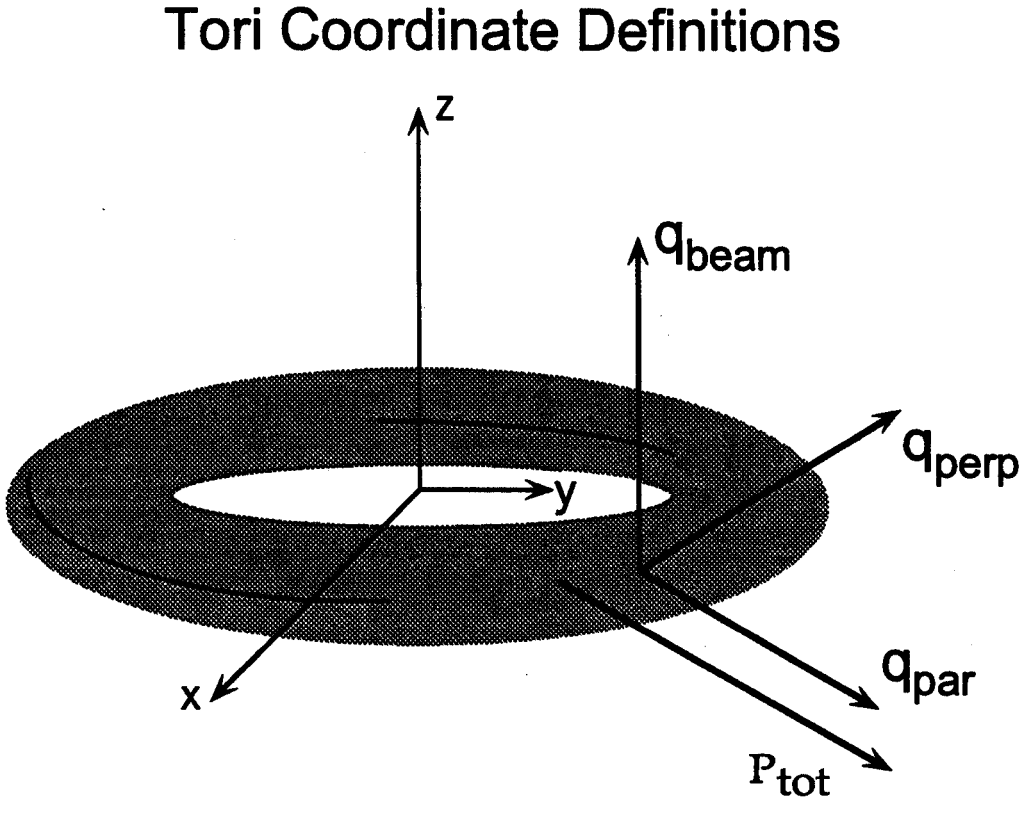

Figure 5.2. Geometry of a torus and the directions of applied cuts on $\bar{q}$ used in all of our calculations.

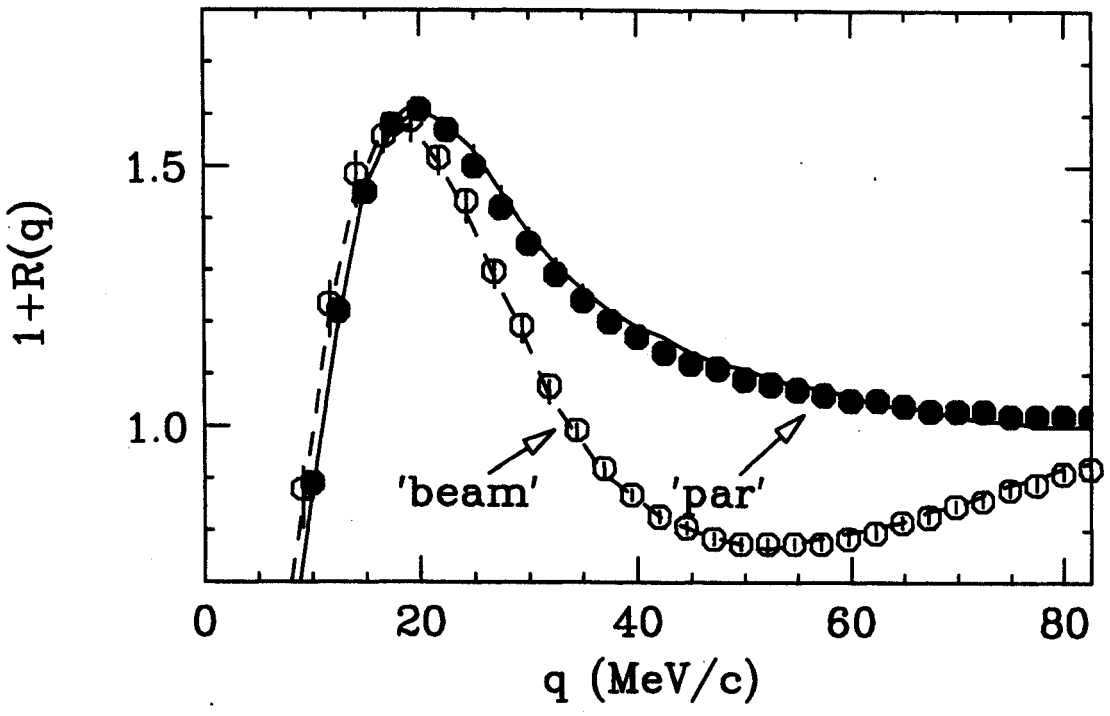

Figure 5.3. Comparisons of correlation functions calculated for a zero–lifetime torus and disk, using the directional cuts defined in Figure 5.2.

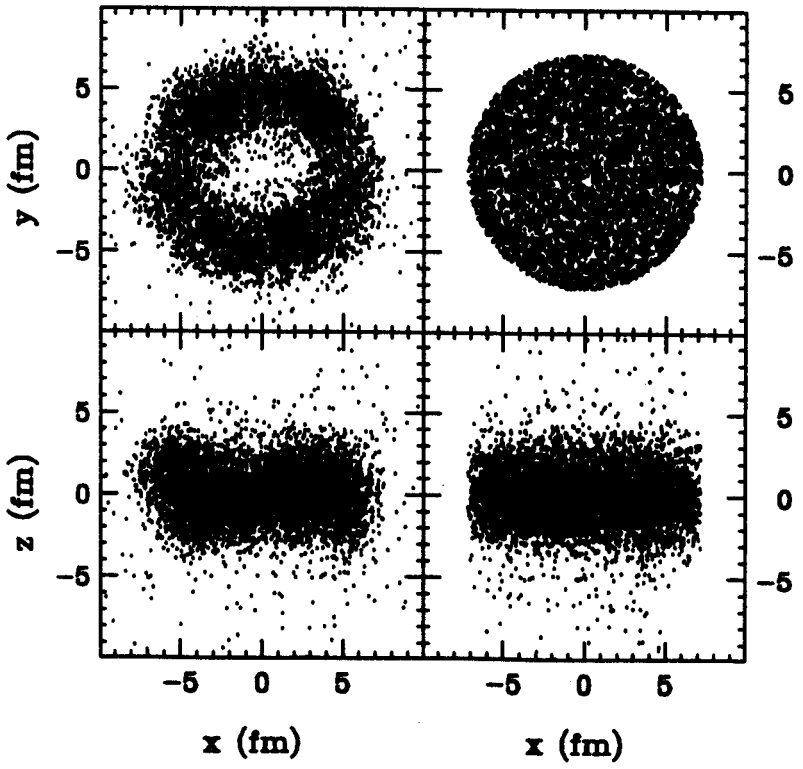

Figure 5.4. Left panels: density distribution of the torus at t=100 fm/c, taken from Figure 5.1. Right panels: density distribution of a "disk," formed by uniformly filling in the hole of the torus. The radius of the disk's density distribution was chosen to produce the same correlation–function peak height as that produced by the torus.

degenerate, consistent with an instantaneous emission. The correlation function for $\vec{q}_{beam}$ exhibits a strongly enhanced Pauli suppression, reflecting the shorter dimension of the torus (see Figures 5.1 and 5.4). The open and solid points in Figure 5.3 represent the results of calculations for instantaneous emission from a disk–shaped distribution obtained by uniformly filling the "hole" of the doughnut. (The torus and "disk" density distributions, which have approximately equal volumes, are compared in Figure 5.4.) The calculations for the two source geometries are very similar, indicating that our choice of directional cuts is not sensitive to the "hole" of the torus. It will be even more difficult, if not impossible, to differentiate between a disk and a torus with experimental correlation functions which average over the temporal evolution of the reaction zone over a finite window of impact–parameters. However, one may still hope to distinguish these "flat" shapes from spherically symmetric sources, even in a more realistic reaction scenario.

The degeneracy of $R(\vec{q}_{perp})$ and $R(\vec{q}_{par})$ is removed if emission occurs with a fixed lifetime, as is shown in Figure 5.5. Specifically, we used the same toroidal spatial distribution employed previously, with an added exponential time dependence, $dN/dt \propto \exp(-t/\tau)$, with $\tau = 25\,\mathrm{fm/c}$. The choice of τ was made for consistency with Reference [Lisa 93b]. The magnitude of the peak of the correlation function at $q \approx 20\,\mathrm{MeV/c}$ is reduced, and the correlation functions are ordered approximately as $R(\vec{q}_{par}) \geq R(\vec{q}_{perp}) \geq R(\vec{q}_{beam})$, reflecting increased Pauli suppression due to smaller average particle separations along the respective directions.

Figures 5.3 and 5.5 suggest that two–proton correlation functions are well–suited to extract useful information about nonspherical sources of fixed geometries. This simplified scenario (of emission from a non–evolving source) serves only as an example. More realistic calculations will incorporate the

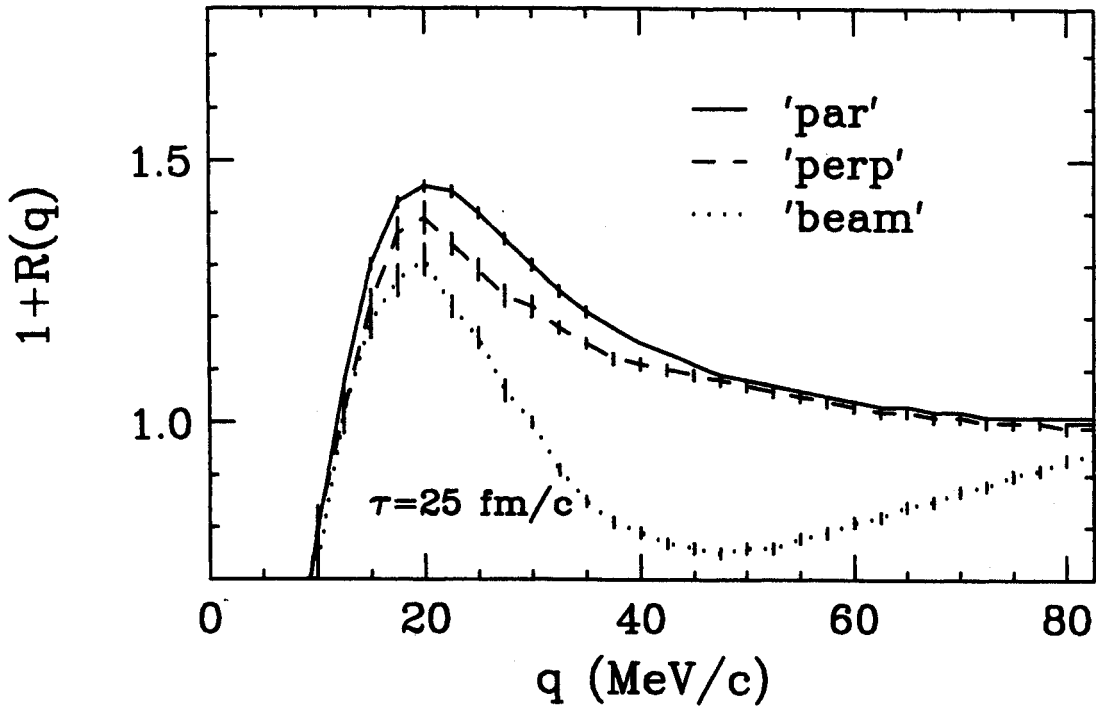

Figure 5.5. Two–proton correlation functions predicted for emission from a torus assuming an exponential time dependence of mean emission time τ=25 fm/c.

dynamics of proton emission, and will include contributions from larger impact–parameter collisions, as described in the following section.

5.2 Correlation Functions from Model Predictions

Figure 5.6 shows that the BUU transport model predicts, for strictly central collisions, that most of the protons are emitted before the torus is fully formed (at $t \approx 100$ fm/c). This suggests that the differences between our directional cuts will be reduced, when employing the phase–space density distribution predicted by the BUU model, due to the substantial proton emission from the compact initial configurations (see Figure 5.1). Figure 5.7 shows that when employing the same cuts as defined in Figure 5.2 (with no restrictions on the magnitude of the total momentum) that the predicted differences are significantly reduced. Although there is a clear difference between the correlation functions cut on $\vec{q}_{par}$ and $\vec{q}_{perp}$, indicative of the source lifetime, the toroidal signature (the difference between $\vec{q}_{perp}$ and $\vec{q}_{beam}$) is substantially diminished.

Further complications arise when unavoidable contributions of nonzero impact parameters are taken into account. Figure 5.8 illustrates the strong impact–parameter dependence of the shape and orientation of the residual system calculated from the BUU theory at t=100 fm/c. Toroidal shapes are shown to be predicted for small (nonzero) impact parameters, but their symmetry axes are tilted away from the beam axis. For impact parameters larger than about 3 fm, the residual system assumes stretched configurations leading to a binary exit channel, possibly accompanied by neck emission [Mont 94].

The impact parameter distribution used for the calculation of the two–proton correlation function for central collisions of ^{36}Ar + ^{45}Sc at E/A=80 MeV was shown in the solid line of Figure 4.2. With our choice of b_{max}=10 fm, this figure shows that the most likely impact–parameter for our central cut is about 3

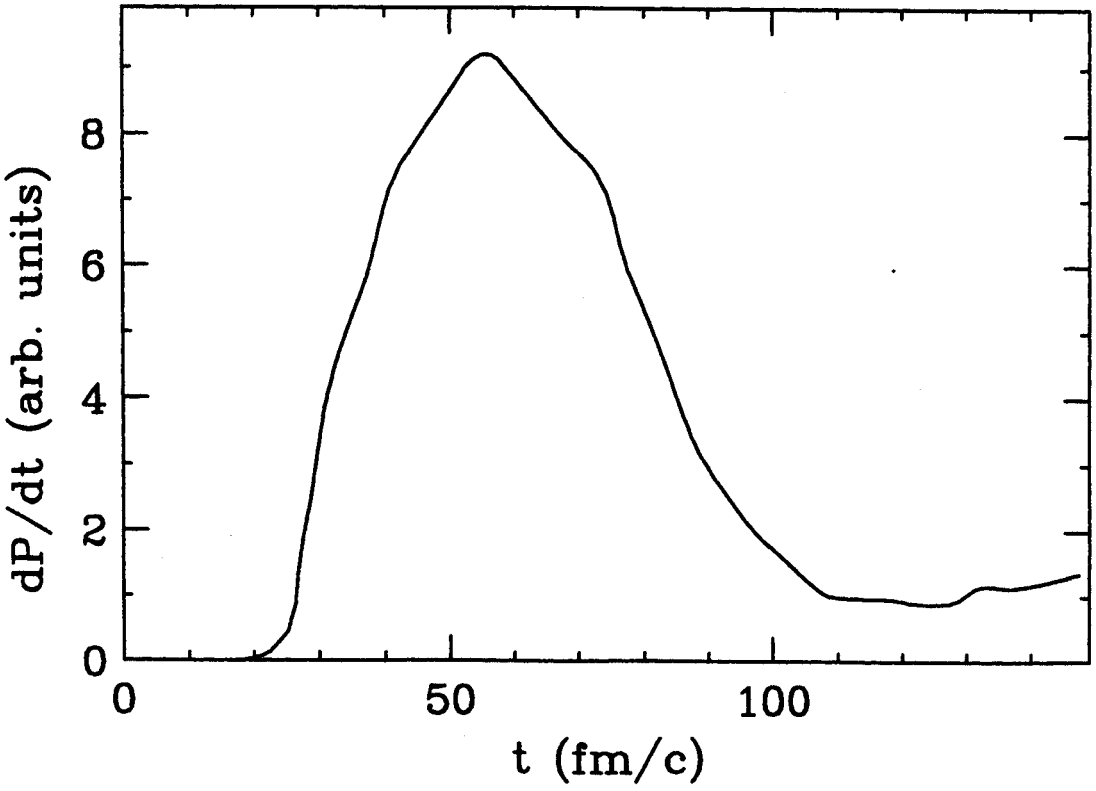

Figure 5.6. The time dependence of proton emission, dP/dt, predicted for b=0 collisions of ^{36}Ar + ^{45}Sc at E/A=80 MeV, showing that most of the protons are emitted before t=100 fm/c, when the torus is fully formed (see Figure 5.1).

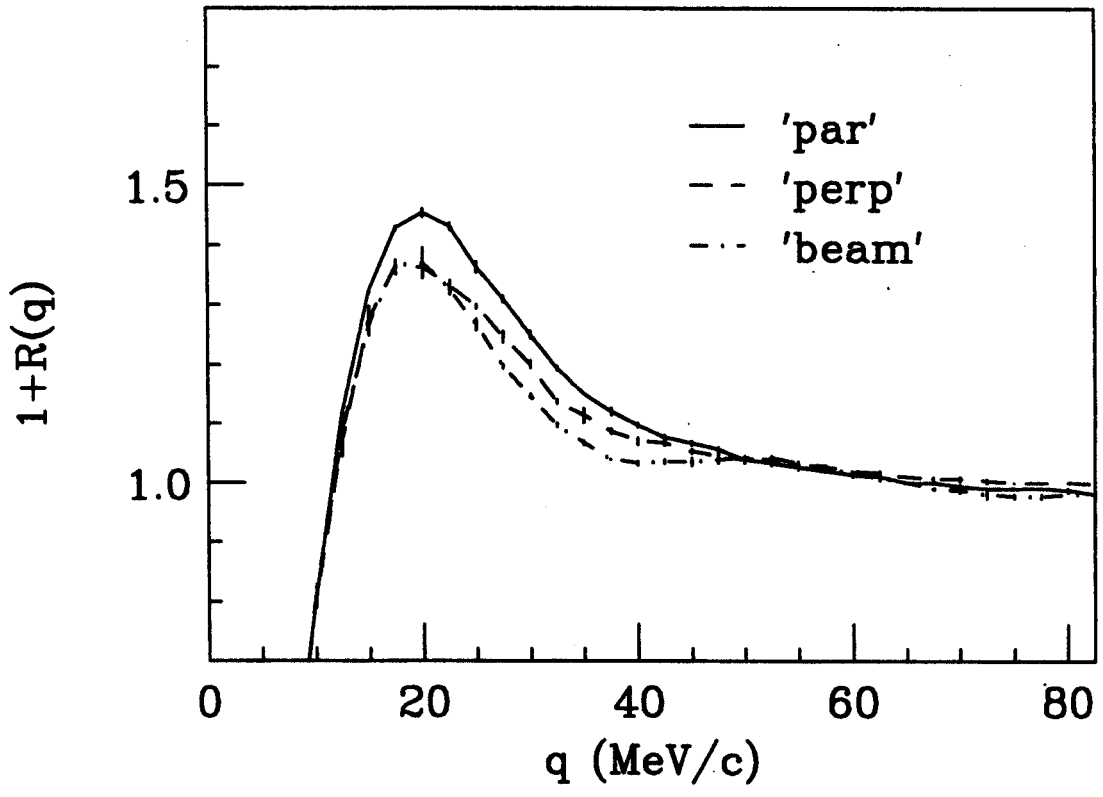

Figure 5.7. Two-proton correlation functions predicted by BUU transport calculations for b=0 ^{36}Ar + ^{45}Sc collisions at E/A=80 MeV.

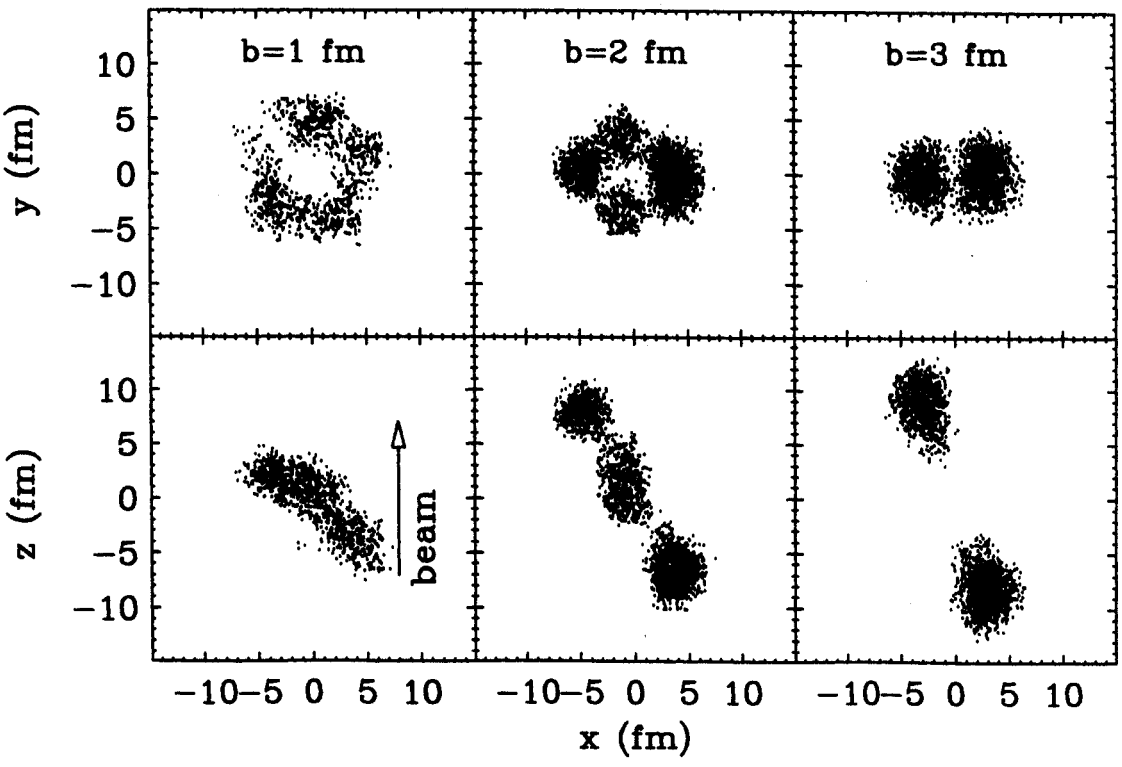

Figure 5.8. Residual system predicted at t=100 fm/c by BUU calculations for $^{36}Ar + ^{45}Sc$ collisions E/A=80 MeV for the indicated impact–parameters.

fm, and that the distribution contains substantial contributions from larger impact–parameters.

Figure 5.9 illustrates the effects of impact–parameter averaging. The correlation functions shown in the figure were calculated using the fixed–axis directional cuts defined in Figure 5.2 and by employing the central–cut impact–parameter distribution shown in Figure 4.2. For tilted tori (i.e., for collisions with $b > 0$), the directional cut parallel to the beam axis no longer probes the smallest dimension of the residual system. As a consequence, the correlation function $R(\vec{q}_{beam})$ is less suppressed, and the relative magnitudes of the three correlation functions are different than in Figures 5.5 and 5.7. Furthermore, dynamical correlations due to impact–parameter averaging [Gong 91b] become important due to the non–negligible sideward directed flow, causing additional distortions at larger values of relative momenta ($q > 40$ MeV/c). The qualitative features of impact–parameter averaged correlation functions are therefore different from those for purely central collisions, making the extraction of a signal of toroidal (or disk–shaped) density distributions difficult, if not impossible. Nevertheless, BUU calculations predict correlation functions with shapes distinct from those representing emission from spherical sources of finite lifetime.

Unfortunately, the statistical accuracy of our experimental data (References [Hand 94, Lisa 93a, 93b]) is not sufficient to allow such tests. Impact–parameter–selected correlation functions of improved statistical accuracy and with appropriately chosen directional cuts should, however, be able to test the nontrivial space–time evolution predicted by microscopic transport calculations. We believe, however, that such an experimental signature would be very difficult to interpret in a model–independent way.

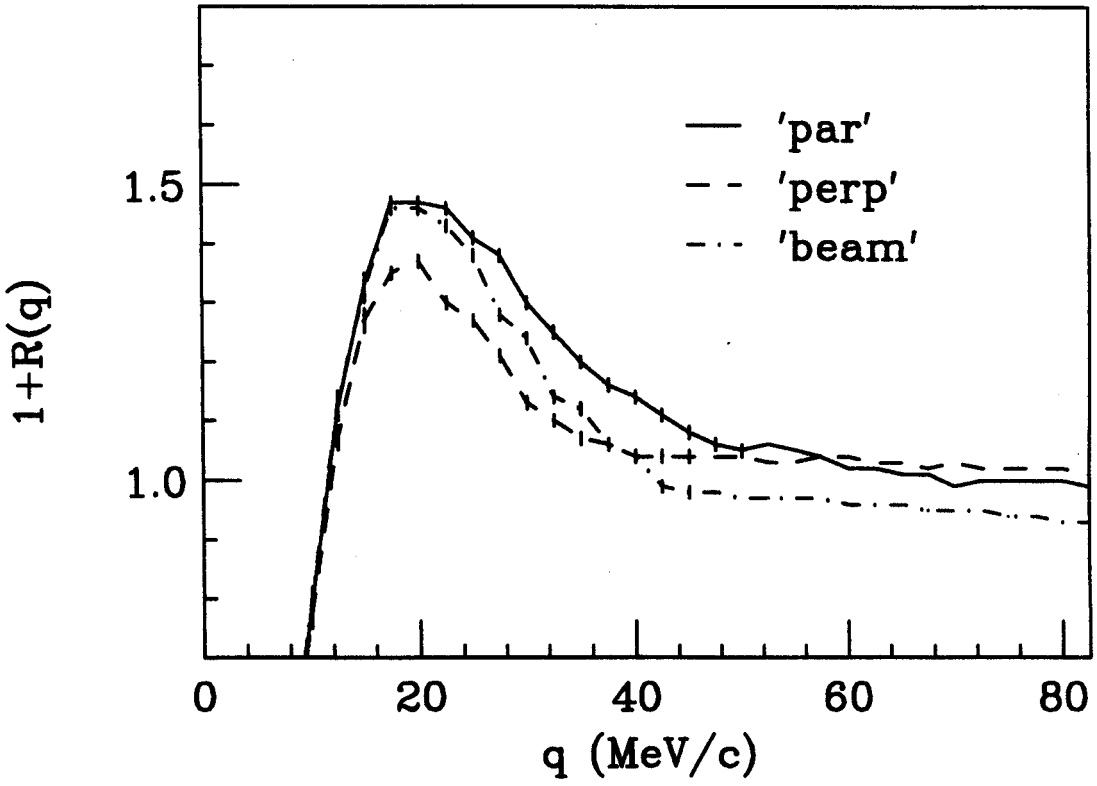

Figure 5.9. Two-proton correlation functions predicted by BUU transport calculations for central ^{36}Ar + ^{45}Sc collisions at E/A=80 MeV. The impact parameter distribution used for these calculations is shown in Figure 4.2.

Chapter 6 – $^{36}Ar + ^{45}Sc$ collisions at E/A=120 and 160 MeV

The two–proton correlation function has proven to be a valuable tool in studying nuclear reactions, and for testing the space–time evolution of nuclear collision dynamics predicted by microscopic transport theories. They are sensitive to source–size and lifetime effects [Lisa 93b]. For energies below a few tens of MeV per nucleon, where long–lived evaporative emission is expected, measured two–proton correlation functions were found to be consistent with compound–nucleus model predictions [Gong 91b, Elma 93]. At high energies, above 200 MeV per nucleon, nuclei should be vaporized and semi–classical cascades should provide a valid description. For collisions at intermediate energies, nuclei disintigrate by emitting a large number of light clusters and intermediate mass fragments. Since this energy range represents the transition from liquid–like to gas–like behavior, it may be the most interesting region to study, but it is also the most difficult to model theoretically.

BUU calculations were successful in reproducing two–proton correlation functions measured at energies below about 100 MeV per nucleon [Gong 91a, 91b, Lisa 93b, Hand 94, Poch 87, Kund 93]. In chapter 4 and References [Lisa, 93c], the BUU model was shown to reproduce detailed depenencies of the measured two–proton correlation function on the total momentum of the proton pair and on the orientation of the relative momentum remarkably well. The emerging discrepencies for peripheral collisions were attributed to an inadequate treatment of the nuclear surface [Lisa 93b, Hand 94], but not to a fundamental limitation of the BUU formalism. Rather surprisingly, the model failed to explain inclusive measurements for $^{40}Ar+^{197}Au$ at E/A=200 MeV [Kund 93] where it should have been on even more firm theoretical grounds than at the lower energy. Improved agreement was obtained by using *two–*proton emission probabilities calculated with the Quantum Molecular Dynamics model [Kund 93, Aich 91], but such calculations could not reproduce the

correlation functions measured at 60 MeV per nucleon [Kund 93, Poch 87], and did not therefore resolve the problem. In addition, the correlation function measured at E/A=200 MeV displayed an unusual insensitivity to the protons' energy and a filling in of the minimum at relative momentum $q \approx 0$, neither of which were observed at lower energies.

Further insight can be expected from impact–parameter filtered data at higher energy. Therefore, we measured two–proton coincidences for collisions of ^{36}Ar + ^{45}Sc at E/A=120 and 160 MeV. In this chapter, we present comparisons of measured correlation functions with predictions of the BUU transport model and we explore the importance of particle–unstable resonances in correlation studies.

6.1 Single Proton Energy Spectra

The measurement of light charged particles is complicated by the possibility of reactions with nuclei within the detector. When this occurs, the incident particle's energy is not accurately measured because of a nonzero Q–value and the emission of energetic neutral particles (neutrons and photons). Following the methods of References [Gong 91c, Kox 87], we calculated the probability of nuclear reaction loss for protons entering a 10 cm long CsI(Tl) crystal, shown in Figure 6.1. A proton of 150 MeV incident energy has about a 20% chance of undergoing a nuclear reaction within the detector. The correlation function is not affected by such reactions since the losses affect both numerator and denominator. However, these losses must be corrected for in singles spectra analyses, especially for reactions at higher beam energies, from which many energetic protons are emitted.

Shown in Figure 6.2 are the single–proton energy spectra for our ^{36}Ar + ^{45}Sc collisions at E/A=120 and 160 MeV. The solid points points show the energies of protons detected at $\langle \vartheta_{lab} \rangle = 31°$ and histograms show the predictions

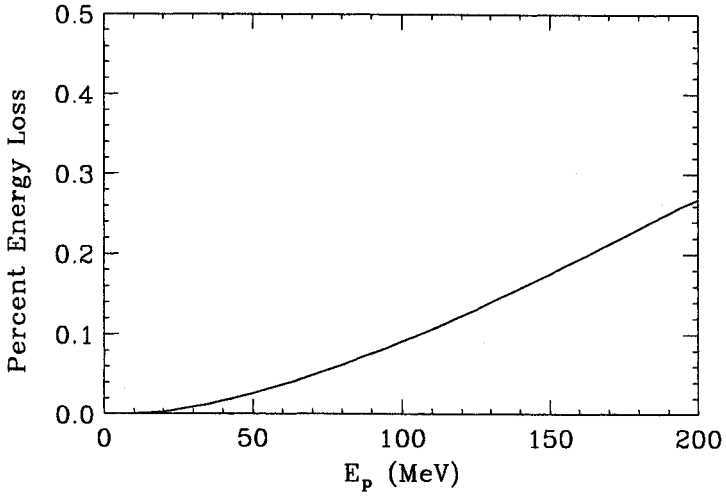

Figure 6.1. Probability for nuclear reaction loss for protons incident on a 10 cm CsI(Tl) crystal.

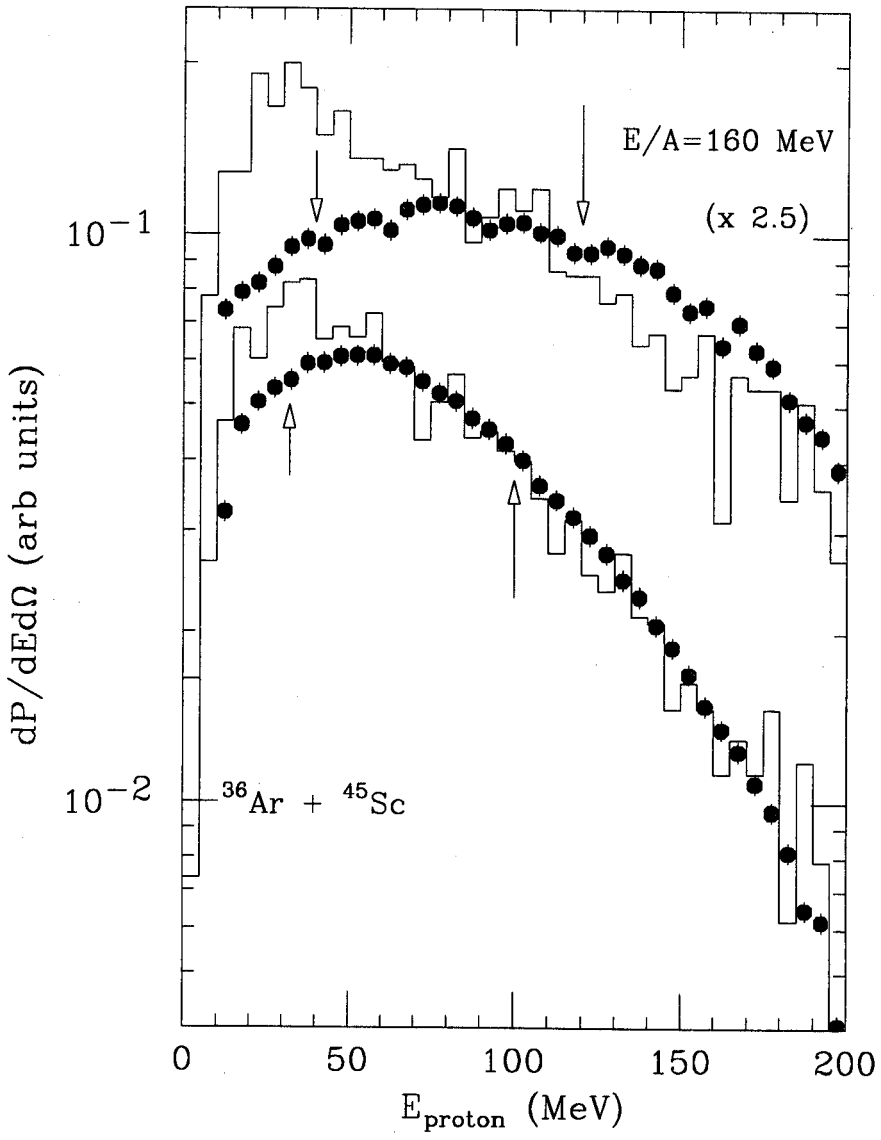

Figure 6.2. Laboratory frame proton energy spectra measured at θ_{lab}=31° for central (b/b_{max} = 0 - 0.3) collisions of ^{36}Ar + ^{45}Sc at E/A = 120 and 160 MeV (solid points) are compared with the predictions of BUU (histograms). Relative normalization gives equal areas for measured and predicted spectra for E_{proton}> 50 MeV. The arrows indicate average values of E^{lab}_{proton} corresponding to low and high momentum cuts used to analyze the correlation function in this chapter.

of the BUU model. The BUU calculations over predict the low–energy proton yields, but they reproduce the approximate shape of the high–energy tails. This over prediction of proton yields at low energy has been observed before, and attributed to the model's inability to treat the formation of bound clusters [Gong 93]. These clusters should preferentially form in regions of phase–space where nucleon population density is high, hence more protons should be "lost" to bound clusters at lower than at higher proton energy.

6.2 Measured Proton–Proton Correlation Functions

The correlation functions presented in this chapter are gated on centrality, total proton center–of–mass momentum, and orientation of relative and total proton momenta. In order to understand the effects of our detector upon the correlation function, we show in Figures 6.3 and 6.4 the acceptance of the hodoscope in the p_x vs. p_z plane for for single–proton center–of–mass momentum cuts $p_{cm} = P_{cm}/2$, for our two energies, E/A=120 and 160 MeV, respectively. These figures are similar to Figure 4.5 with the momentum cuts now defined in the center–of–mass frame. The dashed lines indicate the angular acceptance of the hodoscope $\vartheta_{lab} = 30°–45°$. The dotted and hatched areas correspond to our momentum cuts, $P_{cm} = 200 - 400$ and $400 - 800\ \mathrm{MeV/c}$, respectively. The two solid circles in each plot depict the Fermi momentum spheres of projectile (centered at $p_z/A = 487\ \mathrm{MeV/c}$ and $p_z/A = 568\ \mathrm{MeV/c}$, respectively) and target (centered at $p_z/A = 0$).

Similar to the lower energy reaction, the low momentum cut selects protons emitted at large transverse angles with low energies with respect to the center–of–mass rest frame. Again, the high–momentum cut selects protons with velocities closer to the projectile than target velocity.

In Figure 6.5 we show measured momentum–integrated two–proton correlation functions gated on centrality for our E/A=120 (top) and 160 (bottom) MeV reactions. Consistent with References [Lisa 93a, 93c], our measurements

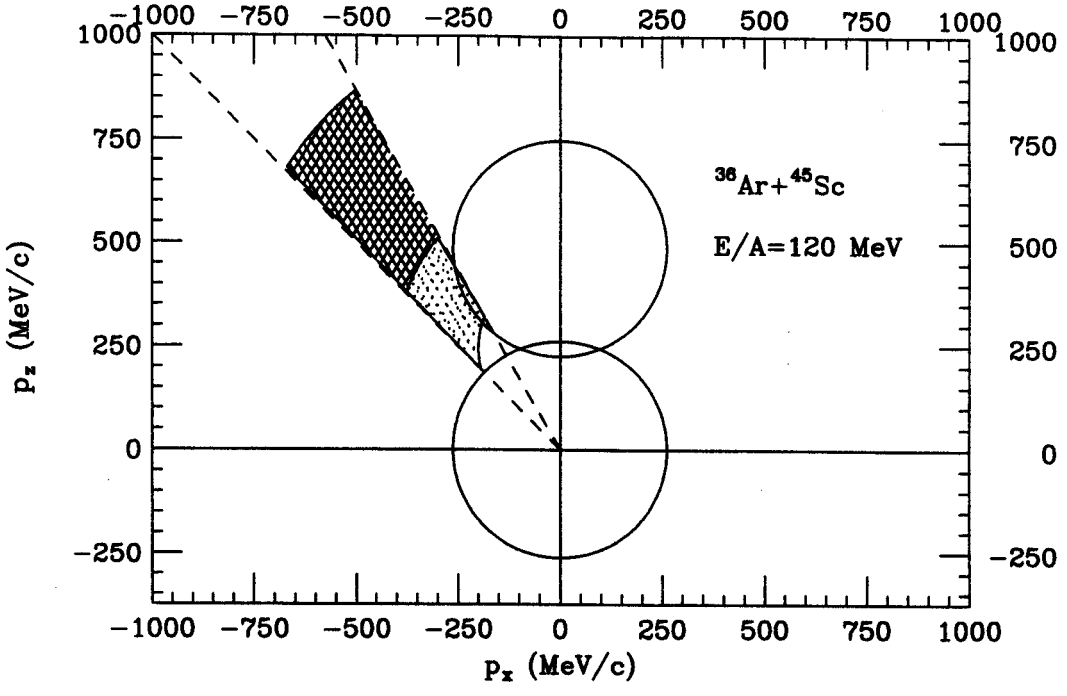

Figure 6.3. Schematic of detector acceptance and center–of–mass momentum cuts for our E/A=120 MeV reaction. Dashed lines represent the detector boundaries at ϑ_{lab} = 30°–45°. Dotted and hatched areas represent the low– and high–momentum cuts, P_{cm} = 200 – 400 and 400–800 MeV/c, respectively. Solid circles depict Fermi spheres of target and projectile.

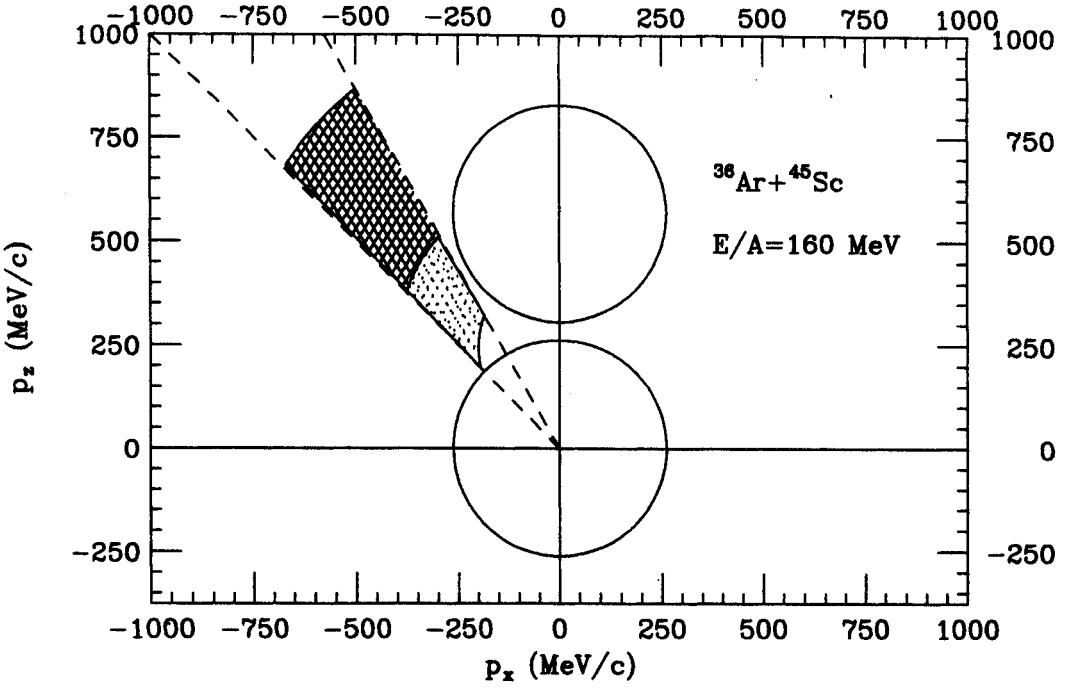

Figure 6.4. Schematic diagram similar to Figure 6.3, appropriate for our E/A=160 MeV reaction.

show a stronger correlation from peripheral than from central collisions, for both bombarding energies. This observation is consistent with a geometric interpretation of the reaction zone: the "source" is formed by the physical overlap of target and projectile, hence peripheral collisions lead to smaller sources.

Figures 6.6 and 6.7 show the measured correlation functions cut on both centrality and proton pair momentum, for our E/A=120 and 160 MeV reactions, respectively. The correlation functions at E/A=120 MeV show a strong dependence on total proton pair center–of–mass momentum, for both central (top) and peripheral (bottom) collisions. Faster protons are shown to be more strongly correlated, suggesting that they are emitted from a smaller source or on shorter time scales than the slower protons. This trend is consistent with previous impact–parameter gated measuremets [Lisa 93a, 93c] for the same system at E/A=80 MeV. For our higher energy reaction (Figure 6.7), the correlation function displays little dependence on proton–pair momentum for central collisions (top panel), but does show a sensitivity for more glancing collisions (bottom panel). The near–degeneracy of low– and high–momentum correlation functions for central collisions may indicate that all protons are emitted on similar time scales, and that there is no evaporative cooling of the source. The momentum dependence at E/A=160 MeV for both central and peripheral collisions is smaller than that observed at E/A=120 MeV.

These trends are summarized in Figure 6.8, where the average value of the correlation function in the peak region q=15–25 MeV/c, $\langle 1+R \rangle_{q=15-25\,MeV/c}$, is plotted versus the total proton–pair center–of–mass momentum, P_{cm}, for the two centrality cuts for both the E/A=120 (top) and E/A=160 MeV (bottom) reactions. Error bars include statistical uncertainties as well as an estimate of the uncertainty due to normalization in the high–q region (q=60–80 MeV/c). While the measured results at E/A=120 MeV show a modest momentum dependence,

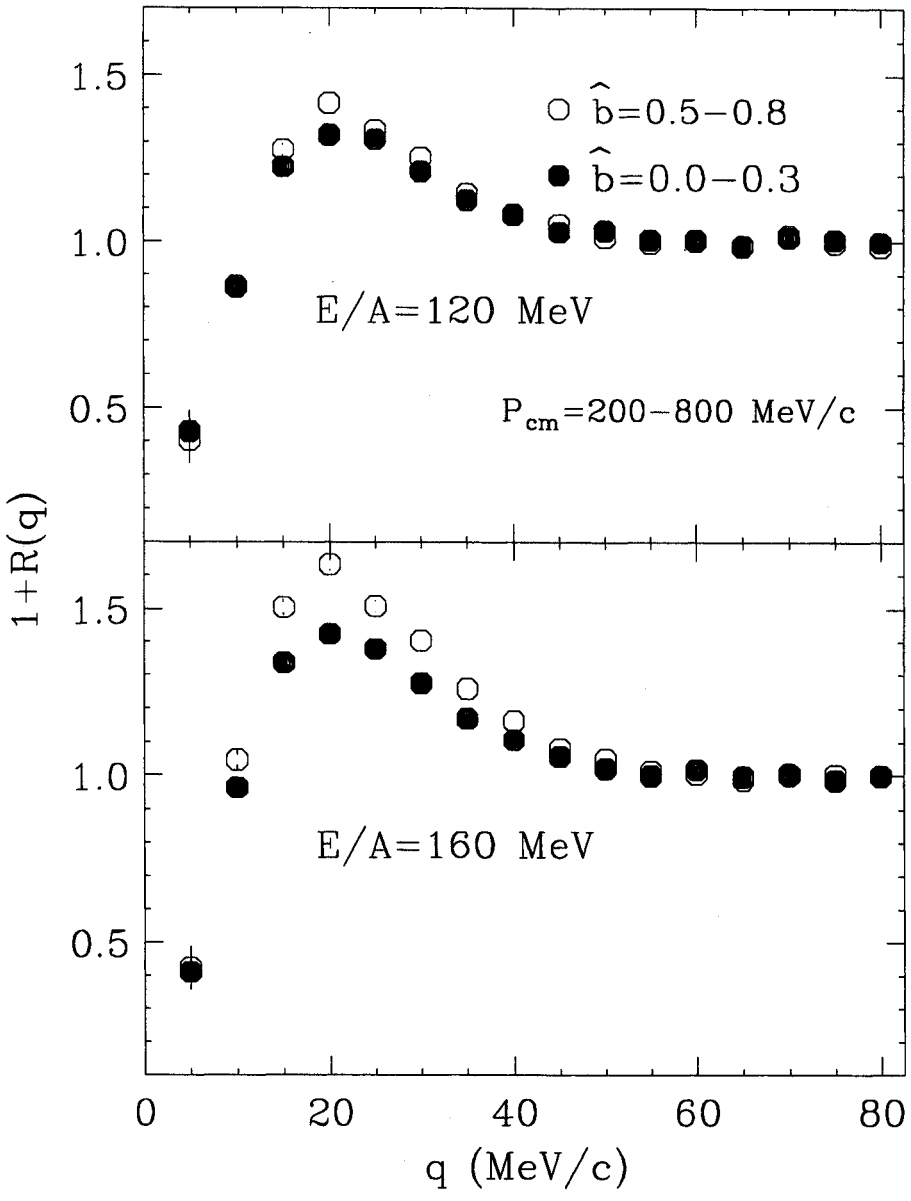

Figure 6.5 Momentum–integrated two–proton correlation functions for our E/A=120 MeV (top panel) and E/A=160 MeV (bottom panel) reactions. Central events are indicated by solid points, while peripheral events are shown in open points.

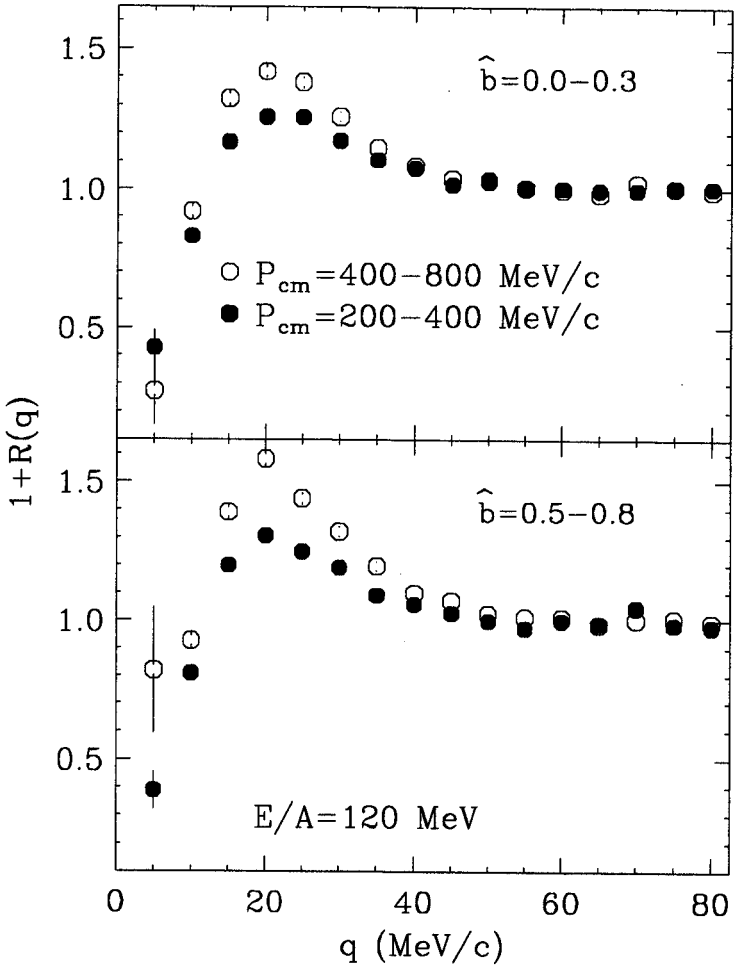

Figure 6.6 Measured two–proton correlation functions, cut on total proton–pair center–of–mass momentum, P_{cm}, and on centrality for our E/A=120 MeV reaction. Open and solid points represent high– and low–momentum protons, cut on central (upper panel) and peripheral (lower panel) events.

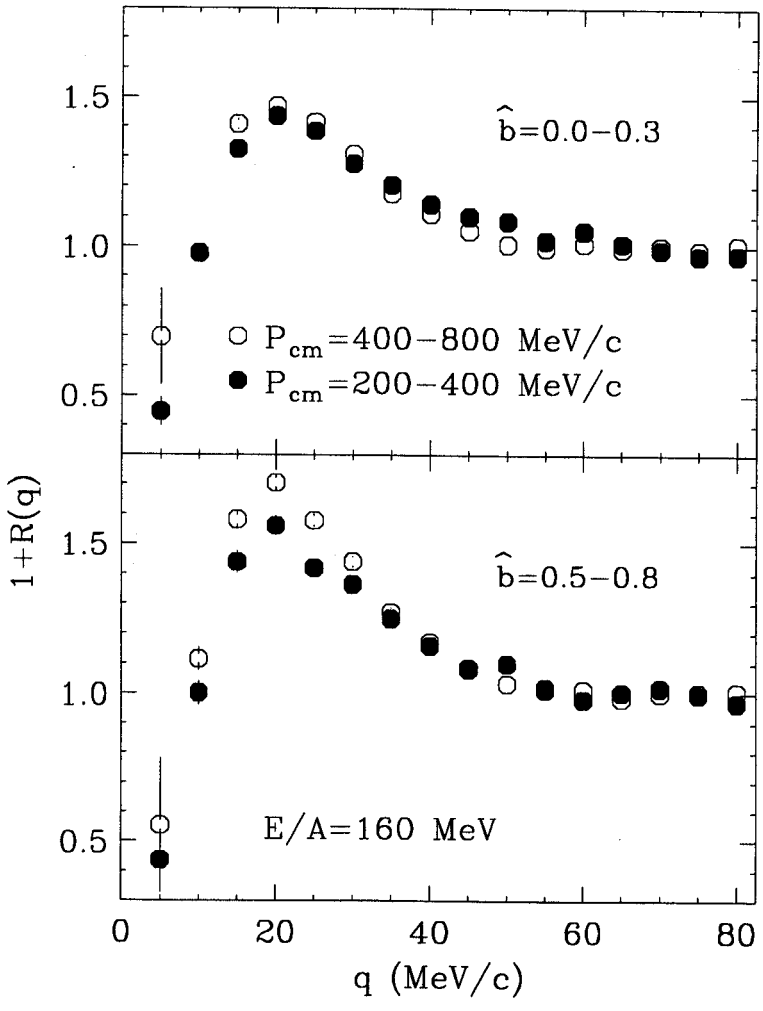

Figure 6.7 Measured two–proton correlation functions, cut on total proton–pair center–of–mass momentum, P_{cm}, and on centrality for our E/A=160 MeV reaction. Open and solid points represent high– and low–momentum protons, cut on central (upper panel) and peripheral (lower panel) events.

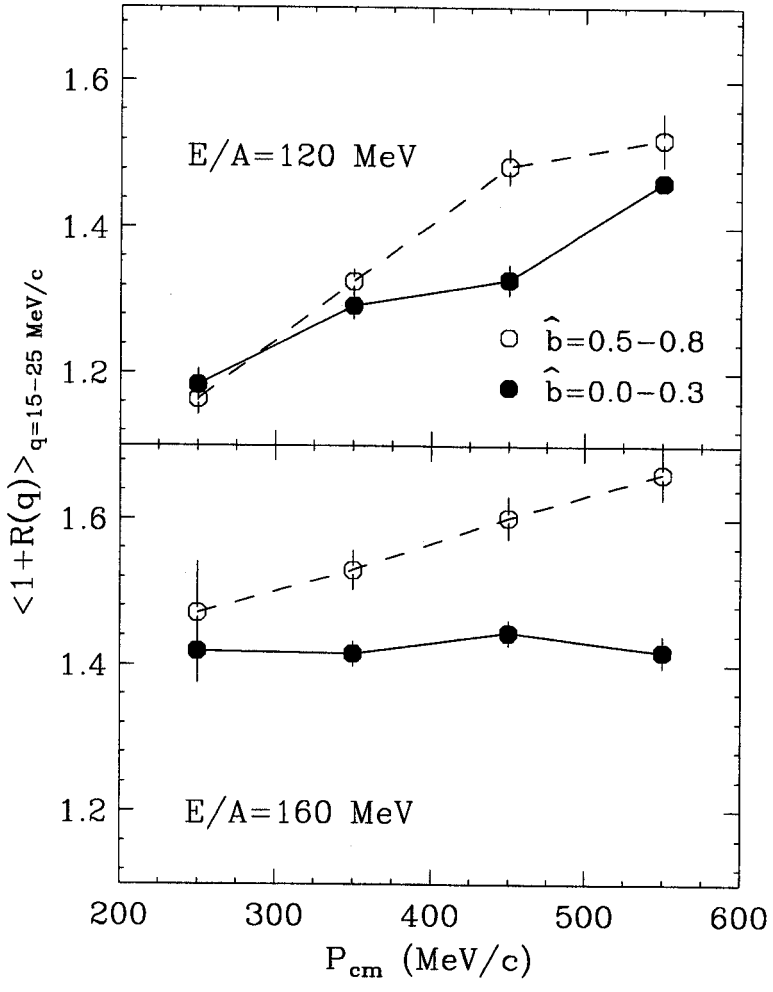

Figure 6.8. The total proton–pair momentum dependence of the average value of the two–proton correlation function ($\langle 1+R\rangle_{q=15-25\,MeV/c}$) in the peak region, q=15–25 MeV/c for our E/A=120 MeV (top) and E/A=160 MeV (bottom) results. Central events are shown in solid points, and peripheral events in open points. The lines are drawn to guide the eye.

the correlation functions at E/A=160 MeV show a weak dependence for peripheral collisions, and no dependence for central collisions.

6.3 Comparisons of BUU Predictions with Experimental Results

The diminishing momentum dependence for higher beam energies was established by Reference [Kund 93] for impact–parameter inclusive measurements of $^{40}Ar + ^{197}Au$ collisions at E/A=200 MeV, which could not be reproduced by BUU calculations. However, correlation functions are known to be highly sensitive to impact–parameter (as shown in Figures 6.5–6.8), and a more stringent test of the BUU model would include gating on centrality as well as momentum. The BUU model is know to fail at lower energies for peripheral collisions, possibly because of an inadequate treatment of the nuclear surface. For this reason, and for better source characterization, we restrict ourselves to central collisions, defiend by $\hat{b} = 0 - 0.3$, for both experiment and theory (see section 2.3.2).

For this analysis, we used the BUU model of Bauer [Baue 86, Baue 87, Li 91a, Li 91b, Baue 92a] with a stiff equation of state (K=380 MeV), and the nucleon–nucleon cross section was set to its value in free space. A proton was considered "emitted" if its local density was less than one–eighth that of normal nuclear matter ($\rho_0 \approx 0.16$ fm^{-3}), before a time $t \le t_{cut} = 150 fm/c$ (and if it did not reenter a region of higher density before the calculation was terminated at t=200 fm/c). Some theoretical uncertainty exhists with respect to the choices of t_{cut}=150 fm/c and freeze–out density, $\rho_f = \frac{1}{8}\rho_o$, which were consistent with previous studies [Boal 90, Gong 90c, 91b, Lisa 93a, 93b, 93c].

While the BUU model reproduces the measured two–proton correlation function rather well at E/A=80 MeV, it over predicts the correlation function for the higher beam energies; see Figure 6.9. Measured (predicted) correlation functions corresponding to the low–momentum cut are shown in solid points (solid lines) and those corresponding to our high–momentum cut are shown in

open points (open lines), for the E/A=80 MeV (top panel), 120 MeV (middle panel), and E/A=160 MeV (bottom panel), respectively, all for central collissions. The data show less sensitivity to the bombarding energy than predicted by the BUU calculations. At all three energies, the maximum of 1+R(q) at $q \approx 20$ MeV/c is larger than for the Ar+Au reaction at E/A=200 MeV [Kund 93], and the minimum at $q \approx 0$ is clearly observed for both cuts on P_{cm}. (The approximate momentum gates used in Reference [Kund 93] were $P_{cm} \approx 160 - 340$, 340 – 430, and 430 – 570 MeV/c. No minimum was observed for the higher two gates).

Figure 6.10 shows the average value of the correlation function, $\langle 1+R \rangle_{q=15-25\,MeV/c}$, in the peak region for measured (solid points) and BUU–predicted (open points) events, as a function of the total momentum of the proton–pair, for the central E/A=120 MeV (upper panel) and E/A=160 MeV (lower panel) collisions. In both cases, the BUU model is shown to substantially over predict the measured values, for all values of proton–pair center–of–mass momentum.

6.3.1. Varying BUU Input Parameters

We have explored whether different BUU input parameters would lead to better agreement with the data. Sensitivities to the stiffness of the equation of state are small [Gong 91a]. However, the choice of freeze–out density (ρ_f) could affect the apparent source size. Also, BUU calculations were recently shown to provide improved agreement with the balance energy in collective flow data if

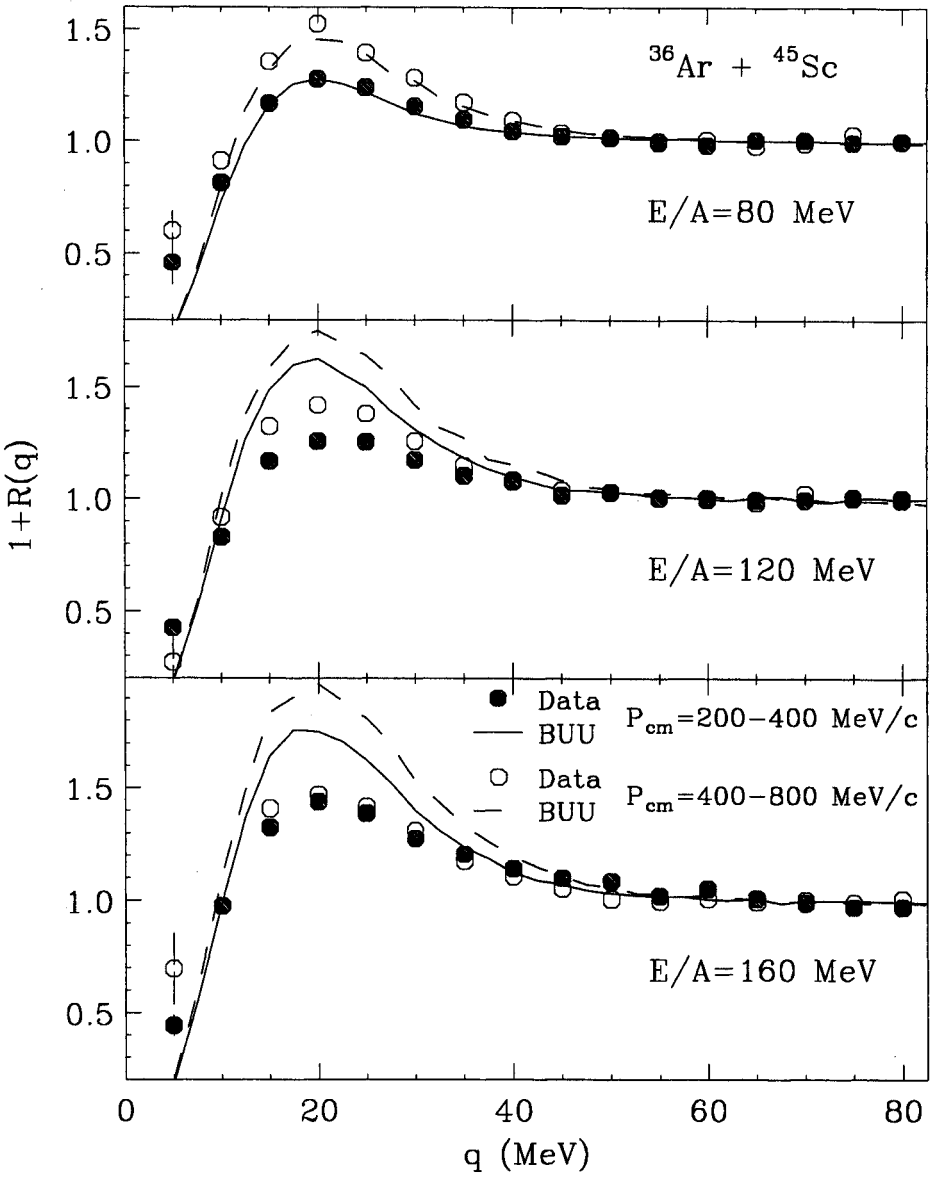

Figure 6.9. Two-proton correlation functions for central collisions of ^{36}Ar + ^{45}Sc at E/A = 80 MeV (top), 120 MeV (middle) and 160 MeV (bottom). results with our low–momentum gates are shown in solid points (data) and solid lines (theory), while high–momentum gated results are shown in open points (data) and dashed lines (theory).

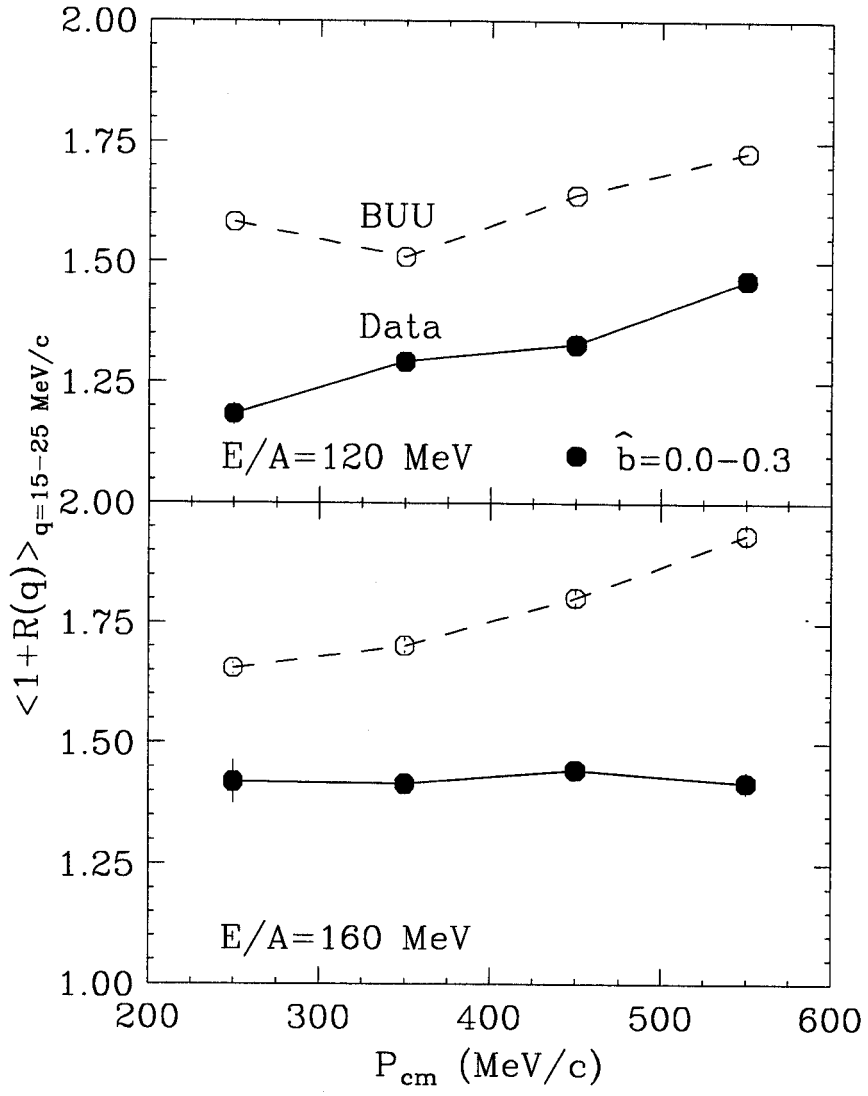

Figure 6.10. The average value of the correlation function, $\langle 1+R\rangle_{q=15-25\,MeV/c}$, in the peak region is plotted versus total proton momentum for our E/A=120 MeV (top) and E/A=160 MeV (bottom) reactions for central collisions. Data are shown in solid points and BUU predictions in open points.

one allows for a density dependence of the nucleon–nucleon cross section (σ_{NN}) [Klak 93]. By using a Taylor expansion for the density dependence of the in–medium cross section, $\sigma_{NN} = (1+\alpha\rho/\rho_o)\sigma_{NN}^{free}$, best agreement with balance energy data was obtained for $\alpha = -0.2$ [Klak 93]. Therefore, we have performed calculations for different choices of freeze–out density, $\rho_f = \rho_o/8$, $\rho_o/16$ and $\rho_o/32$, and for paramter $\alpha = 0, -0.2, -0.4$. Figure 6.11 shows the average peak height of the correlation function at E/A=120 MeV as a function of the proton–pair momentum for data and for BUU simulations. The solid, hatched and dotted regions show predictions for ρ_f = 1/8, 1/16, and 1/32 normal nuclear matter density respectively, each for α between 0 and –0.4. These simulations show little dependence on ρ_f and α, except at lower total momentum where smaller values of ρ_f reduce the predicted peak height. However, no commbination of ρ_f and α is able to reproduce the data, suggesting that the BUU is deficient in its description of the emitted proton phase space distribution at this energy.

The BUU predictions can be understood from the proton emission rates, dP/dt, calculated for central ^{36}Ar + ^{45}Sc collisions, as shown in Figure 6.12. At 80 MeV per nucleon (solid line), the BUU calculations predict the existance of a long–lived residue which slowly cools by particle emission [Lisa 93b, Hand 94]. In contrast, at E/A=120 MeV (dashed line) and 160 MeV (dotted line), a fast flash of nucleon emission is predicted, without any residue. While this drastically different scenario leaves no obvious signature in the single–particle spectra shown earlier in this chapter, it results in enhanced two–proton correlations, at variance with the data.

6.4 Importance of Particle Unstable Resonances

The lack of fragment formation in the current BUU formalism may be responsible for its substantial over prediction of the correlation functions at

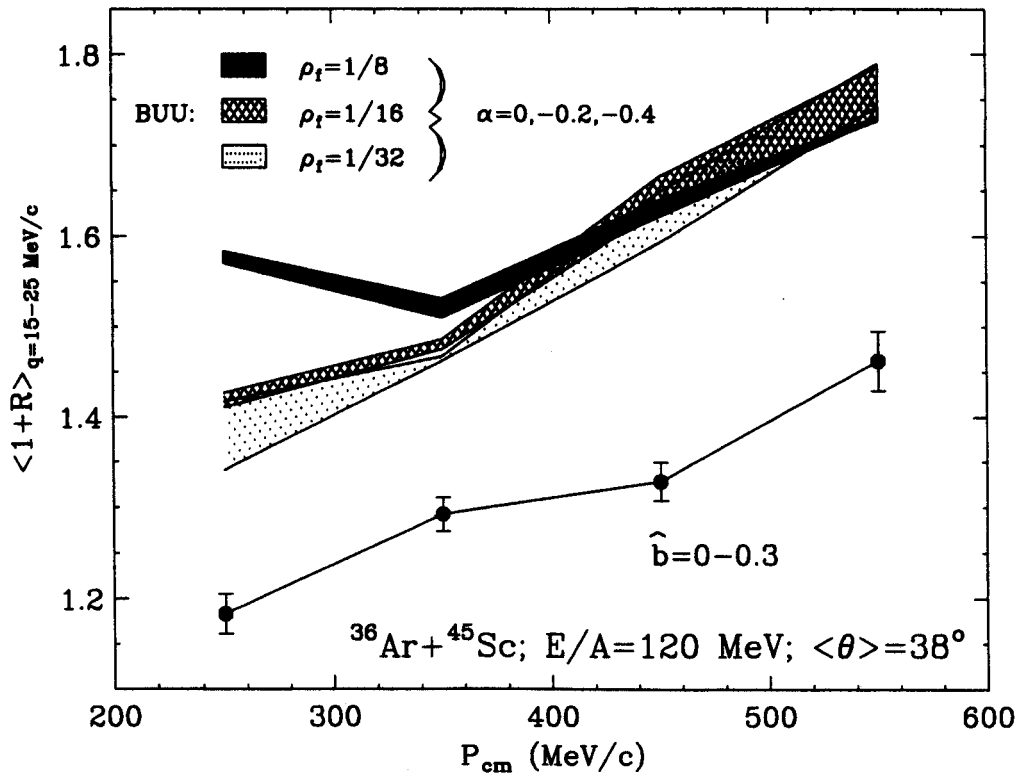

Figure 6.11. The average peak height (at q = 15 - 25 MeV/c) of the two-proton correlation function is shown versus the total proton-pair momentum in the center-of-mass rest frame for central collisions of ^{36}Ar + ^{45}Sc at E/A=120 MeV. Data are shown as solid points. BUU simulations were calculated for freeze-out density ρ_f = 1/8 (solid), 1/16 (hatched) and 1/32 (dotted). Each band shows the range of BUU predictions for values of the parameter α (explained in the text) ranging from 0 to -0.4.

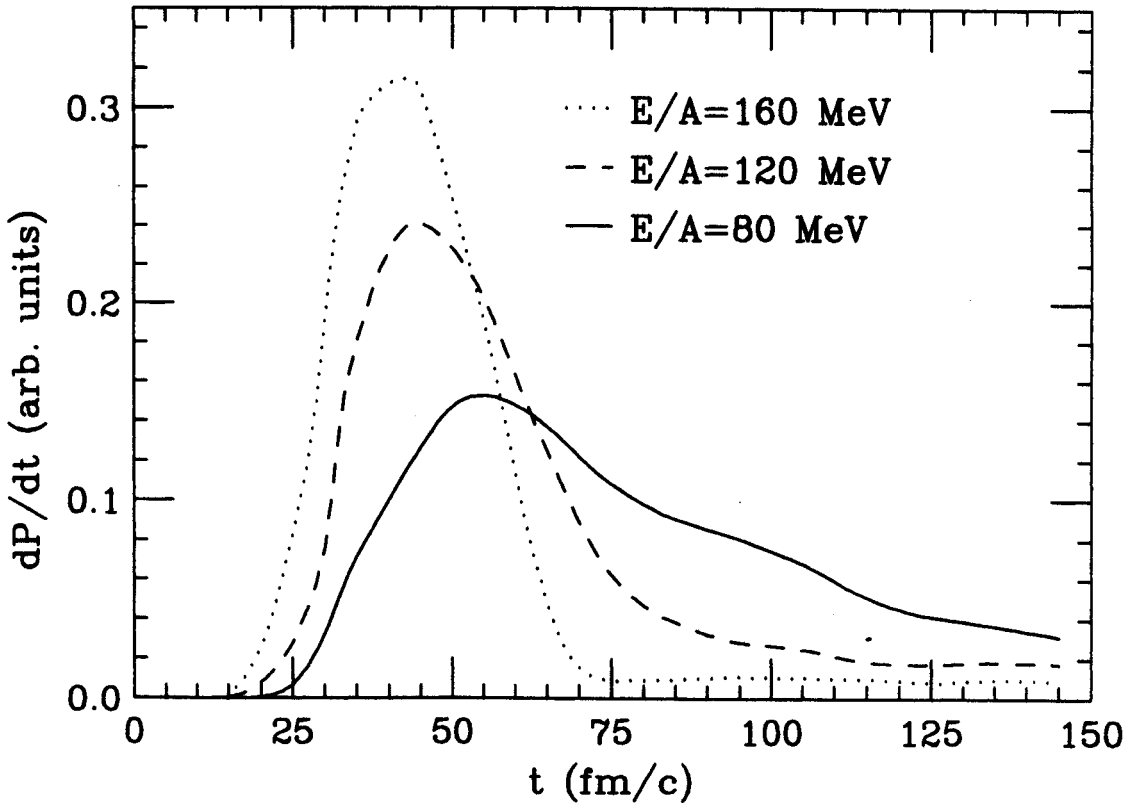

Figure 6.12. Proton emission rates, dP/dt, predicted by BUU calculations from central ^{36}Ar + ^{45}Sc collisions at E/A=80 MeV (solid), 120 MeV (dashed) and 160 MeV (dotted).

E/A=120 and 160 MeV. At much higher energies (1.6 GeV), $\pi^+\pi^-$ correlation functions were well reproduced by BUU calculations in which *baryonic* resonances (such as Δ and N*) played a large role [Plut 93]. At the energies under consideration here, highly excited *particle–unstable fragments* may play an important role in proton production by extending the time scale, τ, over which protons are emitted. We simulate the effects of proton emission from excited states by taking a fraction of the protons (f), predicted to be emitted by the BUU model, and delaying their emissions for a time t, statistically distributed according to $dP/dt = e^{-t/\tau}$. By letting τ range from 20 to 240 fm/c, we simulate emission from resonances of approximately 0.8–10 MeV. The predicted spatial coordinates and momenta are left unchanged. Figures 6.13 and 6.14 show examples of simulations which reproduce the magnitudes of the experimental correlation functions at E/A=120 and 160 MeV, respectively. For the E/A=120 MeV case, the plot shows that simulations with τ=160 fm/c, and f ranging from 30% to 50% bracket the data, providing an excellent fit in the peak reagion of the correlation function, which is the primary indicator of source size. For E/A=160 MeV (Figure 6.14), with τ=160 fm/c, the fraction of delayed protons needed to fit the data lies between 20% and 30%. Somewhat surprisingly, fewer protons need to be delayed at 160 MeV in order to agree with the data than at 120 MeV. Figure 6.12 shows the BUU prediction that protons are emitted over a longer time interval at 120 than at 160 MeV. Delaying a broader distribution (such as the 120 MeV predictions) will have a smaller effect on the proton separation than delaying a sharper distribution (such as the 160 MeV predictions). Therefore, longer times (or more resonances) are required at 120 MeV. However, because of the schematic nature of our calculations, this result should not be over interpreted. The inserts of Figures 6.13 and 6.14 show the ranges of t and f which give similarly good agreement with the data. To some extent, smaller fractions of "delayed" protons, f, can be compensated by longer delay times, τ.

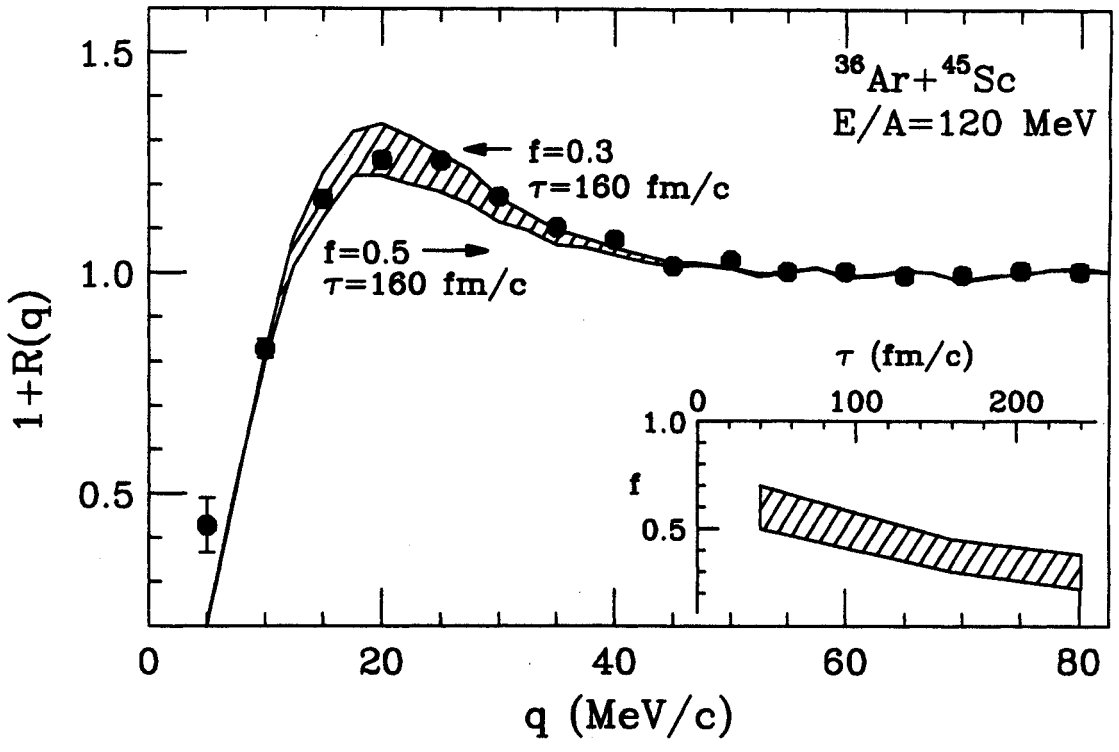

Figure 6.13. Two proton correlation functions (for low-momentum cut) for central collisions of ^{36}Ar + ^{45}Sc at E/A=120 MeV. Data are shown by points, and the results of "delayed" BUU simulations are shown in the hatched area, defined by t=160 fm/c and f=30% to 50%. Details are given in the text. The insert depicts the ambiguity between the parameters τ and f.

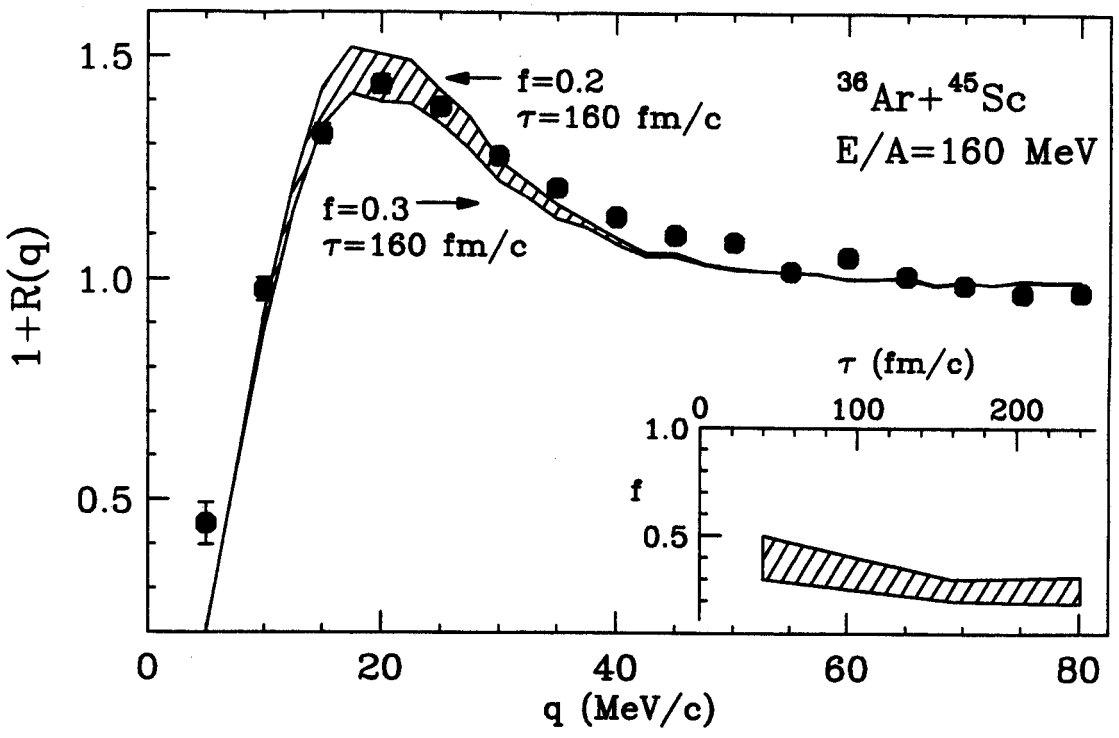

Figure 6.14. Two proton correlation functions (for low-momentum cut) for central collisions of ^{36}Ar + ^{45}Sc at E/A=160 MeV. Data are shown by points, and the results of "delayed" BUU simulations are shown in the hatched area, defined by t=160 fm/c and f=20% to 30%. Details are given in the text. The insert depicts the ambiguity between the parameters τ and f.

weaken the signal. Unless stringently tight cuts on centrality and orientation of relative momenta can be achieved, there is little hope of extracting a toroidal signature with the two–proton correlation function.

Measured correlation functions for the same system at E/A=120 and 160 MeV reveal a weaker dependence on the total momentum of the proton–pair with increasing beam energy. This may indicate that at higher energies, all protons are emitted on similar time scales, and that there is no significant cooling of the source. The BUU model predicts that the peak height of the correlation function rises with beam energy, at variance with the data. Furthermore, it severely over predicts the magnitude of the correlation function at energies above E/A=80 MeV, consistent with a previous study for a less symmetric system.

Varying BUU input parameters, such as the freeze–out density and magnitude of the density dependence of the nucleon–nucleon cross section, has little effect on its predictions. It was shown that particle–unstable fragments, such as $^{5}Li^{*}$, could play an important role in this energy regime, by extending the time scale over which protons are emitted, thus reducing the magnitude of the correlation function. Because such resonances are not modeled by BUU, we schematically incorporate their effects by delaying the predicted emission of protons. Statistical calculations indicate that between 20% and 50% of all protons are emitted from resonances at these energies, which we showed to be consistent with emission from states of widths 1–4 MeV, typical of light resonances. In order to fully assess the importance of such resonances, the development of a truly quantum transport model, which incorporates the production of fragments, is needed in this energy range.

LIST OF REFERENCES

References

[Aich 91] J. Aichlin, Phys. Rep. **202**, 233 (1991).

[Alm 93] T. Alm, G. Röpke, and M. Schmidt, Phys. Lett. **B301**, 170 (1993).

[Awes 88] T.C. Awes, R.L. Ferguson, F.E. Obenshain, F. Plasil, G.R. Young, S. Pratt, Z. Chen, C.K. Gelbke, W.G. Lynch, J. Pochadzalla, and H.M. Xu, Phys. Rev. Lett. **61**, 2665 (1988).

[Baue 86] W. Bauer, G.F. Bertsch, W. Cassing, and U. Mosel, Phys. Rev. C **34**, 2127 (1986).

[Baue 87] W. Bauer, Nucl. Phys. **A471**, 604 (1987).

[Baue 92a] W. Bauer, G.F. Bertsch, and H. Schulz, Phys. Rev. Lett. **69** 1888 (1992).

[Bern 85] M.A. Bernstein, W.A. Friedman, W.G. Lynch, C.B. Chitwood, D.J. Fields, C.K. Gelbke, M.B. Tsang, T.C. Awes, R.L. Ferguson, F.E. Obenshain, F. Plasil, R.L. Robinson, and G.R. Young, Phys. Rev. Lett. **54**, 402 (1985).

[Boal 86a] D.H. Boal, and J.C. Shillock, Phys. Rev. C **33**, 549 (1986).

[Boal 86b] D.H. Boal, and H. DeGuise, Phys. Rev. Lett. **57**, 2901 (1986).

[Boal 90] D.H. Boal, C.K. Gelbke, and B.K. Jennings, Rev. Mod. Phys. **62**, 553 (1990), and references therein.

[Bord 85] B. Borderie, B. Remaud, M.F. Rivet, and F. Sebille, Phys. Lett. B **302**, 53 (1985).

[Bowm 93] D.R. Bowman, G.F. Peaslee, N. Carlin, R.T. de Souza, C.K. Gelbke, W.G. Gong, Y.D. Kim, M.A. Lisa, W.G. Lynch, L. Phair, M.B. Tsang, C. Williams, N. Colonna, K. Hannold, M.A. McMahan, G.J. Wozniak, and L.G. Moretto, Phys. Rev. Lett. **70**, 3534 (1993).

[Cebr 89] D.A. Cebra, W. Benenson, Y. Chen, E. Kashy, A. Pradhan, A. Vander Molen, G.D. Westfall, W.K. Wilson, D.J. Morrissey, R.S. Tickly, R. Korteling, and R.L. Helmer, Phys. Lett. **227B**, 336 (1989).

[Cebr 90] D.A. Cebra, Ph.D. Thesis, Department of Physics and Astronomy, Michigan State University.

[Chen 87a] Z. Chen, C.K. Gelbke, J. Pochadzalla, C.B. Chitwood, D.J. Fields, W.G. Lynch, and M.B. Tsang, Phys. Lett. B **186**, 280 (1987).

[Chen 87b] Z. Chen, C.K. Gelbke, W.G. Gong, Y.D. Kim, W.G. Lynch, M.R. Maier, J. Pochadzalla, M.B. Tsang, F. Saint-Laurent, D. Ardouin, D.

Delegrange, H. Doubre, J. Kasagi, A. Kyanowski, A. Péghaire, J. Péter, E. Rosato, G. Bizard, F. Lefèbvres, T. Tamain, J. Québert, and Y.P. Viyogi, Phys. Lett. C **36**, 2297 (1987).

[Chen 87c] Z. Chen, C.K. Gelbke, J. Pochadzalla, C.B. Chitwood, D.J. Fields, W.G. Gong, W.G. Lynch, M.B. Tsang, Nucl. Phys. **A473**, 564 (1987).

[Chit 85] C.B. Chitwood, J. Aichlin, D.H. Boal, G. Bertsch, D.J. Fields, C.K. Gelbke, W.G. Lynch, M.B. Tsang, J.C. Shillcock, T.C. Awes, R.L. Ferguson, F.E. Obenshain, F. Plasil, R.L. Robinson, and G.R. Young, Phys. Rev. Lett. **54**, 302 (1985).

[Chit 86a] C.B. Chitwood, C.K. Gelbke, J. Pochadzalla, Z. Chen, D.J. Fields, W.G. Lynch, R. Morse, M.B. Tsang, D.H. Boal, and J.C. Shillcock, Phys. Lett. **172B**, 27 (1986).

[DeYo 89] P.A. DeYoung, M.S. Gordon, Xiu qin Lu, R.L. McGrath, J.M. Alexander, D.M. de Castro Rizzo, and L. C. Vaz, Phys. Rev. C **39**, 128 (1989).

[DeYo 90] P.A. DeYoung, C. J. Gelderloos, D. kortering, J. Sarafa, K. Zienert, M.S. Gordon, B.J. Fineman G.P. Gilfoyle, X. Lu,. R.L. McGrath, D.M. de Castro Rizzo, J.M. Alexander, G. Auger, S. Kox, l.C. Vaz, C. Beck, D.J. Henderson, D.G. Kovar, and M.F. Vineyard, Phys. Rev. C **41**, R1885 (1990).

[Dupi 88] P. Dupieux, J.P. Alard, J. Augerat, R. Bainet, N. Bastid, F. Brochard, P. Charmensat, N. De Marco, H. Fanet, Z. Fodor, L. Freysse, J. Girard, P. Gorodetzky, J. Gosset, C. Laspalles, M.C. Lemaire, D. L'Hôte, B. Lucas, J. Marroncle, G. Montarou, M.J. Parizet, J. Poitou, D. Qassoud, C. Racca, A. Rahmani, W. Schimmerling, and O. Vallete, Phys. Lett. B **200**, 17 (1988).

[Elma 93] A. Elmaani, J.M. Alexander, N.N. Ajitanand and Roy A. Lacey, Phys. Rev. C **48**, 2864 (1993).

[Eraz 91] B. Erazmus, N. Carjan, and D. Ardouin, Phys. Rev. C **44**, 2663 (1991).

[Fái 82] G. Fái and J. Randrup, Nucl. Phys. **A381**, 557 (1982).

[Fái 83] G. Fái and J. Randrup, Nucl. Phys. **A404**, 551 (1983).

[Fox 88] D. Fox, D.A. Cebra, J. Karn, C. Parks, A. Pradhan, A.M. Vander Molen, J. van der Plicht, G.D. Westfall, W.K. Wilson, and R.S. Tickle, Phys. Rev. C **38**, 146 (1988).

[Fox 93] D. Fox, R.T. deSouza, L. Phair, D.R. Bowman, N. Carlin, C.K. Gelbke, W.G. Gong, Y.D. Kim, M.A. Lisa, W.G. Lynch, G.F. Peaslee, M.B. Tsang, and F. Zhu, Phys. Rev. C **47**, R421 (1993).

[Glas 93] T. Glasmacher, C.K. Gelbke, and S. Pratt, Phys. Lett. B **314**, 265 (1993).

[Gold 59] G. Goldhaber, W.B. Fowler, S. Goldhaber, T.F. Hoang, T.E. Kalogeropolous, and W.M. Powell, Phys. Rev. Lett., **3**, 181 (1959).

[Gold 60] G. Goldhaber, S. Goldhaber, W. Lee, and A. Pais, Phys. Rev. **120**, 300 (1960).

[Gong 88] G.W. Gong, Y.D. Kim, G. Poggi, Z. Chen, C.K. Gelbke, W.G. Lynch, M.R. Maier, T. Murakami, M.B. Tsang, H.M. Xu, and K. Kwiakowski, Nucl. Intr. and Meth. **A268**, 190 (1988).

[Gong 90a] G.W. Gong, N. Carlin, C.K. Gelbke, and R. Dayton, Nucl. Intr. and Meth. **A287**, 639 (1990).

[Gong 90b] G.W. Gong, C.K. Gelbke, N. Carlin, R.T. de Souza, Y.D. Kim, W.G. Lynch, T. Murakami, G. Poggi, D. Sanderson, M.B. Tsang, H.M. Xu, D.E. Fields, K. Kwiakowski, R. Planeta, V.E. Viola, Jr., S.J. Yennello, and S. Pratt, Phys. Lett. B **246**, 21 (1990).

[Gong 90c] G.W. Gong, W. Bauer, C.K. Gelbke, N. Carlin, R.T. de Souza, Y.D. Kim, W.G. Lynch, T. Murakami, G. Poggi, D. Sanderson, M.B. Tsang, H.M. Xu, S. Pratt, D.E. Fields, K. Kwiakowski, R. Planeta, V.E. Viola, Jr., and S.J. Yennello, Phys. Rev. Lett. **65**, 2114 (1990).

[Gong 91a] W.G. Gong, W. Bauer, C.K. Gelbke, and S. Pratt, Phys. Rev. C **43**, 781 (1991).

[Gong 91b] G.W. Gong, C.K. Gelbke, W. Bauer, N. Carlin, R.T. de Souza, Y.D. Kim, W.G. Lynch, T. Murakami, G. Poggi, D. Sanderson, M.B. Tsang, H.M. Xu, D.E. Fields, K. Kwiakowski, R. Planeta, V.E. Viola, Jr., and S.J. Yennello, Phys. Rev. C **43**, 1804 (1991).

[Gong 91c] G.W. Gong, Ph.D. Thesis, Department of Physics and Astronomy, Michigan State University (1991).

[Gong 92] G.W. Gong, Y.D. Kim, and C.K. Gelbke, Phys. Rev. C **45**, 863 (1992).

[Gong 93] G.W. Gong, P. Danielewicz, C.K. Gelbke, N. Carlin, R.T. de Souza, Y.D. Kim, W.G. Lynch, T. Murakami, Poggi, M.B. Tsang, H.M. Xu, S. Pratt, K. Kwiatkowski, V.E. Viola, Jr., S.J. Yennello, and J.C. Shillcock, Phys. Rev. C **47**, R429 (1993).

[Goss 78] J. Gosset, J.I. Kapusta, and G.D. Westfall, Phys. Rev. C **18**, 844 (1978).

[Gouj 91] D. Goujdama, F. Guilbault, C. Lebrun, D. Ardouin, H. Dabrowski, S. Pratt, P. Lautridou, R. Boisgard, J. Québert, and A. Péghaire, Z Phys. A **339**, 293 (1991).

[Gros 92] D.H.E. Gross, B.A. Li, and A.R. DeAngelis, Ann. Physik **1**, 467 (1992).

[Gust 84] H.A. Gustafsson, H.H. Gutbrod, B. Kolb, H. Loehner, B. Ludewigt, A.M. Poskanzer, T. Renner, H. Riedesel, H.G. Ritter, A. Warwick, F. Weik, and H. Wieman, Phys. Rev. Lett. **53**, 544 (1984).

[Hanb 54] R. Hanbury Brown and R.Q. Twiss, Phil. Mag. **45**, 663 (1954).

[Hanb 57a] R. Hanbuury Brown and R.Q. Twiss, Proc. R. Soc. London Ser. A **242**, 300 (1957).

[Hanb 57b] R. Hanbuury Brown and R.Q. Twiss, Proc. R. Soc. London Ser. A **243**, 291 (1957).

[Hand 94] D.O. Handzy, M.A. Lisa, C.K. Gelbke, W. Bauer, F.C. Daffin, P. Dekowski, W.G. Gong, E. Gualtieri, S. Hannuschke, R. Lacey, T. Li, W.G. Lynch, C.M. Mader, G.F. Peaslee, T. Reposeur, S. Pratt, A.M. Vander Molen, G.D. Westfall, J. Yee, and S.J. Yennello, Phys. Rev. C **50**, 858 (1995).

[Hand 95a] D.O. Handzy, S.J. Gaff, W. Bauer, F.C. Daffin, C.K. Gelbke, and G.J. Kunde, Phys. Rev. C **51**, 2237 (1995).

[Hand 95b] D.O. Handzy, W. Bauer, F.C. Daffin, S.J. Gaff, C.K. Gelbke, T. Glasmacher, E. Gualtieri, S. Hannuschke, M.J. Huang, G.J. Kunde, R. Lacey, T. Li, M.A. Lisa, W.J. Llope, W.G. Lynch, L. Martin, C.P. Montoya, R. Pak, G.F. Peaslee, S. Pratt, C. Schwarz, N. Stone, M.B. Tsang, A.M. Vander Molen, G.D. Westfall, J. Yee, and S.J. Yennello, submitted to Phys. Rev. Lett.

[Hsi 94] W.C. Hsi, G.J. Kunde, J. Pochadzalla, W.G. Lynch, M.B. Tsang, M.L. Begemann-Blaich, D.R. Bowman, R.J. Charity, F. Cosmo, A. Ferrero, C.K. Gelbke, T. Glasmacher, T. Hofmann, G. Imme, I. Iori, J. Hubele, J. Kempter, P. Kreutz, W.D. Kunze, V. Lindenstruth, M.A. Lisa, U. Lynen, M. Mang, A. Moroni, W.F.J. Müller, M. Neumann, B. Ocker, C.A. Ogilvie, G.F. Peaslee, G. Raciti, F. Rosenberger, H. Sann, R. Scardaoni, A. Schüttauf, C. Schwarz, W. Seidel, V. Serfling, L.G. Sobotka, L. Stuttge, S. Tomasevic, W. Trautmann, A. Tucholski, C. Williams, A. Wörmer, and B. Zwieglinski, Phys. Rev. Lett. **73**, 3367 (1994).

[Jeon 94] S.C. Jeong, for the FOPI collaboration, Phys. Rev. Lett. **72**, 3468 (1994).

[Kim 91] Y.D. Kim, R.T. de Souza, D.R. Bowman, N. Carlin, C.K. Gelbke, W.G. Gong, W.G. Lynch, L. Phair, M.B. Tsang, F. Zhu, and S. Pratt, Phys. Rev. Lett **67**, 14 (1991).

[Kim 92] Y.D. Kim, R.T. de Souza, C.K. Gelbke, W.G. Gong, and S. Pratt, Phys. Rev. C **45**, 387 (1992).

[Klak 93] D. Klakow, G. Welke, an W. Bauer, Phys. Rev. C **48**, 1982 (1993).

[Koon 77] S.E. Koonin, Phys. Lett. **70B**, 43 (1977).

[Kopy 72] G.I. Kopylov, Phys. Lett. **B50**, 472 (1974).

[Kox 87] S. Kox, A. Gamp, C. Perrin, J. Arvieux, R. Bertholet, J.F. Bruandet, M. Buenerd, R. Cherkaoui, A.J. Colde, Y. El–Masri, N. Longequeue, J. Menet, F. Merchez, and J.B. Viano, Phys. Rev. C **35**, 1678 (1987).

[Kund 93] G.J.Kunde, J. Pochadzalla, E. Berdermann, B. Berthier, C. Cerruti, C.K. Gelbke, J. Hubele, P. Kreutz, H. Pinkenburg, G. Raciti, H. Sann, and W. Trautmann, Phys. Rev. Lett. **70**, 2545 (1993).

[Kyan 86] A. Kyanowski, F. Saint-Lauret, D. Ardouin, H. Delagrande, H. Doubre, C. Gregoire, W. Mittig, A. Péghaire, J. Péter, Y.P. Viyogi, B. Zwieglinski, J. Québert, G. Bizard, F. Lefèbvres, B. Tamain, J. Pochodzalla, C.K. Gelbke, W. Lynch, and M. Maier, Phys. Lett. B. **181**, 43 (1986).

[Ledn 95] R. Lednicky, V.L. Lyuboshitz, B. Erazmus, and D. Nouais, submitted to Nucl. Phys. A.

[Li 91a] B.A. Li, and W. Bauer, Phys. Rev. C **44**, 450 (1991).

[Li 91b] B.A. Li, W. Bauer, and G.F. Bertsch, Phys. Rev. C **44**, 2095 (1991).

[Li, T 93] T. Q. Li, Ph.D. Thesis, Department of Physics and Astronomy, Michigan State University (1993).

[Lisa 91] M.A. Lisa, W.G. Gong, C.K. Gelbke, and W.G. Lynch, Phys. Rev. C **44**, 2865 (1991).

[Lisa 93a] M.A. Lisa, C.K. Gelbke, W. Bauer, P. Dekowski, W.G. Gong, E. Gualtieri, S. Hannuschke, R. Lacey, T. Li, W.G. Lynch, C.M. Mader, G.F. Peaslee, T. Reposeur, S. Pratt, A.M. Vander Molen, G.D. Westfall, J. Yee, and S.J. Yennello, Phys, Rev. Lett **70**, 3709 (1993).

[Lisa 93b] M.A. Lisa, C.K. Gelbke, W. Bauer, P. Dekowski, W.G. Gong, E. Gualtieri, S. Hannuschke, R. Lacey, T. Li, W.G. Lynch, C.M. Mader, G.F. Peaslee, T. Reposeur, S. Pratt, A.M. Vander Molen, G.D. Westfall, J. Yee, and S.J. Yennello, Phys, Rev. Lett **71**, 2863 (1993).

[Lisa 93c] M.A. Lisa, Ph.D. Thesis, Department of Physics and Astronomy, Michigan State University (1993).

[Litt 80] U. Littmark and J.F. Ziegler, Handbook of Range Distributions for Energetic Ions in all Elements, Pergamon Press, 1980.

[Lynch 82] W.G. Lynch, L.W. Richardson, M.B. Tsang, R.E. Ellis, C.K. Gelbke, and R.E. Warner, Phys. Lett. **108B**, 274 (1982).

[Lync 83] W.G. Lynch, C.B. Chitwood, M.B. Tsang, D.J. Fields, D.R. Klesch, C.K. Gelbke, G.R. Young, T.C. Awes, R. Ferguson, F.E. Obenshain, F. Plasil, R.L. Robinson, and A.D. Panagiotou, Phys. Rev. Lett. **51**, 1850 (1983).

[Mart 95] L. Martin, C.K. Gelbke, B. Erazmus, and R. Lednicky, to be published.

[Mess 76] A. Messiah, "Quantum Mechanics," Volume 1, North Holland Publishing Company, Amsterdam (1976).

[Mont 94] C.P. Montoya, W.G. Lynch, D.R. Bowman, G.F. Peaslee, N. Carlin, R.T. deSouza, C.K. Gelbke, W.G. Gong, Y.D. Kim, M.A. Lisa, L. Phair, M.B. Tsang, J. Webster, C. Williams, N. Colonna, K. Hanold, M.A. McMahan, G.J. Wozniak, and L.G. Moretto, Phys. Rev. Lett. **73**, 3070 (1994).

[More 92] L. G. Moretto, K. Tso, N. Colonna, and G.J. Wozniak Phys. Rev. Lett **69**, 1884 (1992).

[Phai 92] L. Phair, D.R. Bowman, C.K. Gelbke, W.G. Gong, Y.D. Kim, M.A. Lisa, W.G. Lynch, G.F. Peaslee, R.T. de Souza, M.B. Tsang, and F. Zhu, Nucl. Phys. **A548**, 489 (1992).

[Phai 93a] L. Phair, W. Bauer, and C.K. Gelbke, Phys. Lett. B **314**, 271 (1993).

[Phai 93b] L. Phair, D.R. Bowman, N. Carlin, C.K. Gelbke, W.G. Gong, Y.D. Kim, M.A. Lisa, W.G. Lynch, G.F. Peaslee, R.T. de Souza, M.B. Tsang, C. Williams, F. Zhu, N. Colonna, K. Hanold, M.A. McMahan, and G.J. Wozniak, Nucl. Phys. **A564**, 453 (1993).

[Plut 93] J. Pluta, A. Rahmani, D. Ardouin, R. Lednicky, P. Stefanski, H. Dabrowski, J.P. Alard, J. Augerat, N. Bastid, C. Cavata, P. Charmensat, P. Duplieux, P. Gorodetzky, J. Gosset, A. Le Merdy, D. L'Hôte, M.C. Lemaire, B. Lucas, J. Marroncle, G. Montarou, M.-J. Parizet, J. Poitou, D. Qassoud, O. Valette, H.N. Agakishiev, V.G. Grishin, W. Bauer, P. Danielewicz, D. Klakow, and P. Schuck, Nucl. Phys. **A562**, 365 (1993).

[Poch 86] J. Pochadzalla, C.B. Chitwood, D.J. Fields, C.K. Gelbke, W.G. Lycnh, M.B. Tsang, D.H. Boal, and J.C. Shillock, Phys. Lett. B **174**, 36 (1986).

[Poch 87] J. Pochadzalla, C.K. Gelbke, W.G. Lycnh, M. Maier, D. Ardouin, H. Delagrange, H. Doubre, C. Grégoire, A. Kyanoski, W. Mittig, A. Péghaire, J. Péter, F. Saint-Laurent, B. Zwieglinski, G. Bizard, F.

Lefèbvres, B. Tamain, J. Québert, Y.P. Viyogi, W.A. Friedman, and D.H. Boal, Phys. Rev. C **35**, 1695 (1987).

[Pratt 84] S. Pratt, Phys. Rev. Lett. **53**, 1219 (1984).

[Pratt 87] S. Pratt and M.B. Tsang, Phys. Rev. C **36**, 2390 (1987).

[Rebr 90] D. Rebreyend, S. Kox, J.C. Gondrand, B. Khelfaoui, F. Merchez, B. Norén, and C. Perrin, Proceedings of the International Workshop on Particle Correlation and Intererometry in Nuclear Collisions, Le Cellier, France, 1990, edited by D. Ardouin (World Scientific, Singapore, 1990), p. 3.

[Rebr 92] D. Rebreyend, F. Merchez, B. Norén, E. Andersen, M. Cronqvist, J.C. Gondrand, H.A. Gustafsson, B. Jäger, B. Jacoksson, B. Khelfaouli, S. Kox, A. Kristiansson, G. Lövhöiden, S. Mattson, T.F. Thorsteinsen, M. Westenius, and L. Westerberg, Phys. Rev. C **46**, 2387 (1992).

[Reid 68] R.V. Ried, Jr., Ann. Phys. (NY) **50**, 411 (1968).

[Swen 87] L. S. Swenson, Jr. Physica Today **40**, 24 (1987).

[West 76] G.D. Westfall, J. Gosset, P.J. Johansen, A.M. Poskanzer, W.G. Meyer, H.H. Gutbrod, A. Sandoval, and R. Stock, Phys. Rev. Lett. **37**, 1202 (1976).

[West 85] G.D. Westfall, J.E. Yurkon, J. van der Plicht, Z.M. Koenig, B.V. Jacak, R. Fox, G.M. Crawley, M.R. Maier, and B.E. Hasselquist, Nucl. Instr. Meth. **A238**, 347 (1985).

[Wils 91] W.K. Wilson, Ph.D. Thesis, Department of Physics and Astronomy, Michigan State University.

[Winf 91] J. Winfield, editor, "L'User's Guide to the MSU 4π Array," (unpublished), Original Version 1991.

[Xu 93] H.M. Xu, J.B. Natowitz, C.A. Gagliardi, R.E. Tribble, C.Y. Wong, and W.G. Lynch, Phys. Rev. C **48**, 933 (1993).

[Zajc 84] W.A. Zajc, J.A. Bisterlich, R.R. Bossingham, H.R. Bowman, C.W. Clawson, K.M. Crowe, K.A. Frankel, J.G. Ingersoll, J.M. Kurk, C.J. Martoff, D.J. Murphy, J.O. Rasmussen, J.P. Sullivan, E. Yoo, O. Hashimoto, M. Koike, W.J. McDonald, J.P. Miller, and P. Truöl, Phys. ReV C **29**, 2173 (1984).

[Zajc 92] W.A. Zajc, "A Pedestrian's Guide to Interferometry," (1992).

[Zarb 81] F. Zarbaksh, A.L. Sagle, F. Brochard, T.A. Mulera, V. Perez-Mendez, R. Talaga, I. Tanihata, J.B. Carroll, K.S. Ganezer, G. Igo, J. Oostens, D. Woodward, and R. Sutter, Phys. Rev. Lett. **46**, 1268 (1981).

[Zhu 91] F. Zhu, W.G. Lynch, T. Murakami, C.K. Gelbke, Y.D. Kim, T.K. Nayak, R. Pelak, M.B. Tsang, H.M. Xu, W.G. Gong, W. Bauer, K. Kwiatkowski, R. Planeta, S. Rose, V.E. Viola, Jr., L. W. Woo, S. Yennello, and J. Zhang, Phys. Rev. C **44**, R582 (1991).

master. We used the original 4π computer busy to veto the 4π master signals, and we used a stretched "hodoscope busy" to veto hodoscope master signals. For the higher energy experiment, we adopted a different method to veto the master signals. In this last experiment, we used a delayed (not stretched) hodoscope busy signal. Furthermore, we explicitly required a 4π master (appropriately delayed) in coincidence with every hodoscope master before issuing gates to the ADC's. This change prevented the possibility of events being written to tape in which hodoscope data was present without corresponding information from the 4π Array. Figure 2.6 shows the timing of the master electronics.

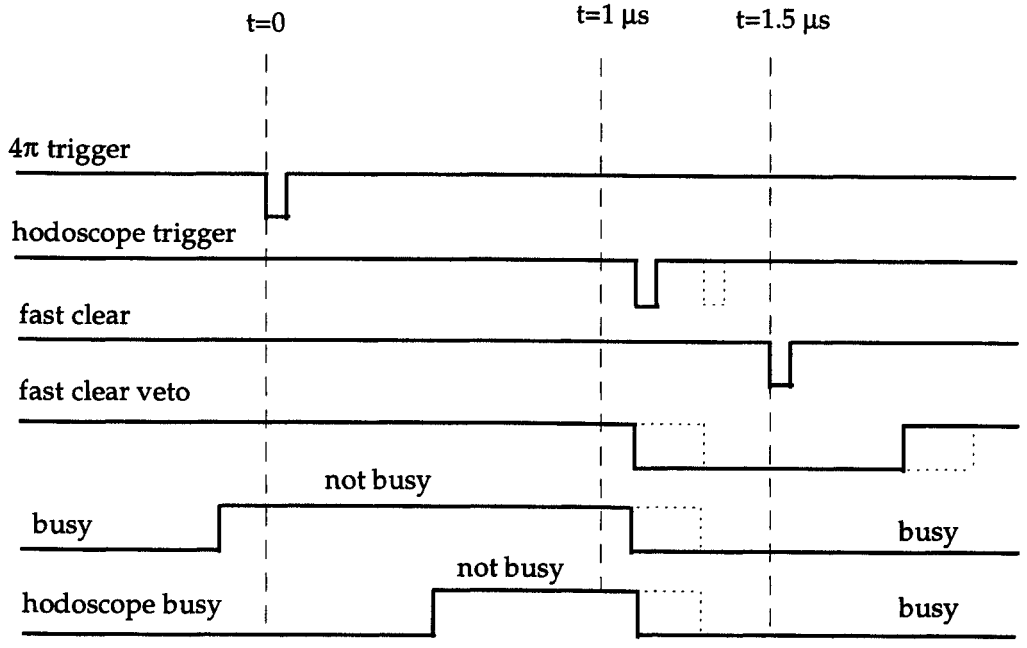

Figure 2.6. Master electronics timing diagram. The dashed lines indicate the effect of the (approximately) 200 ns "jitter" in the relative time between 4π triggers and hodoscope triggers. The fast clear is created about 1.5 μs after the 4π trigger, and the fast clear veto is issued immediately following a hodoscope trigger.

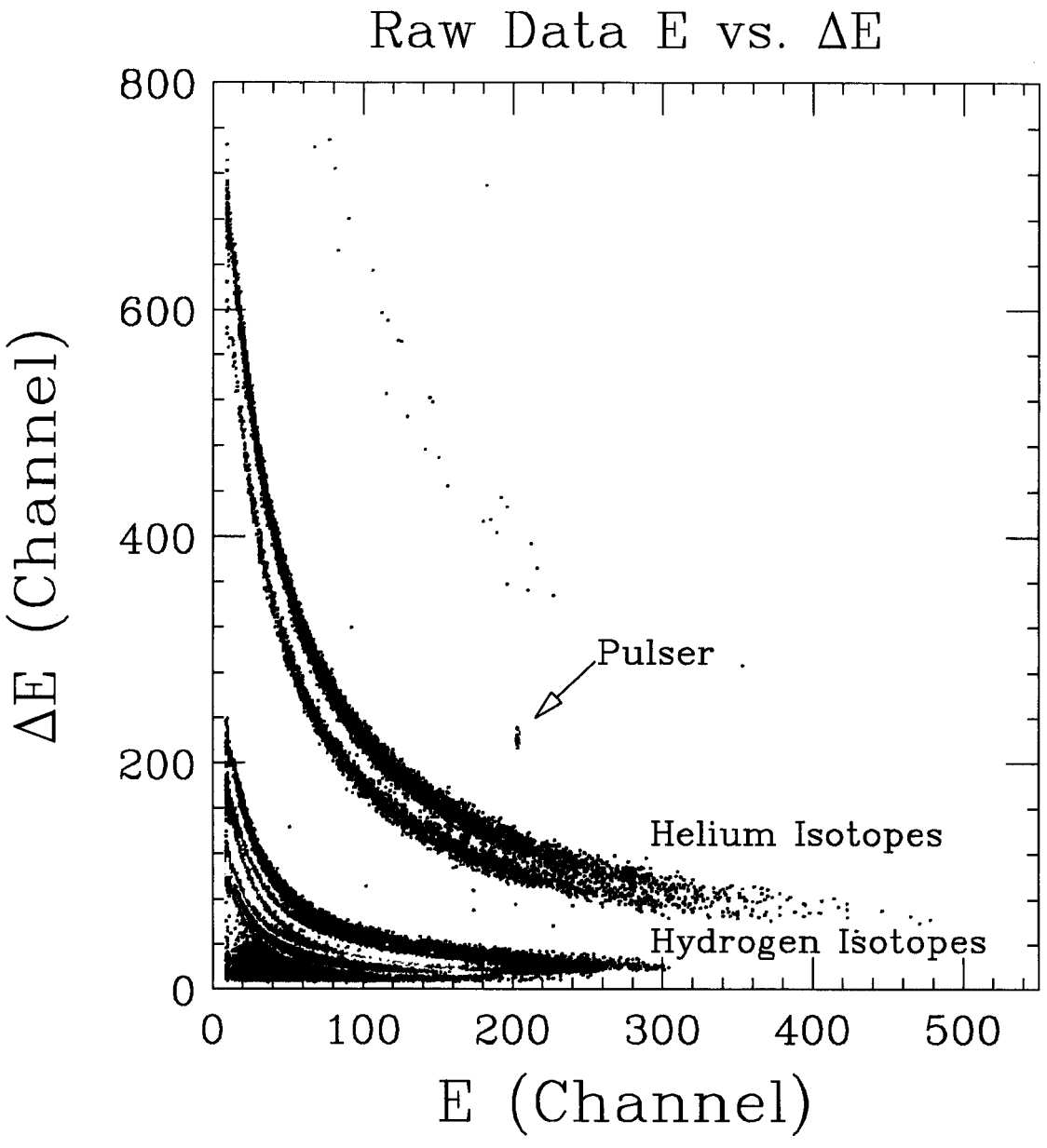

Figure 2.7. 2–dimensional E vs. ΔE for a typical hodoscope detector. Isotopes separate into hyperbolic bands on this logarithmic scale.

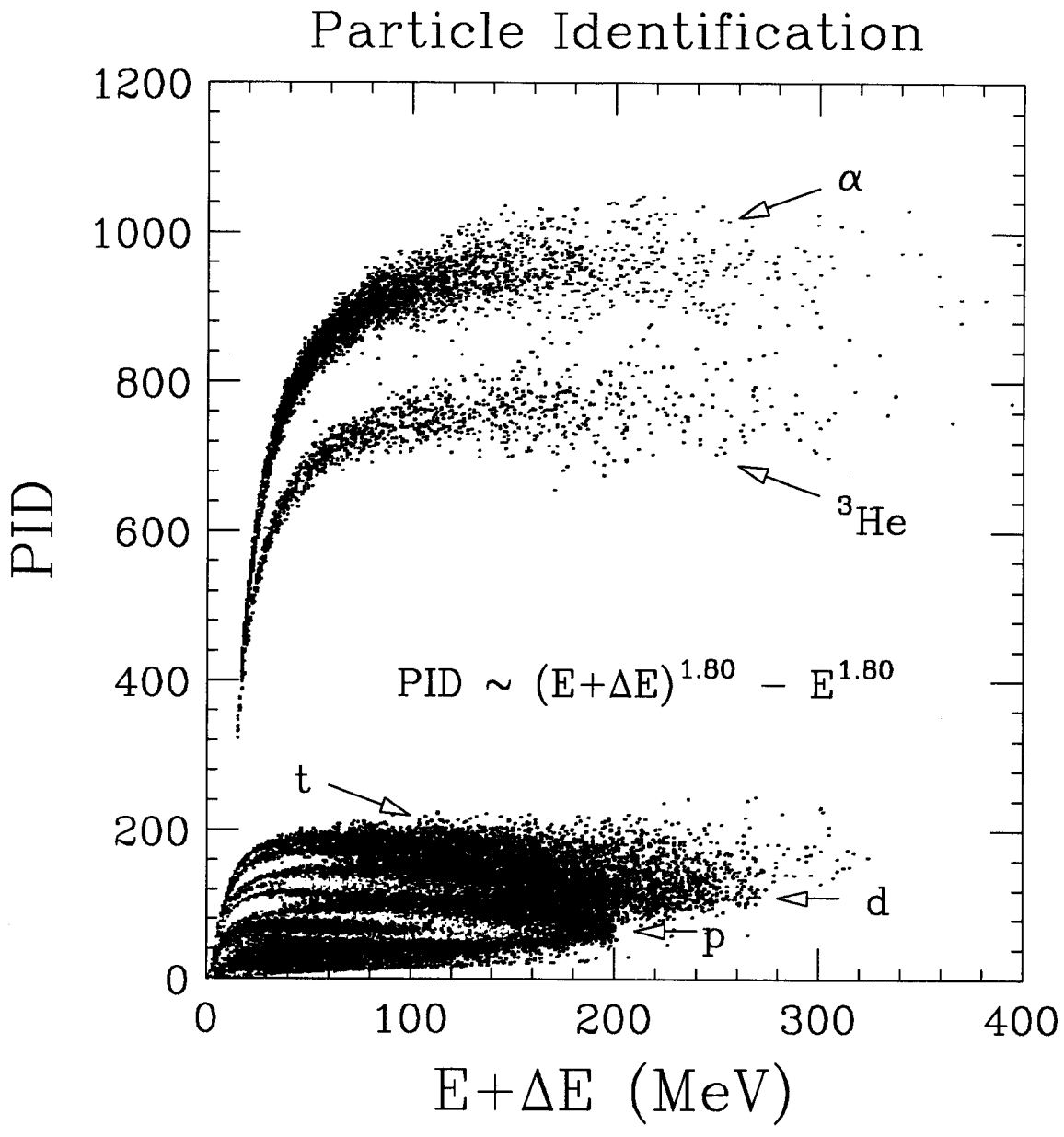

Figure 2.8. 2–dimensional total energy vs. PID plot showing linear separation of isotopes. Again, logarithmic density scale is used.